University of Exeter

College of Engineering, Mathematics and Physical Sciences

Monitoring chromatin remodelling in fixed and live immune cells using vibrational spectroscopy and microfluidics

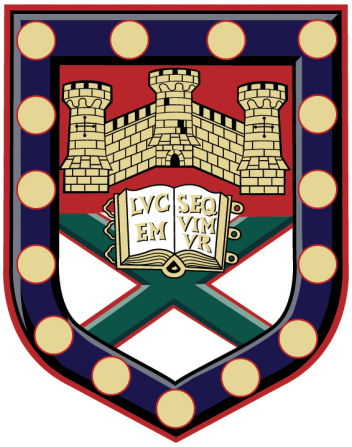

Author:

Rikke Brandstrup Morrish

Supervisors:

Prof. Francesca Palombo

Prof. Nick Stone

Dr. Stefano Pagliara

Prof. Richard Chahwan

Submitted by Rikke Brandstrup Morrish, to the University of Exeter as a thesis for the degree of Doctor of Philosophy in Physics, December 2020.

June 4, 2021 .....

Abstract

Eukaryotic cell growth, maintenance and differentiation relies on the dynamic structure of nuclear chromatin, the macromolecular complex consisting primarily of DNA and histones. Changes to chromatin structure and chemistry may lead to alterations in gene expression, resulting in functional and developmental processes in cells. Additionally, biomechanical properties of the nucleus, which play a role in mechanical signalling pathways, are also affected by chromatin conformation. The regulation and effects of chromatin dynamics in cellular processes have yet to be fully elucidated. Therefore, novel techniques for assessing chemical and mechanical signatures of cells undergoing chromatin changes during cell differentiation at the single cell level have great potential for 1) phenotypic characterisation of single cells for research and clinical purposes and 2) further unravelling the complex coordination of intracellular changes that occur during cell developmental steps and triggering of disease.

In this thesis, I have studied chromatin remodelling in immune cells using vibrational spectroscopy and microfluidics. Single cell measurements were conducted through optimisations of experimental and data analysis parameters. Vibrational spectroscopy methods included FTIR spectroscopic imaging and Raman microscopy, both label-free techniques that measure the interaction of light with chemical properties of a sample by interrogating its molecular vibrations. Microfluidics is a technique for manipulating fluids at a submillimetre scale. It was utilised here to enable live cell Raman mapping, as well as for deformability cytometry for assessing mechanical properties of the cell nuclei. To initiate an immune activation, B cells were incubated with a cytokine (CIT) cocktail.

The biomechanical property, nuclear auxeticity, was investigated in B cells using deformability cytometry. This property has previously been shown in transitioning embryonic stem (ES) cells, and chromatin decondensation has been determined to hold a regulatory role. Chromatin decondensation was therefore induced in B cells through immune activation (CIT treatment) or Trichostatin A (TSA) treatment. These cells were compared to untreated control cells. A subset of cells for both the CIT and TSA treatment, had auxetic nuclei. No control cells had auxetic nuclei.

These results showed nuclear auxeticity in B cells for the first time, and linked it to chromatin decondensation in agreement with previous ES cell data.

Using FTIR spectroscopic imaging and Raman microscopy, spectral features associated with chromatin and DNA changes during immune B cell activation were identified. Peak ratios for distinguishing between non-activated and activated immune cells were determined - for FTIR imaging: a DNA-to-protein peak ratio, and for Raman mapping: a peak ratio between two neighbouring peaks, both associated with nucleic acid. Both peak ratios measured the relative change in a peak associated with $\nu_s(PO_2^-)$, which was therefore shown to be a potential spectral marker for label-free characterisation of immune cells pre- and post activation. The biological origin of the FTIR spectral features was further investigated using additional cell treatments. Chromatin decondensation, intiated through CIT or TSA treatment, gave rise to similar change in the DNA-to-protein peak ratio. This supported the hypothesis that the $\nu_s(PO_2^-)$ spectral changes can be used to monitor structural changes occurring in chromatin and DNA itself.

Finally, the key biological pathways influencing the whole range of Raman spectral differences between non-activated and activated B cells were investigated. Partial least squares (PLS) regression was performed on Raman maps and transcriptomic data. It was determined that a linear correlation exists between the two data types. Transcripts of high importance for this correlation were identified. These included the B cell receptor genes and a number of transcripts of regulatory proteins with known roles in immune activation. Transcripts not previously linked to immune activation were also identified.

In summary, novel techniques for phenotypic characterisation of single cells were explored using both chemical and mechanical measurements of B cells undergoing immune activation. Previously unidentified biochemical and biomechanical factors influencing B cell activation were identified. These have added new layers to our understanding of this process and thus revealed potential new research directions. Furthermore, chromatin decondensation and transcriptional changes are key responses during all cell differentiation processes and disease development. Therefore, these experimental approaches have great potential for investigating other cell types and cellular processes.

Acknowledgements

This thesis is the result of four years' worth of exciting and challenging research. Thank you to the EPSRC for funding my PhD - and for extending the funding when the COVID-19 pandemic and national lockdowns brought everything to a halt. No doubt this thesis would have looked very different without it. I am immensely proud of my own hard work and perseverance that have gone into this work. That said, there are a great many people I wish to acknowledge for their input and support.

First and foremost I would like to thank my supervisory team Prof Francesca Palombo, Prof Nick Stone, Dr Stefano Pagliara and Prof Richard Chahwan. Each one of you have always found the time to discuss my project with me; from experimental optimisation and preliminary results to final edits of figures and manuscripts for publication. For that and for creating such welcoming research groups, I am very grateful to you. Francesca, you have been the very best primary supervisor I could have asked for. Your positivity and enthusiasm have been infectious, and I have left many meetings with renewed energy and clear purpose for the next steps in my research. Thank you for your continued guidance from start to finish.

I have been fortunate enough to be part of three different research groups during my PhD. All of which have helped create a great work environment.

Thank you to the Biospec group and indeed the whole Biophysics group. To Krupakar for training me on the FTIR system when I first started. To Michael for our collaboration on the FTIR data analysis. To Ellen for training me on the WiTec. To Ben for 3D printing and MATLAB guidance. And to all of you, including Pascaline, Michelle, Fay, Toby, Skye, Beth, Anna, Ryan, Noemi, Dave, Alex $\times 2$, Hannah, Doriana, Jenni and everyone else for lunchtime TV, weekend walks and an altogether fun and diverse work atmosphere. Our varied academic backgrounds have always been treated as a great opportunity to give advice and help each other out - what a wonderful team to have been part of.

Thank you to the Chahwan group, especially to Emily, Laura, Laurence, Kevin, and Sally. All of you helped create a fun and encouraging lab environment. Thank you

in particular to Laura: you were the very first person at work I told I was pregnant. Your assistance in the lab with cell cycle inhibitors was invaluable and alleviated many worries - and your snacks alleviated my "morning" sickness. I am very grateful that we could continue working together when my maternity leave ended - the last two Chahwan group members left in Exeter!

Thank you to the Pagliara group, especially Ashley and Rosie for getting me started with microfluidics and Zehra for your input on combining microfluidics and Raman measurements.

Thank you to Dr Jeremy Metz for all your assistance with Python and image analysis.

Technicians and lab managers have also played a vital part by ensuring the running of the wet labs. Thank you especially to Chris, Agnes, Matt, and Steve - your hard work has been much appreciated.

I am also very grateful for my husband Chris and my son Alexander, who keep me sane. Chris, you have always supported me in all I do. You have always been happy to listen to my work worries and discuss any experimental problems I may have - and I have to admit that explaining the process to you has helped solve a problem or two.

Sidst men ikke mindst, skylder jeg også en stor tak til min mor og far. Tak fordi I gav mig troen på mig selv og modet til at følge mine ambitioner. Tak til min søster for altid at heppe på mig - og for at læse korrektur på min afhandling.

Publications

Articles

- **R. Brandstrup Morrish**, M. Hermes, J. Metz, N. Stone, S. Pagliara, R. Chahwan, F. Palombo, "Single Cell Imaging of Nuclear Architecture Changes" in *Frontiers in Cell and Developmental Biology* **2019**, Jul 24:7(141)

Reviews

- E. Sheppard, **R. Brandstrup Morrish**, M.J. Dillon, R. Leyland, R. Chahwan, "Epigenomic Modifications Mediating Antibody Maturation" in *Frontiers in Immunology* **2018**, Feb 26:9(355)
- M. Hermes, **R. Brandstrup Morrish**, L. Huot, L. Meng, S. Junaid, J. Tomko, G.R. Lloyd, W.T. Masselink, P. Tidemand-Lichtenberg, C. Pedersen, F. Palombo, N. Stone, "Mid-IR Hyperspectral Imaging for Label-free Histopathology and Cytology" in *Journal of Optics* **2018**, Jan 24:20(2)

Manuscripts in submission

- **R. Brandstrup Morrish**, K. H. W. Yim, S. Pagliara, F. Palombo, R. Chahwan, N. Stone, "Single cell label-free probing of chromatin dynamics during B lymphocyte maturation" in *Frontiers in Cell and Developmental Biology* **(2020: in submission)**
- S. Wang, K. Lee, Y. Zhang, C. Tang, S. Roa, **R. Brandstrup Morrish**, E. Pesenti, P. E. Cohen, T. MacCarthy, M. Scharff, W. Edelmann, R. Chahwan, "Dissecting the enzymatic and scaffolding functions of mammalian EXO1 in vivo" in *DNA repair* **(2020: in submission)**

Contents

List of Abbreviations

3'RR	3' Regulatory Region
AFM	Atomic Force Microscopy
AID	Activation-Induced cytidine Deaminase
AMR	Antimicrobial Resistance
bp	basepair
CSR	Class Switch Recombination
DSB	Double-Strand Break
ES cell	Embryonic Stem cell
FACT	Facilitates Chromatin Transactions
FSC	Forward Scatter
FTIR	Fourier Transform Infrared
H3K4me3	Trimethylation of histone 3 lysine 4
Ig	Immunoglobulin
LDA	Linear Discriminant Analysis
LINC	Linker of Cytoskeleton and Nucleoskeleton
ncRNA	non-coding RNA
SHM	Somatic HyperMutation
SSC	Side scatter
PCA	Principal Component Analysis
PFA	Paraformaldehyde
PLS	Partial Least Squares
RT-DC	Real-time Deformability Cytometry
SUMO	Small Ubiquitin-like Modifier
V(D)J	Variable (Diverse) Joining DNA segments
VIP	Variable Importance in Projection

List of Figures

List of Tables

1. Introduction

The following chapter contains sections of the papers "Single Cell Imaging of Nuclear Architecture Changes"[1], and "Single Cell Label-free Probing of Chromatin Dynamics during B Lymphocyte Maturation"[2].

The ability to probe and quantify intracellular changes during cellular development can enable the characterisation of cells during differentiation, in response to extracellular cues, or during disease progression. This characterisation could aid in early disease detection, treatment decisions and monitoring, as well as expand our knowledge of changes in healthy and diseased cells. The nucleus and its components are the primary instigators of intracellular changes, and thus, in the pursuit of phenotypic characterisation of single cells, measurements and quantification of biochemical and biophysical properties of the nucleus have great potential.

1.1. Chromatin

The nucleus of a cell is packed with strings of DNA, the genetic code that forms the basis for cell survival and function. A wide array of molecules within the nucleus participate in the control of gene expression and genomic maintenance. This is largely orchestrated through the macromolecular complex known as chromatin, which primarily consists of genomic DNA wound around histones (Figure 1.1). The structure and dynamics of chromatin which are regulated through chemical and conformational changes, are vital for normal cell functions[3, 4].

1.1.1. Biochemical pathways modulate chromatin

A multitude of biochemical and molecular signalling cascades orchestrate changes to chromatin and thereby transcription patterns[5–8]. These signalling cascades are often composed of numerous steps that include protein modifications and protein complex assembly, leading to accumulation of transcription factors and co-activators in

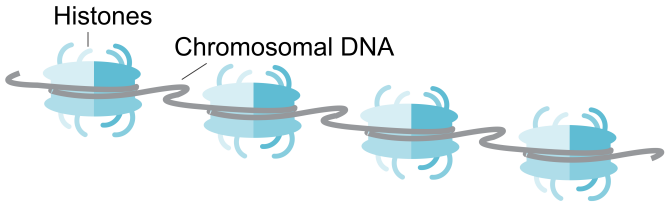

Figure 1.1.: *Schematic representation of chromatin.*
Chromatin is a macromolecular complex, consisting of genomic DNA wound around histone (protein) octamers.

the nucleus. Additionally, they induce chromatin remodelling through histone modifications - modifying access to promoter regions of specific genes or entire chromosomal regions. Types of histone modifications are numerous and include phosphorylation, acetylation, methylation, ubiquitination, and SUMOylation. Some serve as anchor points for regulatory proteins, and their exact position in the amino acid sequence is often vital for their function[9–13]. Modifications of DNA, namely methylation, further regulate gene expression[14].

1.1.2. Mechanotransduction

In addition to biochemical signalling, mechanotransduction, which enables an external load applied to a cell to impact gene transcription[15], also mediates cellular changes. It likely also plays a central role in the alterations of chromatin architecture. This signalling mechanism is thought to be mediated by Linker of Cytoskeleton and Nucleoskeleton (LINC) complexes, which have been implicated in a range of human diseases[16]. Yet the mechanisms involved in the interaction between cytoskeleton and nucleus during mechanotransduction have not yet been fully elucidated[17–20].

Nuclear components, which have been deemed important in mechanotranduction, include nuclear lamins, i.e. fibrous proteins that interact with the inner nuclear membrane proteins to form the nuclear lamina on the interior of the nuclear envelope. They are the main structural components of the nuclear envelope [21, 22]. The LINC complexes directly link the cytoskeleton to nuclear lamins[23] and chromatin[24, 25]. Lamin-A/C in particular plays a key role and has been shown to affect the stiffness of the nucleus[26]. Mutations or deficiencies in lamin-A/C lead to inadequate response to mechanical stimuli[27–29].

1.2. B lymphocytes

A suitable cell model for the study of large-scale chromatin conformational changes may be found in the form of B lymphocytes. These are immune cells with a large nucleus to cytoplasm ratio, which makes them well suited for both clinical and experimental studies.

The ability to identify and destroy invading pathogens is essential for the survival of any organism. Of particular interest are adaptive immune systems, which allow the host to recognise pathogens upon subsequent encounters and quickly deploy an adequate immune response. These systems depend on alterations to the host genome, most of which are irreversible. Complex regulatory processes are therefore involved.

The immune mechanism employed by a given organism largely depends on the different types of pathogens they can expect to encounter. The vertebrate immune system largely relies on the recognition of pathogenic protein, lipid, and sugar moieties. This is achieved through antibodies, or immunoglobulins (Ig), produced by B cells[30].

In order to produce a large and expandable repertoire of antibodies, DNA alterations at the Ig locus are prominent during two developmental stages of B cell maturation. These alterations include reorganisation and mutation of the DNA, and unsurprisingly they are tightly regulated processes[9, 31, 32]. Without the intentional DNA damage the organism will suffer with immune deficiencies, and thus become susceptible to invading pathogens. Conversely, increased or uncontrolled DNA damage can cause accumulation of mutations in the host genome, which may lead to cancerous growth[33].

1.2.1. Antibody diversification in B cells

The primary antibody diversification is known as V(D)J recombination, because it involves the rearrangement of the variable (V), joining (J) and diverse (D) DNA segments to make up the variable region of the Ig gene (Figure 1.2A). The variable region is responsible for antigen binding in the final antibody protein. After the initial diversification, naïve B cells are capable of producing a large variety of antibodies. However, their antigen affinities remain low. Furthermore, they are only capable of expressing the same precursory effector region, restricting their effector functions. The effector region determines both the mechanism of pathogen elimination and the antibody localisation in the body[34].

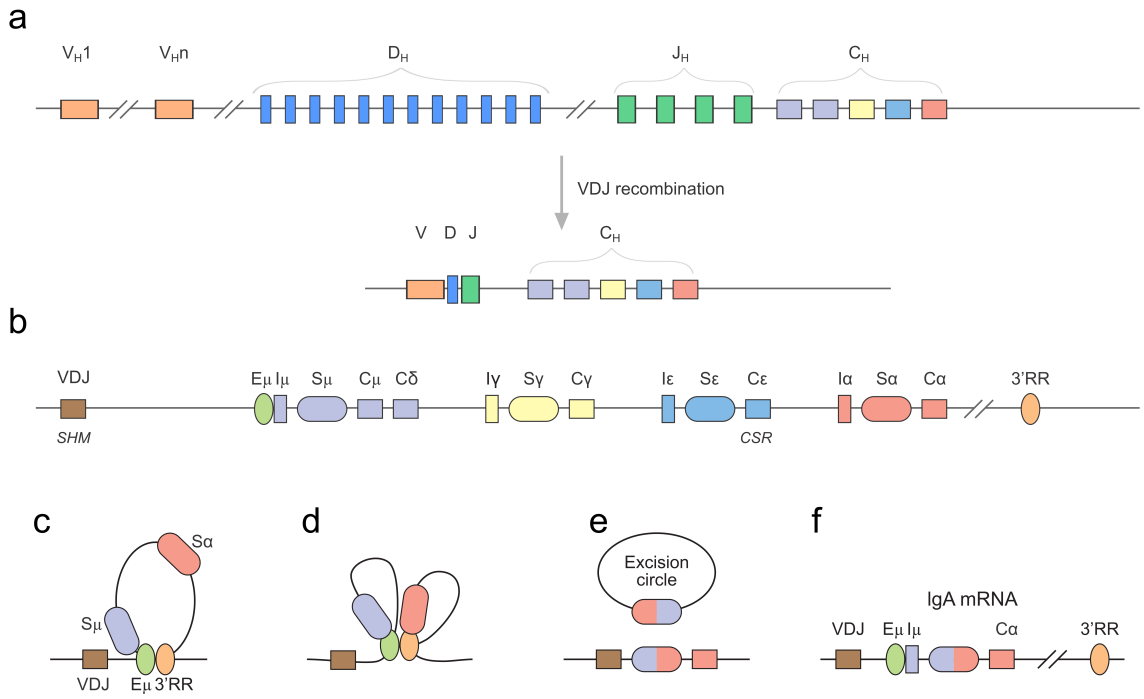

Figure 1.2.: *Reorganisation and mutation of DNA at the Ig locus.*
(a) *The Ig locus undergoing VDJ recombination.* ***(b-f)*** *The Ig locus undergoing class switch recombination (CSR).* ***(b)*** *An expanded view of the Ig locus showing regulatory elements Eμ and 3' regulatory region (3'RR), as well as the intervening regions, I_H, and switch regions, S_H, preceding each constant region. The double-strand breaks occur in the switch regions during CSR.* ***(c)*** *and* ***(d)*** *The Eμ enhances associates with the 3'RR, bringing switch regions into close proximity.* ***(e)*** *CSR occurs when the double-strand breaks (DSBs) are repaired in such a way that the DNA segment between the two switch regions is lost. (f) The Ig locus after CSR; now expressing the IgA antibody.*

Secondary antibody diversification rectifies both of these shortcomings. Activation of naïve B cells occurs through antigen engagement and cytokine stimulation[35]. The activated B cells relocate to germinal centres in secondary lymphoid tissue[36]. Secondary antibody diversification consists of two processes, both of which are initiated by the small mutator protein activation-induced cytidine deaminase (AID). Deamination of cytosines by AID results in U:G mismatches in the DNA sequence[37].

In the variable region of the Ig locus, the U:G mismatches lead to the process of somatic hypermutation (SHM), which is characterised by an accumulation of mutations within the region. Indeed, the mutation rate in the region increases to 10^{-3} mutations per base pair per cell division, which is 10^6 times higher than the background mutation rate of the cells[38, 39]. The accumulation of mutations results in alterations of the tertiary structure of the antibody, allowing increased affinity for encountered antigens.

All four bases are targeted during SHM; C:G and A:T pairs are targeted approximately equally[39, 40]. Although only C:G pairs are directly altered by AID, both depend on AID activity[41]. The targeting of A:T pairs further depend on the mismatch repair machinery; in particular Msh2 and Msh6[42–44]. It has been proposed that the Msh2-Msh6 heterodimer exerts its function through recognition of the AID-generated U:G mismatches and subsequent recruitment of low-fidelity polymerases[44, 45].

AID induced U:G mismatches in switch regions, found upstream of the various effector domains, result in DNA double-strand breaks (DSBs) and recombination of DNA segments (Figure 1.2). This process is known as class-switch recombination (CSR) or isotype switching, because it results in the expression of antibodies with a different constant region. Specific switch regions are targeted by AID depending on cytokine induction type[46], and DSBs are formed.

Efficient CSR depends on chromatin looping involving domains of the 3' regulatory region (3'RR) of the Ig locus (Figure 1.2)[47, 48]. This chromatin looping brings the switch regions into close proximity (Figure 1.2C-D). This allows for repair of the DSBs in such a way that the DNA segment between the two switch regions is lost in the process (Figure 1.2E)[49]. Figure 1.2B-F shows a representation of isotype switching from IgM to IgA.

1.2.2. Chromatin modifications and remodelling are essential for successful antibody diversification

It is apparent that secondary antibody diversification involves major changes to the genome, both in terms of conformational changes and direct changes to the DNA sequence (see previous subsection 1.2.1). However, these are just the beginning of the changes at the Ig locus region. Significant chemical changes also occur at the chromatin level in the shape of histone modifications[9]. Recruitment of a myriad of DNA damage response proteins accounts for further changes[50, 51]. Other factors, such as noncoding RNAs, also play a regulatory role[52]. Figure 1.3[9] depicts the chromatin modifications that have been correlated with different stages of secondary antibody diversification. Some of the proteins recruited to the chromatin modifications are also marked.

Trimethylation of histone 3 lysine 4 (H3K4me3) is required for recruitment of AID to both the variable regions and switch regions[53–55]. Regulation of this histone mark occurs through the facilitates chromatin transactions (FACT) complex[55], as well as the histone chaperone Spt6[53]. Additional marks have been implicated in the recruitment of AID. These include H3K9me3 and H3K9ac[56], as well as the combinatorial mark H3K9acS10ph[13].

Other histone modifications have been linked to the resolution of the AID induced DNA damage. Certain repair proteins required for SHM and CSR are recruited through these histone modifications.

The low-fidelity polymerase Polη is essential for the generation of A:T mutations in SHM[57]. Ubiquitination of H2AK119 and H2BK120 has been associated with the variable region and co-localise with Polη[58]. Polη is known to possess an ubiquitin binding domain[59, 60].

In successful CSR, most chromatin modifications are involved in the recruitment of 53BP1, a protein essential for the repair of DNA DSBs[61, 62]. This is not surprising, as unrepaired DNA DSBs are detrimental to cell survival. Recruitment of 53BP1 involves several signalling pathways that include ubiquitination, acetylation, methylation and phosphorylation of histones.

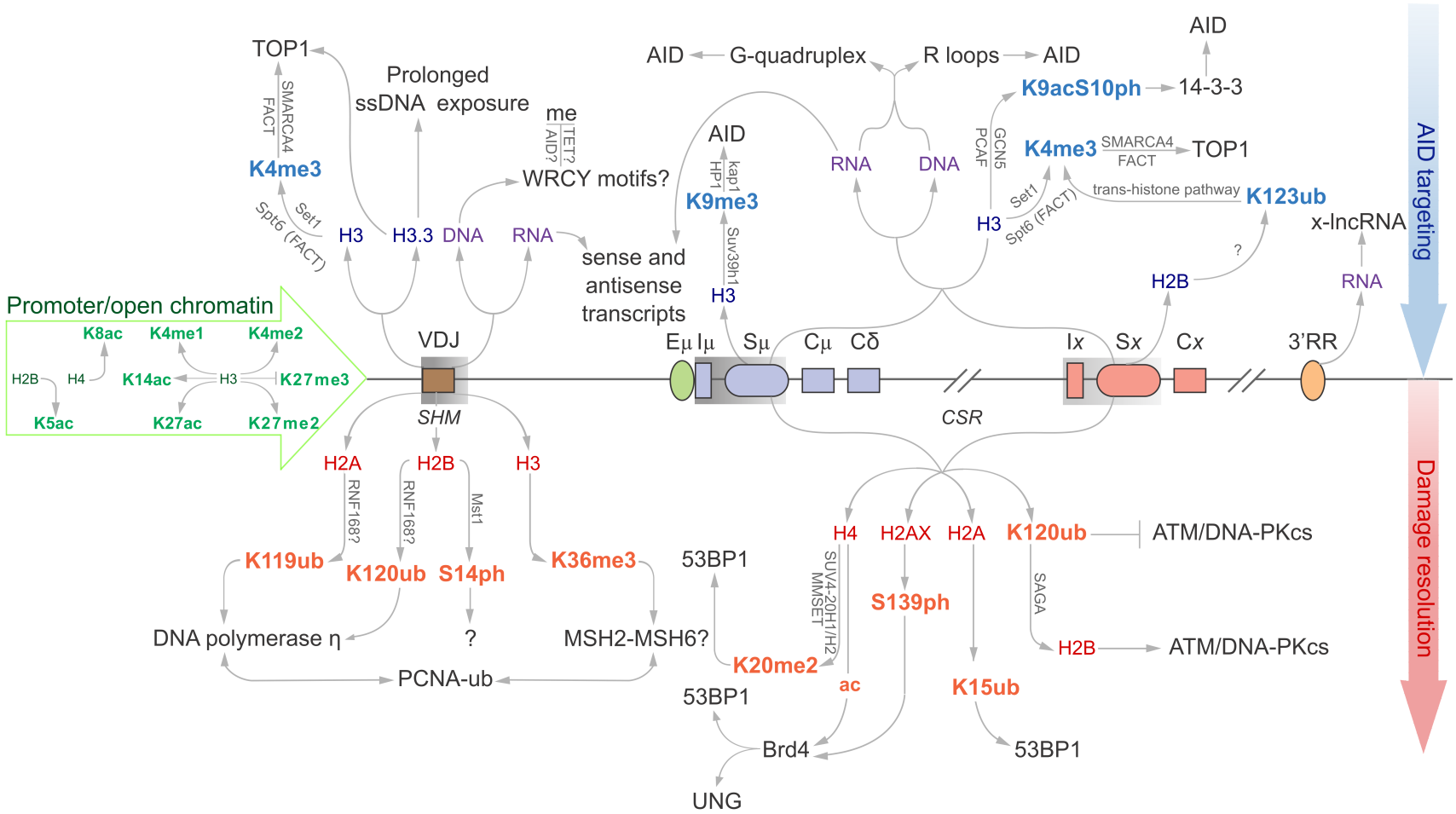

Figure 1.3.: *Epigenomic modifications directing antibody diversification processes SHM and CSR.*
Reproduced from [9]. Green core histones and associated modifications are involved in chromatin de-compaction and enable transcription through the Ig locus. All factors above the locus are important for the generation of DSBs while everything below encourages mutagenic repair at the V region, and DSB repair at donor and acceptor S regions (Sμ and Sx, respectively). Blue histones and affiliated modifications help recruit or tether AID and other factors that facilitate production of DSBs. Purple DNA and RNA are linked with sequences and structures that facilitate AID recruitment or targeting. Red core histones and accessory modifications recruit DNA repair proteins to ensure excision of intervening CH region for successful class switching as well as error-prone polymerases to the V region. Modifications include ubiquitination (ub), phosphorylation (ph), methylation (me) and acetylation (ac).

From the recruitment of AID to the repair and/or attenuation of the AID induced DNA damage, both SHM and CSR are in large part orchestrated by chromatin modifications. Indeed, some have even been proposed to function as anchors for protein platforms that retain important factors at the site of damage[63, 64]. Furthermore, proteins responsible for chromatin modifications, so-called chromatin modifiers, have been found to be mutated in >5% of B-cell lymphomas[65]. It is clear that major chemical changes at the Ig locus take place during antibody diversification. Indeed, the entire chromatin proteome changes.

In addition to these Ig locus specific chromatin modifications, large-scale chromatin changes also occur across the genome, namely histone acetylation as the cells undergo an increase in size and RNA synthesis and accelerated proliferation[66].

1.2.3. Cell-to-cell interactions define a successful immune response

Despite our knowledge of the factors involved in B cell activation and secondary antibody diversification, we cannot replicate it *ex vivo*. Class switch recombination can be induced in primary B cells *ex vivo* after isolation from mouse spleens[67], but SHM is more difficult to induce[68]. Cultured cell lines are not capable of producing a diverse set of antibodies like the fully functioning immune system can. The murine cell line CH12F3-2A is the most commonly used model for CSR, but SHM does not occur in this cell line. Conversely, the human cell line Ramos can be used for modelling SHM, but it has low CSR capability[69]. These discrepancies are perplexing and poorly understood. The requirement of the entire immune system in its endogenous environment of for example a mouse, implies that cell-to-cell interactions are important for successful antibody diversification. Secreted cytokines and other signals are simply not enough.

The *in vivo* setting for secondary antibody diversification is the germinal centre. Activation of naïve B cells, through the interaction with antigens, is followed by aggregation of B cells in secondary lymphoid organs, where they form germinal centres[36]. A germinal centre can be subdivided into the dark zone and the light zone.

In the dark zone, SHM is the primary reaction taking place. In the light zone, B cells undergo CSR and interact with other immune cells, such as follicular dendritic cells and T cells. The fate of the B cells is largely determined by the antigen affinity of their antibodies. This includes re-entry into the dark zone for further SHM as well

as differentiation into a plasma cell or memory cell. Finally, B cells with unsuitable antigen affinity go through apoptosis[36].

Direct cell-to-cell signalling appears to play an important in secondary antibody diversification. The exchange of miRNAs through exosome shuttles between B cells and T cells[70–72], stresses the need for the presence of a more intact immune system. However, the exchange of chemo signals may not tell the whole story. Evidence is emerging that mechanical forces exerted by cells onto adjacent cells have a direct role in the immune response.

As has been known for a long time, germinal centres are densely packed[73]. The mechanical forces exerted by a cell onto its neighbouring cells could potentially mediate cell-to-cell signalling. Recent studies have indeed revealed that mechanical stress instigates certain cellular processes. In B cells, activation through antigen contact with receptors has been shown to have a mechanical threshold. Furthermore, the isotypes IgM, IgG and IgE exhibit different sensitivities and thresholds[74]. T cells have been shown to use mechanical forces to promote the destruction of target cells[75]. Evidence from non-immune cells, especially studies showing regulation of chromatin and transcription through mechanical cell manipulation[15, 76], further supports the likelihood of a central role played by mechanical forces in the immune response. Hence, chemo-mechanical assays that provide the ability to correlate these aspects of cellular response are particularly relevant.

1.3. Vibrational spectroscopy

Chemical imaging methods based on vibrational spectroscopy, such as Fourier Transform Infrared (FTIR) and Raman spectroscopy, provide non-invasive and spatially resolved tools for investigating biological samples including single cells. They provide information on chemical composition and structure on a subcellular scale. The techniques exploit changes in vibrational energy levels of molecules exposed to light of particular wavelengths, in the IR or visible range. Each vibrational (FTIR or Raman) spectrum is a 'chemical fingerprint' of the material in that it contains information on the identity, structure and quantity of molecules in a sample.

1.3.1. Cell analysis using FTIR and Raman microscopy

The application of FTIR and Raman microscopy on single cells can provide information about numerous intracellular processes. Monitoring and quantification of changes to specific biomolecules during cellular processes have been shown for both techniques. These include changes to intracellular DNA levels during cell cycle progression[77–80]. In FTIR imaging, the peaks at ∼1080 cm^{-1} and ∼1240 cm^{-1}, both relating to nucleic acids, have shown marked changes. In agreement with cell growth during cell cycle progression, additional spectral changes were seen in lipid and protein peaks[77, 78]. Raman spectra have shown changes in the nucleic acid, lipid and protein regions as well[79, 80].

Modifications of specific biomolecules have also been monitored. A number of studies have found FTIR spectral signatures of radiation induced DNA damage, through cell measurements[81–84] and measurements of isolated DNA from radiation exposed cells[85]. Several spectral features have been identified in these studies. Common for most were changes to the asymmetrical and symmetrical O-P-O stretching modes (∼1240 cm^{-1} and ∼1080 cm^{-1}). Importantly, they have been found in both extracted DNA and whole cell measurements. Other studies monitored protein modifications, in particular histone acetylation levels and changes to these induced by HDAC inhibitors[86, 87]. FTIR peak ratios proved useful for monitoring these changes.

Both FTIR and Raman have also been used to characterise phenotypic changes in cells. These come with large-scale changes to the trancriptomic and proteomic profiles of the cells, resulting in spectral differences between cell populations. Multivariate analysis is often used for discrimination between cell types or treatments. Immune cell activation states and immune cell response to pathogens are of interest for a large number of disease states, and some progress in characterising these have been made[88–98]. Discrimination of lymphocytes from other white blood cells has been explored[99, 100], so has discrimination between lymphocytes[96, 97].

B and T cells are difficult to differentiate using other label-free techniques which cannot probe the chemical composition, as morphologically these cells are nearly identical. Using Raman spectroscopy, Hobro et al were able to detect biochemical differences between these cell types, and partial least squares discriminant analysis allowed for classification of multiple B and T cell lines[97]. Ichimura et al have also used Raman spectroscopy to discriminate between B cells and T cells[96]. Further, they visualised the activation status of T cells. By examining a number of time points,

they found that the spectral changes between cells reflected the global changes in cell state upon activation[96]. Similarly macrophage activation can also be detected using Raman spectroscopy[98]. Importantly, the spectral indicators of activation were linked to upstream intracellular changes, again demonstrating the potential of Raman spectroscopy in characterising phenotypic cell changes.

A number of studies have used FTIR spectroscopy to examine lymphocytes and their activation[88, 89, 94]. These revealed spectral differences between nonactivated and activated B cells, primarily in the low wavenumber region. Several peaks associated with nucleic acids exhibited changes, including $\nu_{as}PO_2^-$ ($\sim$1244cm^{-1}) and $\nu_sPO_2^-$ ($\sim$1080cm^{-1}). Mazur et al further demonstrated the clinical potential of peaks in the 1000-1200 cm^{-1} region by differentiating between a number of cancers based on spectral profiles of B lymphocytes from germinal centres in lymph nodes adjacent to the cancers. With no metastatic cells present in the lymph nodes, the immune activation provided the marker for disease[94].

1.3.2. Correlation between Raman spectra and transcriptomic data

It is becoming apparent that, although it is possible to identify specific peaks associated with intracellular biochemical changes, a whole range of subtle spectral changes characterise cell state changes, such as immune activation. This is not surprising, as cellular responses induce a swarm of transcriptional up- and downregulation orchestrating changes to the transcriptomic and proteomic profile of the cell. Using multivariate analysis, spectral information enables classification of cell states or phenotypes of mammalian cells as seen in the previous section, but also of yeast and bacterial cells[101, 102]. It is this label-free classification that has great potential both in i) clinical settings, for disease diagnosis and prognosis, and ii) in biomedical research, for example through cell sorting for downstream processes. How powerful this tool can be, depends upon our understanding of the correlation between the spectral output and the underlying biochemical pathways within the cells.

In bacterial research, antimicrobial resistance (AMR) is of great interest. Spectral markers of antibiotic resistance have been identified at the population level[101], and more recently a correlation between peak intensities and expression levels of antibiotic resistance contributing genes has been found[101]. Importantly, this was done in the absence of antibiotics, indicating that the transcriptional profile of the given cells, rather than their phenotypic response to the presence of antibiotics, were responsible

for the spectral signatures. This correlation between Raman spectra and transcriptomic data has further been explored in a comprehensive manner in yeast, where it has been shown that Raman spectra and transcriptomic data are linearly correlated[102]. In both yeast and bacterial cells, several environmental conditions whave been examined. A linear transformation matrix describing the relationship between the Raman data and the transcriptomic data, made it possible to predict a environment-specific Raman spectrum based on transcriptomic data. Conversely, the transcriptome of a specific environment was predicted based on the Raman data[102].

Transcriptomic readouts consist of thousands of RNA transcripts, whereas Raman spectroscopy can measure the phenotypic expression of the RNA transcripts, i.e. the biochemical result of the transcriptomic profile. All transcripts do not change indenpendently; instead, strong correlations are found between transcripts that are controlled by global regulators, reflected in the Raman signals. In the yeast study, it has been determined that only 17 transcripts were sufficient for determining a linear correlation with the Raman spectra. The transcripts largely responsible for the linear correspondence with the Raman spectra have been identified by determining the variable importance in projection (VIP) values for each transcript. The top scoring transcripts are primarily non-coding RNAs in yeast and ribosome-related transcripts in bacteria[102].

1.3.3. Live cell analysis using FTIR imaging and Raman mapping

Sample preparation is of great importance for all scientific methods, especially in regards to consistency. For FTIR and Raman measurements, the choice between applying fixatives or measuring live cells is of special interest for the interpretation of the spectra. There are pros and cons for both approaches. Fixatives preserve the sample, but introduce artefacts of their own as they interact with the biomolecules of the cells[81, 103–106]. Live cell measurements circumvent these and enable measurements of hydrated cells. Depending on the setup, they may also allow for real-time measurements of some biological processes. However, they come with technical challenges.

For FTIR measurements, the presence of water is generally seen as a disadvantage because of its strong IR absorption. Attenuated total reflection (ATR) mode measurements can overcome this[107–110]. Only a few micrometres into the cell is probed during these measurements, thus avoiding the medium above the cells, but potentially

missing the inner part e.g. nucleus. For transmission measurements, which capture the entirety of the sample, reducing the optical pathlength is necessary. Sandwiching the cells between two substrates can accomplish this[111–113], however this does not allow for the maintenance of the cellular environment. Microfluidic approaches allow for better control. Choice of device material should take into consideration biocompatibility, microfabrication techniques and FTIR transparency regions. Materials that are fully transparent in both visible and MIR regions, such as calcium fluoride[114–117] and barium fluoride[118], are good choices - with calcium fluoride being more biocompatible, as it is non-toxic and inert to organic chemicals. Although drilling and surface modifications enable flow and bespoke structures, the cost of materials make large-scale productions of these devices impractical. Contrarily to FTIR, the water contribution to the Raman spectrum is a minor problem, so there are fewer challenges for live cell Raman measurements[119]. A heated enclosure is still needed for time-course experiments, in order to maintain a suitable environment for the cells. Choice of laser wavelength for illumination is also a factor. Wavelengths outside the visible range are thought to be superior for live cell measurements, as they result in reduced phototoxicity[120, 121] and increased depth of penetration.

1.4. Mechanical measurements

In addition to biochemical markers, the biomechanical properties of cells and cellular components can also facilitate characterisation of specific cell states. The biological relevance of such measurements was introduced in subsection 1.1.2. Mechanical properties of a cell can be assessed in a number of ways[122], such as atomic force microscopy (AFM)[123], micropipette aspiration[26], microbead rheometry[15] and real-time deformability cytometry (RT-DC)[124, 125]. Direct contact with the cell is required for most techniques, in order to apply mechanical stress. A notable exemption to this is Brillouin spectroscopy, which probes the true elastic stiffness[126]. There is a lack of standards across all these techniques[127], and direct comparisons between them are therefore difficult. However, general trends regarding stiffness and deformability are still apparent.

1.4.1. Mechanical properties of the nucleus

Studies performed on isolated nuclei[128, 129] and nuclei in cells[26, 123, 130, 131] - with intact cytoskeleton and links between cell surface and nucleus - have examined

nuclear mechanical properties. Embryonic Stem (ES) cells and other progenitor cells are often chosen as models, as the properties of the nucleus change during the differentiation. Indeed, stem cell nuclei are found to be softer and more deformable than differentiated cell nuclei[26, 130].

This variation in nuclear properties is correlated with chromatin structure[126, 130, 131] and nuclear lamins[26]. Specifically, chromatin decondensation is correlated with softening of the nucleus. For instance, treatment with Trichostatin A (TSA), which instigates decondensation of the chromatin through hyperacetylation of histones, induces nuclear softening[126, 131]. In ES cells, priming for differentiation through Nanog downregulation, induces chromatin decondensation and a softening of the nucleus[130]. The role of nuclear lamins is centered around lamin A/C. Indeed, knockdown of lamin A/C in human epithelial cells softens the nucleus to an ES comparable level[26]. It is thus unsurprising that nuclei of primed ES cells, which have decondensed chromatin and low lamin A/C expression levels, are softer than nuclei of differentiated cells, which have more organised and condensed chromatin and upregulated lamin A/C expression.

1.4.2. Microfluidics

Microfluidics is the term given to technology allowing the manipulation of fluids on a submillimetre scale[132–134]. It facilitates high throughput collection of single cell data, which has the potential to reveal details that population-averaged data cannot by reducing stochasticity caused noise[135–139]. For biomechanical cell and nuclei measurements - single cell analysis being the only option - it is particularly useful. It forms the basis of real-time deformability cytometry, which has primarily been used to investigate whole cell deformability[122, 125, 140–148].

Mechanical characterisation of peripheral blood cells enables identification of different cell types and disease states[144, 148]. Erythrocyte pathologies, such as malaria infection, are detectable by mechanical characterisation of blood cells. Leukocyte activation, through *in vivo* and *in vitro* infection, can also be identified. Additionally, leukemia patients have differing profiles to those of healthy patients, and cell deformation and size can be used to monitor treatment and its success. With measuring rates of 1000 cells/sec and the ability to analyse whole blood without purification, mechanical characterisation of cells by real-time deformability cytometry has great clinical potential.

1.4.3. Nuclear auxeticity

The previous sections showed that deformability and stiffness are important properties of cells and nuclei with both clinical and biological relevance, and that microfluidics can be an important tool for rapid measurements. Combining deformability cytometry with fluorescence imaging enables high-throughput analysis of *nuclear* mechanical properties[124].

Using both atomic force microscopy and deformability cytometry, Pagliara et al showed that ES cells transitioning from a naïve state to a differentiation priming state have auxetic nuclei. Auxeticity is a mechanical property of materials with a negative Poisson's ratio. While naïve and differentiation priming ES cell nuclei become thinner when stretched, the auxetic nuclei of transitioning ES cells instead expand perpendicularly to the stretching forces. It was determined that this auxetic phenotype, which had not previously been seen in cells, is regulated by the chromatin condensation state. Transitioning ES cells exhibit less condensed chromatin compared with naïve and differentiation priming ES cells. Treating naïve ES cells with TSA, and thus inducing global chromatin decondensation, caused the nuclei to become auxetic[124].

Together, this introduces nuclear auxeticity as a possible factor in mechanotranduction, perhaps a modulator of a nucleus' sensitivity to mechanical cues. Further, nuclear auxeticity is a novel biomechanical property that could be used - on its own or in combination with other biomechanical properties - for mechanical phenotyping of cells, be it for research or clinical purposes. To further explore this, its relevance in other cell types will need to be examined.

1.5. Research objectives

In summary, this chapter has gone some way to illustrate the importance of chromatin changes, whether they are initiated through biochemical or mechanical signalling, and how B cells are both an excellent model for studying these changes and of clinical interest themselves. As the chromatin changes lead to transcriptional up- and down-regulation, determining cell fate, properties of the nucleus (chromatin condensation state, stiffness or other mechanical properties of the nucleus) could be key markers for phenotypic characterisation of single cells. Doing this in a rapid and/or label-free manner has great potential in both clinical and research settings. Exploring

novel techniques for assessing and quantifying these properties is key if this is to be achieved. Therefore, three objectives lay the foundation for this thesis.

The first objective is to monitor global chromatin changes within cells. Major changes in chromatin structure and chemistry cannot be assessed solely based on the measurements of specific post-translational modifications of histones. Overall structure and chemistry and changes herein are also of interest.

The second objective concerns exertion of mechanical stress to cells during measurement. This will enable the investigation of mechanical forces as instigators of or contributors to antibody diversification.

The third objective concerns single cell measurements of live cells. Fixatives can introduce their own artefacts - live cell measurements circumvent this limitation. Further measuring the chemical and physical properties of a single cell before and after treatment or mechanical stimuli will account for stochastic differences in for example protein concentrations between cells and potentially reveal patterns hidden in population-averaged measurements.

The fourth objective is to examine the correlation between Raman spectral data and transcriptomic data. This correlation is instrumental in unravelling the underlying biochemical structures and pathways that affect Raman spectra.

1.5.1. Thesis outline

Figure 1.4 provides an overview of the biological system studied in this thesis, which will assess and quantify nucleus properties, exploring the use of novel methods. In chapter 2 information on methods and materials is presented, along with theoretical background of the experimental techniques.

The following four chapters, chapter 3, chapter 4, chapter 5 and chapter 6, are result chapters, each focusing on one experimental approach. FTIR imaging of chromatin changes is the focus of chapter 3 and deformability cytometry for studies of nuclear mechanical properties the focus of chapter 4. Live cell vibrational spectroscopy measurements is the focus of chapter 5 and chapter 6, with chapter 5 focusing on technical optimisation and chapter 6 focusing on Raman mapping of chromatin and transcriptional changes in live cells. Conclusions are found at the end of each of these chapters.

One publication and one manuscript in submission form the basis of chapter 3, chapter 4, and chapter 6. In chapter 7 summarising discussions and conclusions covering the whole thesis are presented along with future perspectives.

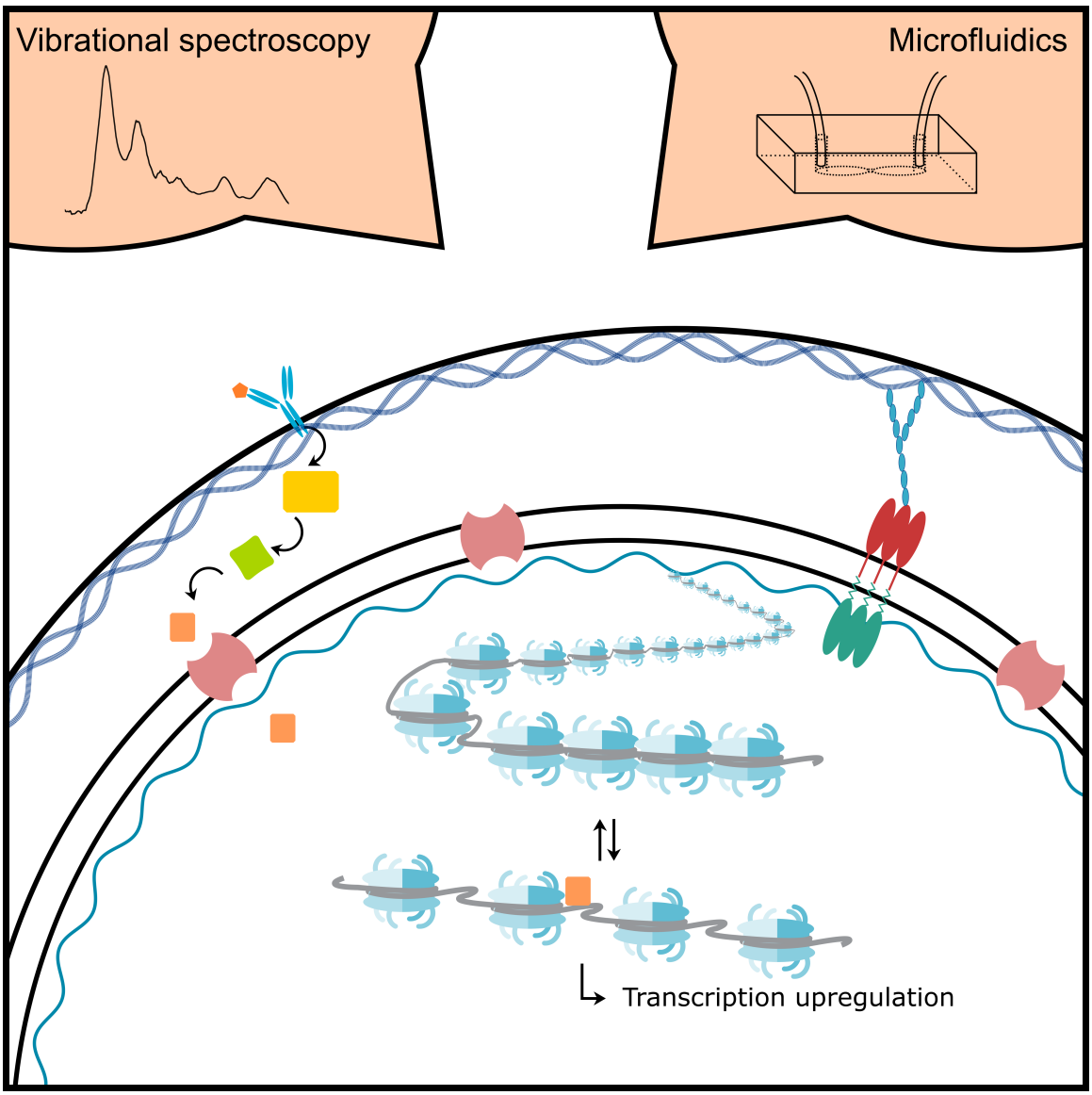

Figure 1.4.: *Thesis graphical summary.*
This thesis focuses on the intracellular regulation and signalling that results in chromatin changes which in turn lead to the transcriptional changes that determine cell fate. Both biochemical signalling and mechanotransduction play a role, and as such chemical as well as mechanical measurements are needed to shed light on these processes. Varying combinations of vibrational spectroscopy and microfluidics were used to explore these, as outlined in subsection 1.5.1.

2. Materials and Methods

The following chapter contains sections of the paper "Single Cell Imaging of Nuclear Architecture Changes"[1] and the manuscript "Single Cell Label-free Probing of Chromatin Dynamics during B Lymphocyte Maturation"[2].

2.1. Cell culture and cell treatments

2.1.1. CH12F3-2A cell culture

CH12F3-2A cells, originally acquired from Dr Matthew Scharff (Albert Einstein College of Medicine, NY, USA), were grown in HyClone^{TM} RPMI 1640 medium (GE Healthcare Life Sciences, SH30096.01) with 10% Fetal Bovine Serum (Gibco^{TM}, 16140071), 5% NCTC-109 (Gibco^{TM}, 21340039), 1% Pen-Strep (Gibco^{TM}, 10378016), 1% Glutamine (Gibco^{TM}, 25030024), 1% Sodium Pyruvate (Gibco^{TM}, 11360070) and 50 μM β-mercaptoethanol (Gibco^{TM}, 31350010).

2.1.2. Animals

Barrier bred 8 weeks old female C57/BL6 mice were obtained post-mortem from the Biological Services Unit, Living Systems Institute (University of Exeter), as part of the facility's maintenance culling protocol; thereby circumventing the need for additional ethical approval. Cells were extracted from the spleen, and B cells were isolated using EasySep^{TM} Mouse B Cell Isolation Kit (Stemcell Technologies, 19854). The isolated B cells were grown in HyClone^{TM} RPMI 1640 medium (GE Healthcare Life Sciences, SH30096.01) with 10% Fetal Bovine Serum, 1% Pen-Strep, 2% Glutamine and 50 μM β-mercaptoethanol.

2.1.3. Cell treatments

For cell cycle experiments, cells were stalled in S phase and G2/M phase, using 0.1mM Hydroxyurea (Sigma-Aldrich, H8627-1G) for 20 hours and 10 ng/ml Nocodazole (Sigma-Aldrich, M1404-2MG) for 8 hours, respectively.

For the chromatin conformation experiments, cells were incubated with 10nM Trichostatin A (Sigma-Aldrich, T8552-1MG) for 24 hours to inhibit HDAC activity and thus induce hyperacetylation and decondensation of the chromatin.

For immune activation, CH12F3-2A cells were incubated with a cytokine cocktail (CIT) consisting of 2.5 μg/ml anti-CD40 (BD Biosciences, 553788), 10 ng/ml IL-4 (R&D Systems, 404-ML-050) and 50 ng/ml TGFβ (R&D Systems, 240-B-010). Primary cells were incubated with 5 μg/ml Lipopolysaccharide solution (Invitrogen^{TM}, 15526286) and 10 ng/ml IL-4. Class switch recombination was assessed by IgM to IgA switching for CH12F3-2A cells, and IgM to IgG1 switching for primary B cells.

2.2. Microfluidic devices

Fluorescent imaging (section 2.7) and spectroscopic mapping (section 2.5) were applied to live cells within microfluidic devices. The designs of these chips are presented in section 4.2 and subsection 5.3.1.

2.2.1. Microfluidic device preparation

Microfluidic chip silicon moulds were designed and fabricated by Dr Stefano Pagliara and Dr Zehra Kahveci as previously reported[124, 149, 150]. A negative mould was prepared through replica moulding with PDMS (DOWSIL^{TM} 184 Silicone Elastomer Kit), 9:1 ratio of base to curing agent, in a small container. Once bubble-free, the PDMS was heated at 70°C for one hour. The PDMS chip was cut to size using a scalpel, and the inlet and outlet were cyt through with a 1.5mm biopsy punch (Miltex, 33-31A-9/25).

The chip was bonded to a glass coverslip using surface ionisation by oxygen plasma treatment (10 second exposure to 30W plasma power in 1 mbar air, Diener Royal Oak).

2.2.2. Epoxy mould

Epoxy moulds of multiple chips were prepared in petri dishes, using Loctite Hysol 9483. Epoxy moulds are less fragile than silicon moulds, and allow for multiple identical chips to be made simultaneously.

PDMS chips were placed, pattern facing up, in a layer of liquid PDMS and baked at 65°C for one hour. PDMS was added until level with the chips and baked at 65°C for another hour. Loctite Hysol 9483 was added on top in a fume hood and degassed in a dessicator until bubble-free. The epoxy mould was left to solidify at room temperature for 24 hours. The bottom of the petri dish was cut out using a drill and the PDMS chips were cut out revealing the epoxy mould.

2.3. Flow cytometry

Flow cytometry is a microfluidics and laser based technique that allows for automatic, high-throughput single cell measurements. Standard measurement rates are several hundred cells per second. Cells are passed single-file through a light beam, and optical parametres are measured. A number of detectors enable measurements of forward scatter (FSC), side scatter (SSC) and a selection of fluorescence signals, which vary dependent on the instrument[151]. For each detected signal, height, width and area are quantified.

FSC is measured by a detector in line with the light source. The intensity depends on the size of a cell, and FSC is therefore used to discriminate between cells by size. SSC is measured by a detector perpendicular to the laser. The granularity of a cell affects SSC; intracellular structures such as the nucleus and vesicles increase side scatter[151]. FSC and SSC can be used together to discriminate between different cell types. They are also commonly used for gating a healthy cell population as a pre-processing step, and thereby excluding debris and dead cells from further analysis.

Fluorescent signals are measured simultaneously with FSC and SSC. Fluorescence occurs when a fluorophore absorbs photons from the laser, raising the electrons from the ground state to a transitional excited state. When the electrons return to the ground state, as soon as the laser illumination is quenched, the absorbed energy is released through the emission of photons of a longer wavelength[151]. Different fluorophores have distinct excitation and emission spectral profiles. Where there is little overlap

between the spectral profiles, it is possible to measure multiple fluorescent signals simultaneously. For larger overlaps, it is more complicated and requires compensation between the signals. Specific molecules within cells can be fluorescently tagged either through genomic modification or the addition of fluorophore-conjugated antibodies. This allows for rapid measurement of cellular levels of biomolecules or modifications of these.

2.3.1. Sample preparations for flow cytometry analysis

For cell cycle assays, cells fixed in 70% ethanol and stored at 4°C were washed in PBS and incubated in PI solution (PBS with 1% TritonX, 20 μg/ml RNAse A and 60 μg/ml propidium iodide) for 30 min at 37°C , placed on ice and measured.

For acetylation assays, cells fixed in 1% paraformaldehyde (PFA) were stained with Histone H4ac (pan-acetyl) antibody (Active Motif, 39244) and a secondary antibody conjugated to the Alexa 647 fluorophore (abcam, ab150067). For class switching assays, CH12F3-2A cells fixed in 1% PFA were stained with FITC Anti-mouse IgA antibody (BD Biosciences, 559354) and APC Anti-mouse IgM antibody (Affymetrix eBioscience, 17-5790-82), both 1:200 dilution. Primary B cells fixed in 1% PFA were stained with FITC Rat Anti-Mouse IgM antibody (BD Pharmingen^{TM}, 553408), 1:200 dilution. Both cell types were incubated with the antibody solutions for 45 min on ice, then washed in PBS and measured.

2.3.2. Flow cytometry measurements

Flow cytometry measurements were performed using a BD Accuri C6 Plus flow cytometer. Two excitation wavelengths, 488 nm and 640 nm, were used in conjunction with four detectors using the standard filters 533/30, 585-40, 670 LP and 675/25. The fluorophores FITC and PI were excited by the 488 nm laser, and detected by FL1 (533/30) and FL2 (585/40), respectively. The fluorophores Alexa 647 and APC were both excited by the 640 nm laser, and detected by FL4 (675/25). FITC and APC were measured simultaneously for class switching assays. The excitation and emission spectral profiles of these two fluorophores do not overlap, hence no compensation was needed.

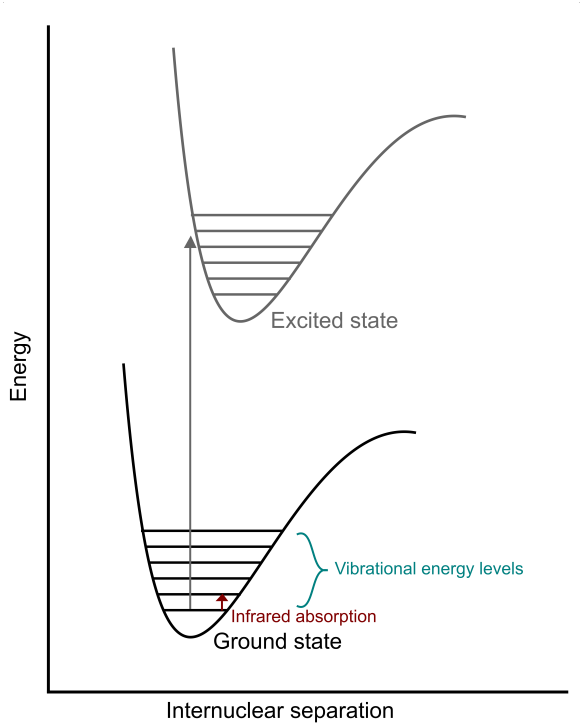

Figure 2.1.: *Molecular potential energy curve for a diatomic molecule.*
The electronic ground state and the first excited state are shown. Several vibrational states are associated with each electronic state. Absorption of infrared light causes a change in the vibrational level of the molecular normal mode.

2.3.3. Flow cytometry data analyis

The data were analysed using the software FlowJo[152]. The healthy cell population was gated based on FSC and SSC. Further gating was applied based on fluorescence signals. For cell cycle analysis, 'single cells' were gated based on the area and height of the measured propidium iodide signal. Examples of raw data and gating are in section A.1 in Appendix A.

2.4. FTIR imaging of cells

Absorption of infrared light in the mid-IR range results in vibrational excitation of molecular normal mode vibrations (Figure 2.1). It is important to note that differently from other radiations such as UV or visible light, IR radiation does not cause changes in electronic energy levels. Absorption of IR light by a molecule occurs by virtue of vibrational motion of single or multiple bonds. Vibrational bands in the FTIR

spectrum correspond to IR-active vibrational modes, i.e. those accompanied by a change in the dipole moment of the bond[153].

The dipole moment is a measure of a bond's polarity; the distribution of electrical charge between the atoms covalently bound. A separation of charge within a molecule occurs when there is an unequal sharing of electrons between atoms. This is called a dipole. The dipole moment measures the strength of a dipole; the charge multiplied by the distance between the charges. Vibrational modes that are accompanied by a change in dipole moment as the bond expands and contracts are IR-active and absorb IR light.

Different molecular bonds absorb different IR frequencies depending on their stretching or bending vibrational modes, their atomic constituents, whether the bond is single, double or triple, and the molecular environment. Molecules of biological relevance, including nucleic acids, proteins and lipids, have distinct IR active vibrational modes[154, 155], so the method is able to distinguish between these fundamental constituents of all living cells.

The measured transmittance (intensity ratio between IR light transmitted through the sample and IR light transmitted in the absence of a sample, or background intensity) is converted to an absorbance spectrum, i.e. absorbance measured as a function of wavenumber (cm^{-1}) of the radiation. The most relevant spectral regions for assaying biological materials are the fingerprint region (600 - 1800 cm^{-1}), which comprises the Amide I and Amide II bands (1500 - 1700 cm^{-1}), and a higher-wavenumber region (2500 - 3800 cm^{-1}) associated with S-H, C-H, N-H and O-H stretching[156].

Figure 2.2 shows a representative FTIR spectrum of a cell. Relevant peaks are annotated and colour-coded in the groups protein, nucleic acid and lipid. It is worth noting that an FTIR absorbance spectrum follows the Beer-Lambert law,

$$A_\lambda = \varepsilon_\lambda \cdot c \cdot l \tag{2.1}$$

meaning the absorbance, A is proportional to the molar concentration of the molecules within the sample, c through the optical path length, l and the molar absorption coefficient, ε. A more detailed list of spectral interpretations can be found in Table B.1 in Appendix B.

Micro FTIR imaging combines the use of an FTIR spectrometer with an optical microscope equipped with a focal plane array (FPA) detector, which enables the simultaneous measurement of several thousand FTIR spectra of the sample from a

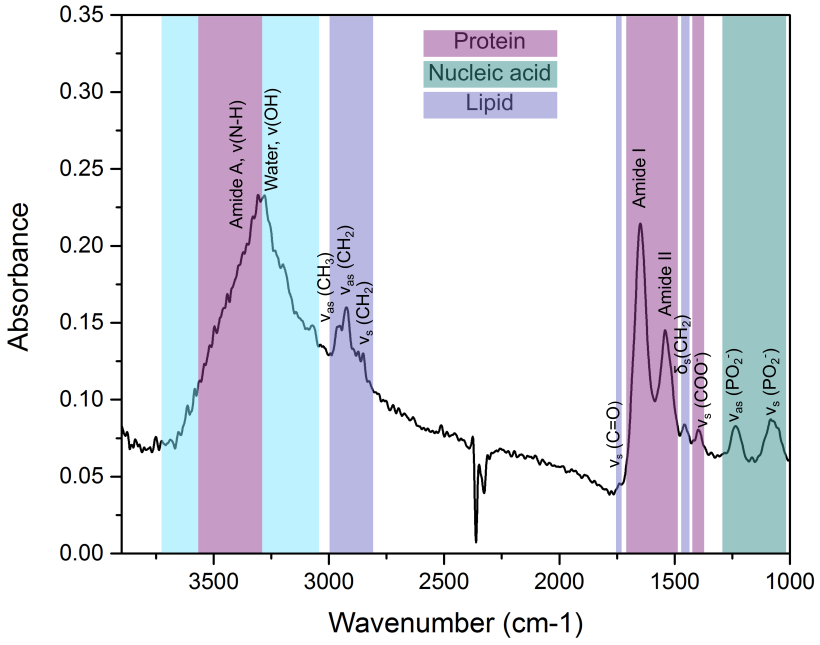

Figure 2.2.: *Representative FTIR spectrum of a cell.*
Biomolecules are annotated and colour-coded. ν=stretching vibrations, δ=bending vibrations, as=asymmetric and s=symmetric.

given location, providing both chemical and spatial information. An FTIR image is a hyperspectral dataset with two spatial dimensions and one spectral dimension. This is sometimes referred to as FTIR micro-spectroscopic imaging[157], because it combines optical microscopy, FTIR spectroscopy and imaging[156, 158]. The experimental set-up involves a mid-IR source (globar), Michelson interferometer, optical microscope, and FPA detector e.g. 128×128 pixel array. Samples are mounted on transparent microscope slides, e.g. made of calcium fluoride. The spectral datasets generated through FTIR imaging are complex. Specific biological events can be observed through changes in the spectrum and in the image. Owing to the large amount of data contained in a hyperspectral dataset, multivariate statistical analysis is often applied in order to extract the relevant information[156].

2.4.1. Sample preparation for FTIR analysis

Cells were washed in PBS, pelleted and resuspended in PBS. A 30 μl aliquot of the cell suspension was pipetted onto a calcium fluoride slide (Raman grade polished window, 20 mm diameter by 1 mm thickness, Crystran) at a 45° angle to prevent clumping. The samples were left to rest in this position while kept in the fridge at 4°C for 10 min, then fixed in 2% PFA for 20 minutes (optimisation of the fixation protocol is discussed in section 3.2). After removal of the fixative, the samples were briefly washed in water. Cells were left to dry for minimum 36 hours in a covered container. A minimum of three replicates were prepared and analysed for each cell treatment.

2.4.2. Micro-transmission Fourier Transform Infrared (FTIR) imaging

Micro-transmission FTIR images were collected using an Agilent microscope and imaging system consisting of an Agilent 670 spectrometer, an Agilent 620 FTIR microscope with a 0.62 NA, 15× Cassegrain objective, and a liquid nitrogen-cooled 128×128 focal plane array (FPA) detector with 5.5×5.5 μm^2 pixel size. The system was used in 'high magnification' mode, with magnifying optics before the FPA detector, providing an additional 5× magnification corresponding to 1.1×1.1 μm^2 pixel size. For each mosaic image, 2×2 tiles were measured with 256 scans at 4 cm^{-1} spectral resolution in the 3900-1000 cm^{-1} spectral region. A background, measured

in the absence of a sample (clean area of calcium fluoride substrate), was also measured for each sample with 512 scans. Each mosaic image had an acquisition time of approximately 50 minutes.

2.4.3. FTIR data analysis: KMC average cell spectra approach

Data analysis was conducted in the fingerprint region, between 1800-1000 cm^{-1}. Spectral information from the cells had to be extracted from the whole FTIR images, to enable a reliable comparison between cell treatments. The data were analysed in R using the software packages hyperSpec[159], FTIR, gridExtra[160] and matrixStats[161].

K-means cluster analysis with two clusters was performed on each image to enable the extraction of a mean cell spectrum to be compared between samples and treatments.

2.4.4. FTIR data analysis: Cell segmentation approach

To further enable the extraction of single cell spectra from each FTIR image, an image-based cell segmentation approach was applied. The image-based cell segmentation was conducted in Python using Otsu thresholding and watershed segmentation. The spectral signatures of the samples were then compared at the single cell level, thus considering intra-sample variability and quantifying the spectral differences between cell populations.

Pre-processing of the spectra involved baseline subtraction using an offset at 1800 cm^{-1}, and normalisation to the Amide I peak maximum in the range 1710-1650 cm^{-1}. To calculate peak intensity ratios, a baseline passing through the troughs each side of the peak was drawn and the integral of the peak was calculated.

2.5. Live cell Raman mapping

Vibrational spectroscopy also includes Raman spectroscopy. Similarly to FTIR, it measures the interaction between light travelling through a sample and the molecular vibrations in the sample itself. Unlike FTIR, Raman spectroscopy is based on a light scattering effect.

Elastic scattering, known as Rayleigh scattering, does not result in energy loss or gain. Rayleigh scattering is most likely event. Raman scattering on the other hand is inelastic. It results in a gain or loss of energy for the light photon, referred to as Anti-Stokes and Stokes Raman scattering, respectively (Figure 2.3). The loss or gain of energy for the scattered photons results in a longer or shorter wavelength. It is this shift that is measured in Raman spectroscopy[162].

FTIR and Raman spectroscopy give similar, yet complementary results in that they both detect vibrational modes in molecules, but the physical principle (selection rules derived by quantum mechanics) are different - a vibrational mode is Raman active if it causes a change in the polarizability of the molecule.

The polarizability of a molecule is a measure of how easily the charge distribution can be distorted from its normal shape in response to an external field. A change in bond length, bond strength and electron density can affect the polarizability of a molecule. Molecules with a delocalised electron charge, for example molecules with conjugated double (or triple) bonds such as benzene, have a high polarizability. Longer bond lengths increase polarizability, and increasing bond strenth decreases polarizability. Vibrational modes with a net increase of bond length, such as symmetrical stretching, are Raman active.

Raman and FTIR spectroscopy are said to be complementary techniques, because for molecules with a centre of symmetry, an IR active bond is not Raman active, and vice versa. Additionally, for other molecules, vibrational modes that are strong IR absorbers tend to be weak Raman scatterers. One such example is water. The three fundamental vibrational modes of water, symmetric and asymmetric stretching and bending mode, all result in a change in dipole moment and thus are all IR active. Due to the large change in dipole moment, in particular for the stretching modes, strong vibrational bands are seen in the IR absorption spectrum. On the contrary, water is a small, essentially isotropic molecule and has a modest polarizability, making it a very weak Raman scatterer. The three vibrational modes are Raman active, but the low polarizability means the interference of water in the Raman spectrum of biomolecules is minimal.

2.5.1. Sample preparation

Cells were washed in PBS, pelleted and resuspended in PBS or Phenol Red free medium (HyClone^{TM} RPMI 1640 media without Phenol Red (GE Healthcare Life Sci-

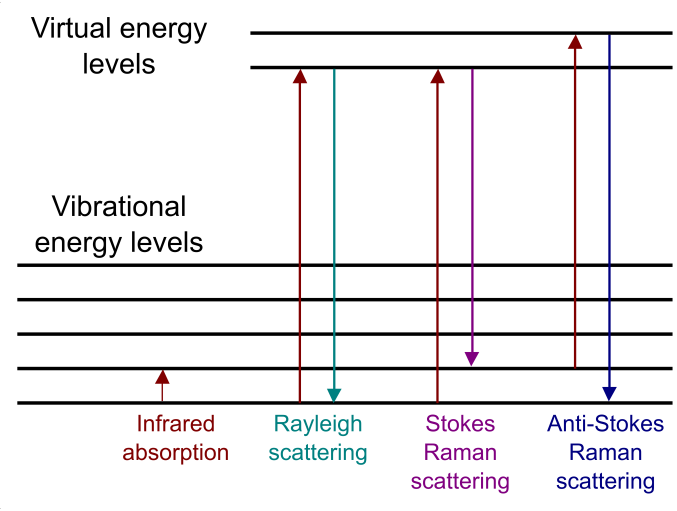

Figure 2.3.: *Vibrational spectroscopy: FTIR and Raman.*
Raman scattering is an inelastic scattering effect, meaning the light gains (Anti-Stokes) or loses energy (Stokes) during the scattering process.

ences, SH30605.01) with 10% Fetal Bovine Serum, 1% Pen-Strep, 1% Glutamine, 1% Sodium Pyruvate and 50 μM β-mercaptoethanol). PBS or Phenol Red free medium was manually flowed into the PDMS chip bonded to a glass coverslip through Portex tubing PE 0.86×0.33mm BxW (Scientific Laboratory Supplies, TUB26668) using a syringe and a 21G microlance (Becton Dickinson Medical, 304432). Cells were flowed into the chip through Portex tubing using a syringe and a 21G microlance and left to settle for minimum 30 minutes.

2.5.2. Raman measurements

Raman maps were collected using a WITec alpha300 R Confocal Raman system consisting of a 532nm laser, a fibre-coupled UHTS spectrometer, and an confocal microscope with a 0.7 NA, 50× objective. The combination of Raman spectroscopy with a confocal microscope allows for optical sectioning. This is achieved by the pinhole, which spatially filters the sampling volume, so that only Raman scatter from the focal plane is detected. The microfluidic chip containing the single cells in suspension was held coverslip side facing up in a custom holder. Single cells (adhering to the glass) were identified in white light imaging mode, then the focus was adjusted in Raman mode using the oscilloscope to maximise the scattered signal intensity (of the C-H stretching peak in the range 2700-3000 cm^{-1}), and cell maps were collected with 5 measurement points per micrometre using a 0.1 s integration time. Single position spectra were collected with 20 accumulations using a 0.5 s integration time

per point. Cells were kept in the microfluidic chip for a maximum of four hours during measurements, before a new chip with fresh cells was prepared.

2.5.3. Data analysis

Data processing was performed using MATLAB 2020a. Common k-means cluster analysis with 10 clusters was performed on 118 cell maps (58×D0, 60×D4). This involved the calculation of a similarity measure for each of the spectra from all 118 maps (a total of 716,250 spectra). As the most similar spectra are grouped together, the spectrum of the new group becomes the mean of its members. At the end of the process, when ten similar group clusters remained, they contained the spectra from regions of cells with similar biochemical constituents, each represented by a mean spectrum or centroid. Each of the 10 clusters was assigned as nucleus, cytoplasm or background, based on the spectral profiles of the cluster centroids. Hence, a mean nucleus, cytoplasm, whole cell (cytoplasm + nucleus) and background spectrum was extracted from each cell map. 13 maps (5×D0, 8×D4) were discarded from the dataset before further analysis, since they either contained no pixels identified as nucleus or cytoplasm, or very few pixels associated with nucleus - with a nucleus size of less than 3 μm.

To remove background signal (from the coverslip and PBS), the background spectra were subtracted from the nucleus and cytoplasm spectra for each map in three steps. (1) The spectra were baseline-corrected by subtracting an offset (based on the mean intensity in the range 1780-1840 cm^{-1}). (2) The background spectra were smoothed using a Savitzky-Golay filter (order = 2, framelength = 99) to reduce the effect of noise. (3) The smoothed background spectra were then subtracted from the nucleus, cytoplasm and whole cell spectra.

Principal Component Analysis (PCA) was performed on nucleus, cytoplasm, and whole cell spectra. For each principal component, a t-test was used to determine if scores were significantly different between D0 and D4 cells . Linear Discriminant Analysis (LDA) was also performed to single out the peaks responsible for the discrimination between D0 and D4 cells.

2.5.4. Partial least squares regression

Transcriptomic data were collected by Ho Wai Kevin Yim as described in section 2.6. To analyse the potential correlation between the Raman data and the transcriptomic data, Partial Least Squares (PLS) regression was applied to the datasets. The transcriptomic data consisted of the read counts for 17,725 transcripts with three D0 samples (D0-1, D0-2, and D0-3) and three D4 samples (D4-1, D4-2, and D4-3). Dimension-reduced Raman data were used in the form of PC scores. To correspond to the three replicates for each condition of the transcriptomic data, the Raman cell measurements were randomly assigned to three groups of D0 and three groups of D4.

PLS regression analysis was performed with a leave-one-out approach; each of the six samples, i, was removed in turn. Each leave-one-out analysis determined a linear regression model between the Raman (R_{-i}) and transcriptomic (T_{-i}) datasets - meaning the PLS regression coefficients matrix, $BETA_{-i}$, was found so that

$$R_{-i} = BETA_{-i} \cdot T_{-i} \tag{2.2}$$

For each PLS regression analysis, Raman PC scores were predicted for the left-out sample, i, using the transcriptomic data (T_i) and the $BETA_{-i}$ matrix.

To assess the validity of the predicted Raman PC scores (and thus the regression model), they were compared against the single cell PCA scores. For further assessment, the predicted Raman PC scores were then converted to LDA scores and again compared with the single cell data.

2.6. Transcriptomic data

RNA extraction and transcriptomic data analysis were performed by Kevin Yim for the manuscript [2].

2.6.1. RNA extraction

Total cell RNA was extracted by TRIzol followed with chloroform for phase separation and 100% isopropanol for RNA precipitation. Total RNA was eluted in 30 μl RNase-free water after being washed twice in 75% ethanol. The RNA concentration was

assessed using a NanoDrop 2000 spectrophotometer (Thermo Scientific). The RNA yield and size distribution were analysed using an Agilent 2200 Tapestation with RNA Screentape (Agilent Technologies).

2.6.2. RNA-seq library preparation, next-generation sequencing and data processing

For small RNA library preparation, RNA aliquots were used for library preparation using NEBNext Multiplex Small RNA library preparation kit (New England Biolabs). The PCR amplified cDNA construct (from 140-160 basepairs) was purified using a QIAquick PCR Purification kit (Quiagen). The purified cDNA was directly sequences using an Illumina MiSeq 2000 platform (Illumina). For long RNA library preparation, libraries were constructed using Ribo-Zero Magnetic Gold Kit (Human, Illumina) and NEBNext Ultra^{TM} RNA Library Prep kit for Illumina (New England Biolabs) according to the manufacturer's instructions. Libraries were tested for quality and quantified using qPCR (Kapa Biosystems). The resulting libraries were sequenced on a HiSeq 2500 instrument that generated paried-end reads of 100 nucleotides.

Raw sequencing reads were checked for potential sequencing issues and contaminants using FastQC. Adapter sequences, primers, number of fuzzy bases (Ns), and reads with quality scores below 30 were trimmed. Reads with a length of less than 20 bp after trimming were discarded. Clean reads were aligned to the mouse genome (GRCm38) using the TopHat 2.0 program, and the resulting alignment files were reconstructed with Cufflinks[163]. The transcriptome of each sample was assembled separately using Cufflinks 2.0 program.

2.6.3. Sequencing data analyses and statistical methods

Read counts of each sample were subjected to cluster analysis[164] and differential expression analysis using RNA-seq 2G[165]. Genes with |fold change| $\geq$1, P value $\leq$0.05 and false discovery rate (FDR) $\leq$0.05 were considered statistically significant. Expression of significant differentially expressed genes in different B cell subsets was determined using My Geneset ImmGen[166].

2.7. Nuclear properties assessed using microfluidic devices

Mechanical properties of cell nuclei can be determined using deformability cytometry (introduced in section 1.4) and fluorescence imaging. Here, the mechanical property auxeticity and its correlation to chromatin decondensation was examined in B cells. Auxeticity is defined as the property of a material or structure having a negative Poisson's ratio. The Poisson's ratio, ν, quantifies the deformation of a material perpendicular to applied strain, and is defined as the negative ratio of transverse strain, S_T, over axial strain, S_A:

$$\nu = -\frac{S_T}{S_A} \tag{2.3}$$

The majority of materials become thinner if they are stretched - they have a positive Poisson's ratio. Auxetic materials instead expand in the perpendicular direction to stretching, meaning they have positive S_T. To examine this effect in B cell nuclei, a chip was designed to apply stretching forces to the nucleus (more details in section 4.2).

2.7.1. Sample preparation and microfluidic experimental setup

The chip was functionalised with 1 mg/ml BSA and incubated at 37°C for one hour. Cells were spun down (300gx5min) and resuspended in 0.5 μg/ml Hoechst 33342 (ThermoFisher Scientific, H3570) for CH12F3-2A cells and 5 μg/ml Hoechst 33342 for primary B cells. Following incubation at 37°C for 20 minutes, the cells were spun down again, washed in PBS and resuspended in PBS, 50 μM β-mercaptoethanol, 15% OptiPrep (Sigma Aldrich, D1556-250ML) for CH12F3-2A cells and PBS, 50 μM β-mercaptoethanol, 10% OptiPrep for primary B cells. The β-mercaptoethanol and OptiPrep were added to reduce cell propensity for sticking to each other and to the chip, in particular the channel entrances.

Cells were flowed into the microfluidic chip at a constant applied pressure of 1 mbar through Portex tubing PE 0.86x0.33mm BxW using a Fluigent pump. This resulted in a cell average velocity of 0.55 $\pm$ 0.06 mm/s that was constant during channel translocation. The microfluidic chip was mounted on an inverted epifluorescence microscope (Olympus IX73) equipped with a 40×, 0.95 NA objective and a sCMOS camera (Andor Zyla 4.2) used at a frame rate of 30 fps. A minimum of three replicates were prepared and analysed for each cell treatment.

2.7.2. Nucleus deformation data analysis

Image analysis of nucleus deformation was performed using Python, in particular the modules scikit-image[167], imageio, numpy[168] and SciPy[169]. Cell nuclei were identified using li thresholding (optimisation of thresholding discussed in subsection 4.3.1) and tracked between frames. Fragmented trajectories were stitched together manually. Properties, including minimum axis (a) and maximum axis (b), were saved for each nuclei in each frame. These were used to calculate average nuclei size within region 0 (before channels) and region 1 (within channels), as well as transverse strain, S_T

$$S_T = (a_{\text{in channel}} - a_{\text{before channel}})/a_{\text{before channel}} \tag{2.4}$$

and axial strain, S_A

$$S_A = (b_{\text{in channel}} - b_{\text{before channel}})/b_{\text{before channel}} \tag{2.5}$$

for each cell. These calculations are also described in Figure 4.5c-d in section 4.4.

3. Single cell FTIR imaging of DNA and chromatin changes

The paper "Single Cell Imaging of Nuclear Architecture Changes"[1] forms the basis of the following chapter.

3.1. Background

Chromatin conformation changes are important drivers of cell development, and thus measurements of pan-nuclear dynamics may enable phenotypic characterisation of cells. Pan-nuclear measurements can be achieved in many ways. Measurements of chromatin architecture have generally required bespoke protein, DNA, or RNA labels[170–173] or high-throughput DNA sequencing such as chromosome conformation capture (or 3C) and its more recent variant Hi-C, among others[174]. However, these specific tools are not without their own limitations in terms of prohibitive cost, technical difficulties, and reproducibility issues.

One emerging field that may provide new tools for chromatin research is vibrational spectroscopy-based chemical imaging. Fourier Transform Infrared (FTIR) spectroscopy, which enables label-free detection of the chemical composition and heterogeneity of a sample, has been shown to be a powerful tool for analysing biological samples[156]. The technique probes vibrational modes in molecules that are specific as a chemical fingerprint; through imaging or mapping approaches with a microscope, it provides molecular distributions with high spatial resolution. FTIR spectroscopy has previously been used to monitor DNA conformational changes[175, 176], making it a powerful biochemical tool for studying chromatin structure and conformation. Developing novel approaches to assessing chromatin changes at the single cell level would enable a more comprehensive understanding of the nuclear response.

In this chapter, the use of FTIR imaging for the meaurement and quantification of changes to DNA levels and chromatin conformation in single B cells will be explored (Figure 3.1).

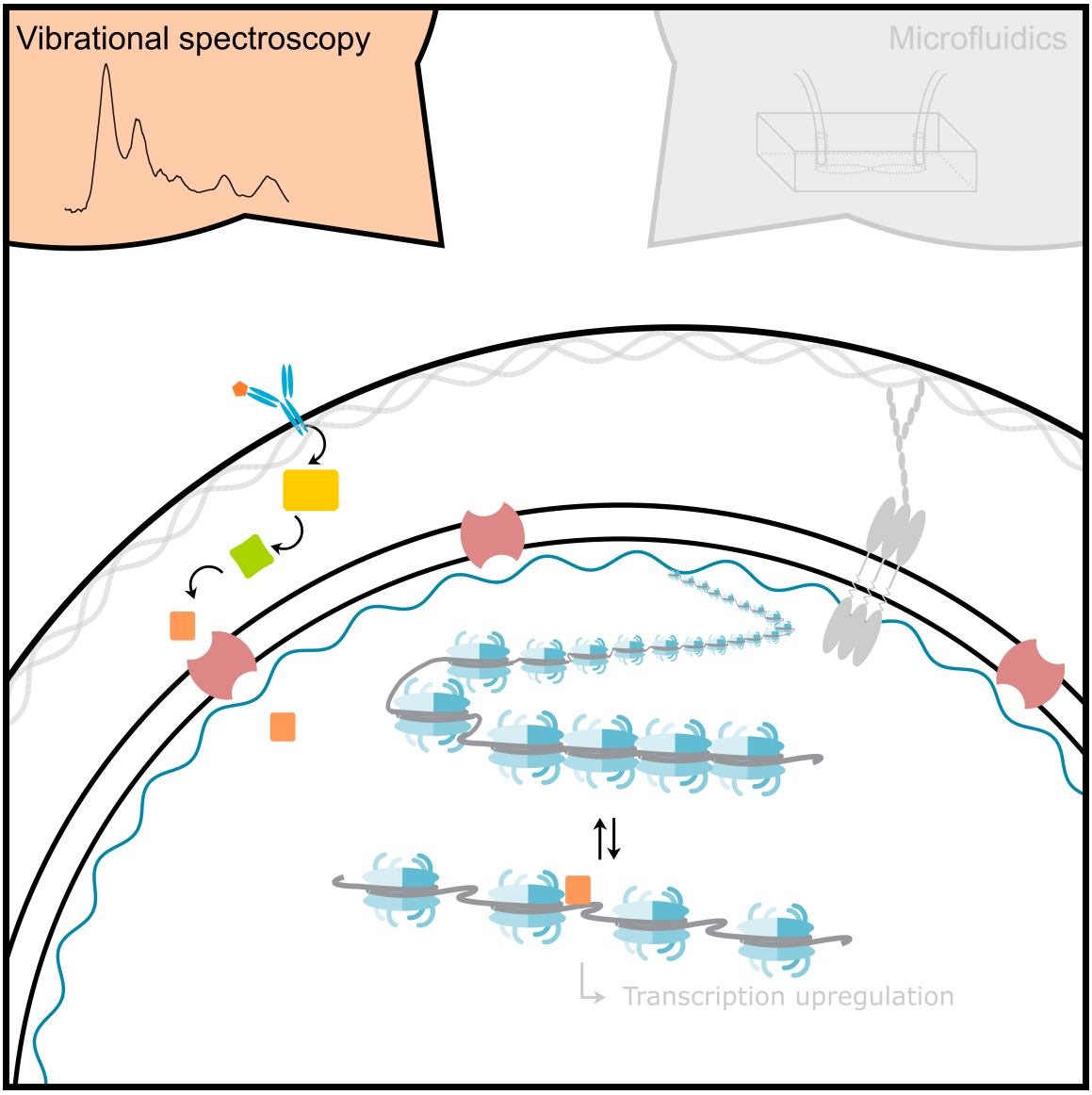

Figure 3.1.: *Thesis graphical summary - Chapter 3 focus.*
This chapter focuses on detecting chromatin decondensation in single cells using the label-free technique FTIR imaging.

3.2. Fixation of cells for FTIR imaging

To optimise sample preparation protocols, two fixation methods were compared: 2% paraformaldehyde (PFA) fixation and 70% ethanol fixation. PFA, and other aldehydes, works by cross-linking biomolecules of the cells, whilst alcohol-based fixation works by denaturing proteins through the disruption of hydrophobic bonds[119].

For an even distribution of suspension cells on calcium fluoride slides to allow for imaging of single cells, the preparation methods described in subsection 2.4.1 was used. Figure 3.2 shows the comparison between cells fixed in 2% PFA (Figure 3.2a-c) and cells fixed in 70% ethanol (Figure 3.2d-f). For both cell treatments, a white light image (Figure 3.2a and d), a pseudo-colour FTIR image based on the integrated intensity of the Amide I peak (Amide C=O stretching), 1680-1620 cm^{-1}(Figure 3.2b and e), and a representative spectrum extracted from the centre of a cell (Figure 3.2c and f) are shown.

For both cell preparations, the signal measured from single cells is strong enough to distinguish them from the substrate, hence revealing the suitability of FTIR imaging towards detection of single fixed cells. However, the interface between cells and substrate appears sharper for the PFA fixed cells. Furthermore, based on the white light images, ethanol fixation appears to shrink the cells more so than PFA. This is in turn expressed in the individual spectrum in the form of scattering (Figure 3.2f). Based on these data, PFA was determined to be the preferred fixative when preparing CH12 cells for FTIR imaging. For the following experiments, all cells were fixed in 2% PFA.

3.3. Novel optimisation of micro-FTIR imaging for single cell analysis

Previous work has shown FTIR imaging of biological samples[177–179], however efficiently extracting average single cell spectra from large FTIR images has remained problematic. Smaller FTIR images of single cells, or selection of areas of interest within larger images post-acquisition, while able to circumvent this, are time consuming approaches. This was addressed using a combination of experimental and computational optimisations. The photomicrograph of an untreated CH12F3 cell

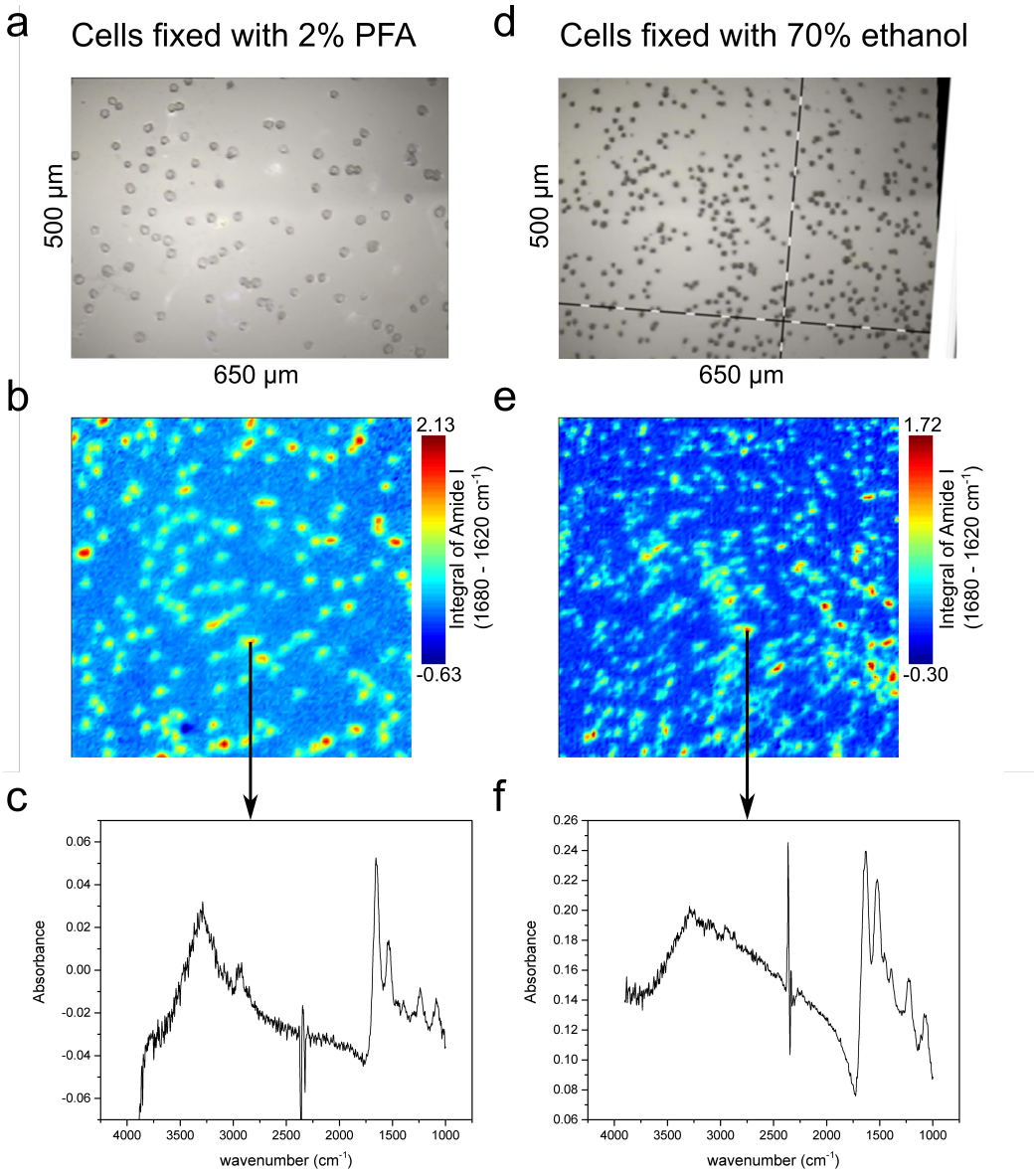

Figure 3.2.: *Comparison of FTIR imaging of cells fixed with PFA and ethanol.* ***(a-c)*** *PFA fixed cells.* ***(d-f)*** *Ethanol fixed cells.* ***(a and d)*** *White-light images.* ***(b and e)*** *A pseudo-colour FTIR image based on the integral of Amide I.* ***(c and f)*** *A representative spectrum from the centre of a cell - position indicated by an arrow.*

sample acquired using a 15× Cassegrain objective is shown in Figure 3.3a. Cells appear as dark ovoids fairly homogeneously distributed on the transparent microscope slide. A chemical image based on the intensity (peak maximum) of the Amide I band, essentially C=O stretching of the peptide group, in the range 1675-1625 cm^{-1} is presented in Figure 3.3b. Note that FTIR images are pseudo-colour images where the high absorbance, represented by red colour, corresponds to high concentration of particular chemical species, in this case proteins, whilst low absorbance represented by blue colour corresponds to low concentration or absence of that species. Here, cells are identified by the high protein signal (Amide I) corresponding to red-to-green areas in Figure 3.3b.

3.3.1. K-means cluster analysis

K-means cluster analysis with two clusters provided an initial separation of cells from substrate (Figure 3.3c), so that an average spectrum from all cells was extracted (Figure 3.3e). As a multivariate approach, k-means cluster analysis categorises the pixels of the image based on the similarity between spectra. This enabled comparison of cell spectra between samples, but did not allow single cell analysis. Therefore an additional analysis approach was explored.

3.3.2. Cell segmentation

Image segmentation analysis provided separation of small clusters of cells into single cells (Figure 3.3d), so that an average spectrum per single cell was extracted (Figure 3.3f). This enabled downstream analysis of the spectral signatures of differentially treated cell populations at the single cell level. Spectral analysis was performed in the "fingerprint" region (1800-1000 cm^{-1}), which contains characteristic signals from protein, lipids, and nucleic acids.

3.3.3. Comparison

A comparison between the k-means extracted cell spectrum and the average spectrum from the cell segmentation approach is shown in Figure 3.3g. This compares the two methods' estimated average cell spectrum from the FTIR image. The two spectra are nearly identical. This verifies the validity of the cell segmentation approach for extracting spectral information from single cells.

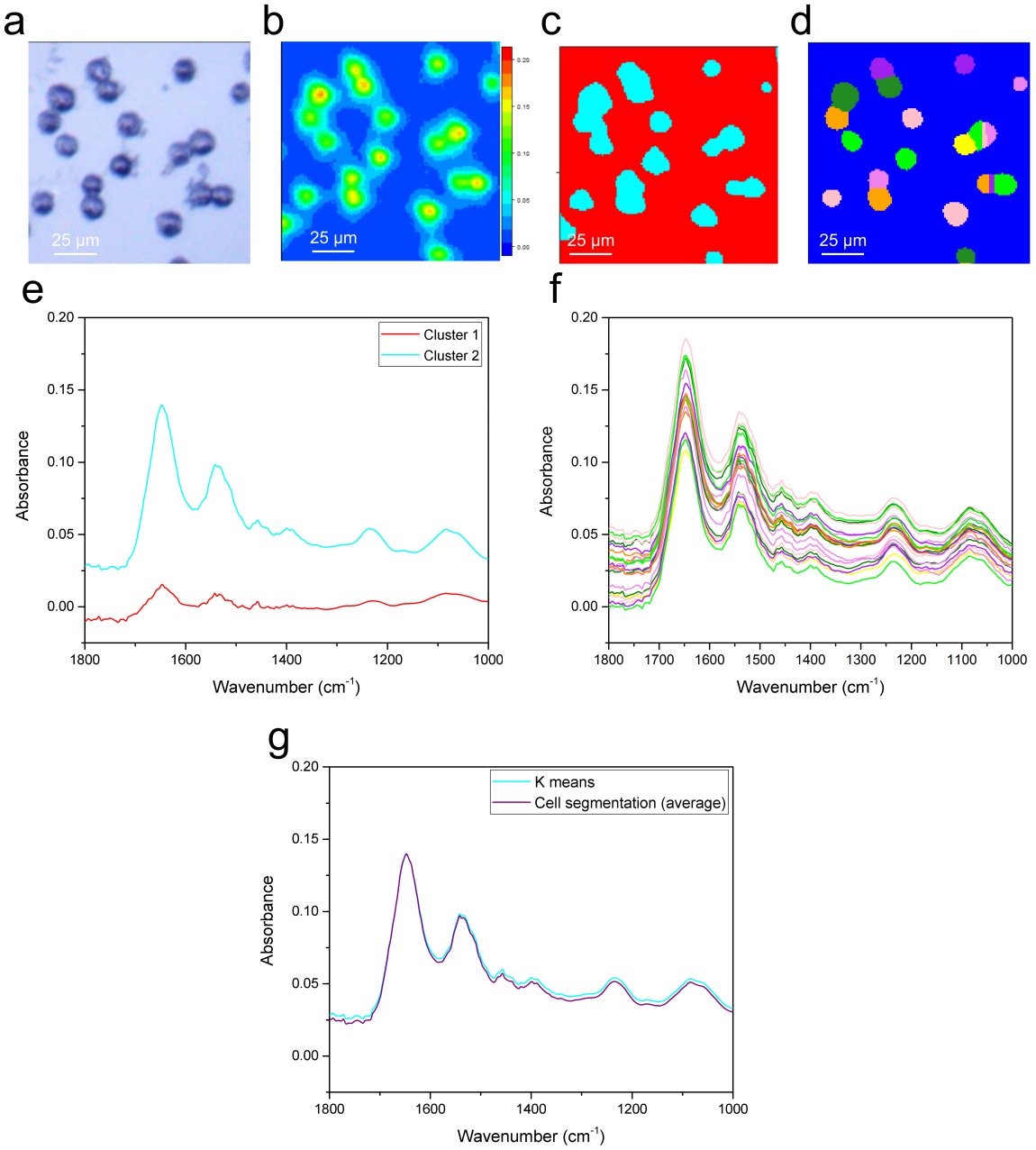

Figure 3.3.: *Data analysis approaches.*
(a) *White-light image measured in reflection mode.* ***(b)*** *Chemical image based on 1625-1675 cm^{-1}.* ***(c)*** *K-means clustering output with two clusters.* ***(d)*** *Output of the cell segmentation of the data in (b).* ***(e)*** *Extracted cluster spectra; cluster 1 (red) represents the substrate, and cluster 2 (turquoise) represents the cells.* ***(f)*** *Extracted single cell spectra. The spectra are colour coded to (d)* ***(g)*** *Comparison of the k-means cell spectrum and the average spectrum from the single cell segmentation approach.*

3.4. DNA quantity measurements using FTIR imaging during cell cycle progression

Peak absorbance in the FTIR spectrum is related to the concentration of a particular chemical species (Beer-Lambert law; Equation 2.1 in section 2.4). The application of micro-FTIR imaging to detect changes in intracellular DNA content was validated by investigating the effect of cell cycle progression on the molecular properties derived from FTIR spectroscopy. The cell cycle is the process used by cells to couple DNA duplication (S phase) with cell division (M phase). These two phases are interjected by two growth phases known as G1 and G2 phase, respectively (Figure 3.4A). FTIR images of cell populations stalled in early S phase (1×DNA content) and G2/M phase (2×DNA content) were therefore compared with untreated control samples.

Hydroxyurea and Nocodazole are two distinct drugs utilised to arrest cells at specific phases of the cell cycle. Treatment with Hydroxyurea stalls cells in early S-phase, through inhibition of DNA synthesis. Treatment with Nocodazole stalls cells at the G2/M transition phase through the disruption of microtubules and mitotic spindle function. The effect of each drug on CH12F3-2A cells was assessed by PI staining and flow cytometry (Figure 3.4B). An increase in PI signal correlates with an increase in DNA content[180]. The control cells are distributed across the different cell cycle phases, starting from an initial peak representing cells in G1 phase (1×DNA content), spanning the increase in DNA content during S phase (>1×DNA content), and ending in a peak for cells in G2/M phase (2×DNA content). Cells treated with Hydroxyurea are stalled in early S phase, which is denoted by a large main peak at low PI signal. In contrast, cells treated with Nocodazole give rise to a single peak at high PI signal, indicating stalling in G2/M phase.

Figure 3.4C shows FTIR images of representative samples for each cell group. Average FTIR spectra calculated from single cell spectra within each group show differences (Figure 3.4D), especially in the phosphate symmetric stretching (ν_s PO_2^-) peak at 1070-1035 cm^{-1}, which is due to intracellular DNA. Changes in DNA to protein ratio at the single cell level was quantified using the integrated ratio of ν_s PO_2^- to Amide II peak at 1580-1490 cm^{-1} (Figure 3.4E), as opposed to the Amide I, which may contain some contribution from the water bending mode. The DNA-to-protein ratios were significantly different between control, S and G2/M phase cell populations. The observed differences reflected changes in DNA content, with lower values for the S

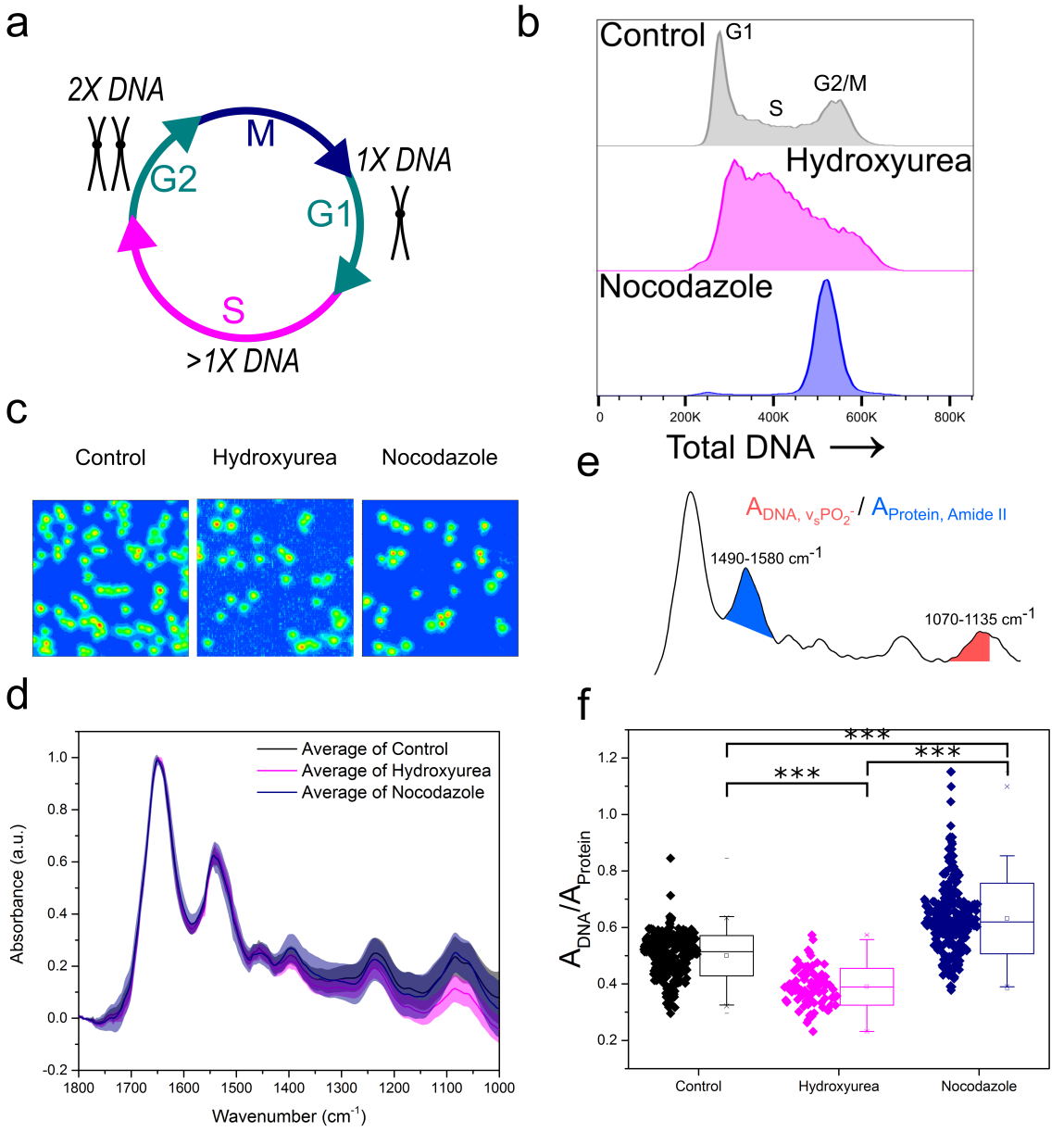

Figure 3.4.: *Key FTIR spectral signatures associated with intracellular DNA levels. Reproduced from [1].* ***(a)*** *Schematic of the cell cycle. Cells go from G1 phase with 1×DNA, through S phase where the DNA is replicated, to G2 phase with 2×DNA. Following this the cells enter M phase where they undergo mitosis and divide into two daughter cells.* ***(b)*** *Flow cytometry assessment of intracellular DNA content of cell samples: Control, Hydroxyurea treated and Nocodazole treated. DNA is stained by the fluorescent marker PI.* ***(c)*** *FTIR images of cell samples Control, Hydroxyurea treated and Nocodazole treated.* ***(d)*** *Average single cell spectrum for each cell treatment. Shaded area denotes the standard deviation.* ***(e)*** *Representative spectrum indicating the peak ratios used for single cell analysis in (f).* ***(f)*** *DNA-to-Protein peak ratio showing the spectral changes associated with differing levels of intracellular DNA at a single cell level. A t-test gave a statistically significant difference between samples (ns.: $P>0.05$, $*:\leq 0.05, **: P \leq 0.01, ***: P \leq 0.001$).*

phase stalled cells (Hydroxyurea treatement, pink) compared to control cells, and higher values for the G2/M phase stalled cells (Nocodazole treatment, navy).

The correlation between DNA-to-protein ratio and the intracellular DNA content is unsurprising, as a change in concentration leads to a change in absorbance. The FTIR spectral changes are potentially caused by more than a simple decrease or increase in intracellular DNA. Significant changes to DNA environment and structure, which are especially apparent for chromosome condensation during G2/M phase, likely also influence the absorbance, as this would incur changes to local densities and the extinction coefficient. This brings up the question whether FTIR imaging can detect changes in DNA strcuture and environment, when these are independent from cell cycle phase and thus intracellular DNA content.

3.5. DNA quality measurements using FTIR imaging of chromatin changes

DNA rarely exists in isolation within the cell nucleus. Indeed, the macromolecular complex known as chromatin consists primarily of genomic DNA wound around a complex of histone proteins (Figure 3.5A). Although DNA quantity does not vary during the G1 and G2 growth phases of the cell, the chromatin fibres do still respond to intra- and extra-cellular stimulations which can alter the quality and architecture of the chromatin complex.

3.5.1. FTIR spectral changes in response to chromatin changes

TSA is an inhibitor of histone deacetylases which primarily function as transcriptional repressors. Treating CH12F3-2A cells with TSA causes hyperacetylation of the histones which results in chromatin decondensation. This increase in acetylation was verified by flow cytometry, using an antibody against pan-acetylation (Figure 3.5B). Chromatin decondensation is an essential intermediate in a number of cell processes, including immune activation of B cells, where it facilitates the increased transcription associated with activated B cells[181, 182]. TSA treatment of cells can therefore mimic the chromatin modifications observed during immune cell activation. Indeed, lymphocyte stimulation has previously been shown to induce an increase in acetylation of the chromatin[66, 183, 184]. In addition, secondary antibody diversification, a result of activation of B cells via antigen binding, can be initiated in CH12F3-2A

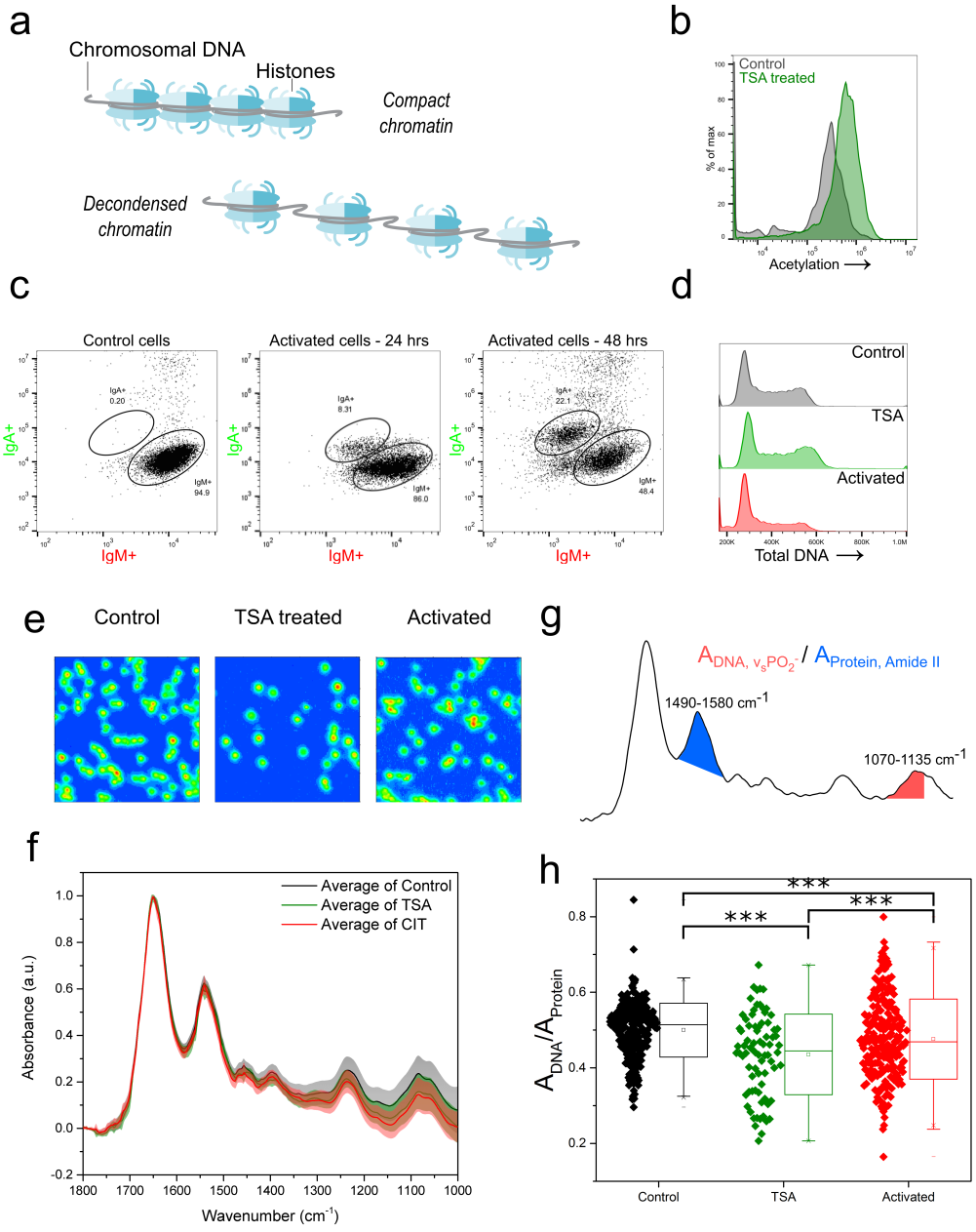

Figure 3.5.: *Chromatin changes can be assessed using FTIR imaging. Reproduced from [1].* ***(a)*** *Cartoon representation of chromatin, in compact and decondensed state.* ***(b)*** *Verification of the effect of TSA treatment, as seen by increased acetylation levels in TSA treated cells compared to control cells. Intracellular acetylation level labelled by an anti-pan acetyl antibody and measured by flow cytometry.* ***(c)*** *CSR measured as verification of immune activation of B cells through CIT treatment. A subpopulation, increasing over 48 hours, switches from IgM to IgA expression.* ***(d)*** *Cell cycle phase distribution for TSA treated and activated cells compared to control cells. DNA is stained by the fluorescent marker PI.* ***(e)*** *FTIR images of cell samples: Control, TSA treated and Activated (CIT treated).* ***(f)*** *Average single cell spectrum for each cell treatment. Standard deviaton is marked as a shaded area.* ***(g)*** *Representative spectrum indicating the peak ratios used for the single cell analysis in (h).* ***(h)*** *DNA-to-protein peak ratio showing the spectral changes associated with changes to chromatin state at the single cells level. A t-test gave a statistically significant difference between samples (ns.: $P>0.05$, $*: P \leq 0.05, **: P \leq 0.01, ***: P \leq 0.001$).*

cells through addition of a cytokine cocktail (CIT) consisting of IL-4, TGF-β and anti-CD40. The resultant class switch recombination, where a subset of the cells undergoes DNA recombination leading to changes to the expressed antibody constant region, was assessed using flow cytometry and antibodies against the Ig isotypes IgM and IgA (Figure 3.5C).

The effect of chromatin decondensation induced through TSA treatment or CIT mediated immune activation, was investigated here. Cell cycle phase distribution was assessed as before by flow cytometry. Importantly, neither TSA or CIT treatment resulted in changes to overall DNA content (Figure 3.5D). No statistically significant difference was found for the cell cycle phase distribution between the treatments (Control: G1 = 45.1±5.4, S = 29.1±2.3, G2/M2 = 25.2±6.8, TSA treated: G1 = 55.5±12.8, S = 20.8±5.1, G2/M = 22.8±7.9, CIT treated: G1 = 48.2±7.7, S = 22.1±3.1, G2/M = 22.8±9.4). Therefore, any differences observed in FTIR spectra would derive from "qualitative" chemical and conformational changes to the chromatin, rather than from changes to overall DNA "quantity".

FTIR images and spectral analysis for this study are presented in Figure 3.5E-G. FTIR spectra from TSA and CIT treated cells were found to vary with respect to those of control cells (Figure 3.5F), especially in the phosphate stretching peaks. The single cell DNA-to-protein ratio showed a statistically significant decrease for both TSA and CIT treated cells when compared to control cells (Figure 3.5G). Although a significant difference was found between TSA and CIT treated cells, the similar response relative to control cells is consistent with the similar chromatin response expected for the two treatments. Furthermore, it supports the consensus that, while only a subset of the cells successfully switches IgM to IgA, all cells are initially activated by the addition of CIT.

3.5.2. Second derivative analysis of FTIR spectra

The second derivative of the average single cell FTIR spectrum of all samples was calculated to investigate changes in Amide I sub-peak positions between cell treatments. Only minor changes were observed, suggesting that protein secondary structure[176, 185] is essentially preserved. This rules out major conformational changes to the protein component of chromatin and the cell overall.

Figure 3.6 shows the second derivative for the Control, TSA treated, and CIT treated cells, the latter showing the largest, although still minor, variation amongst the cell

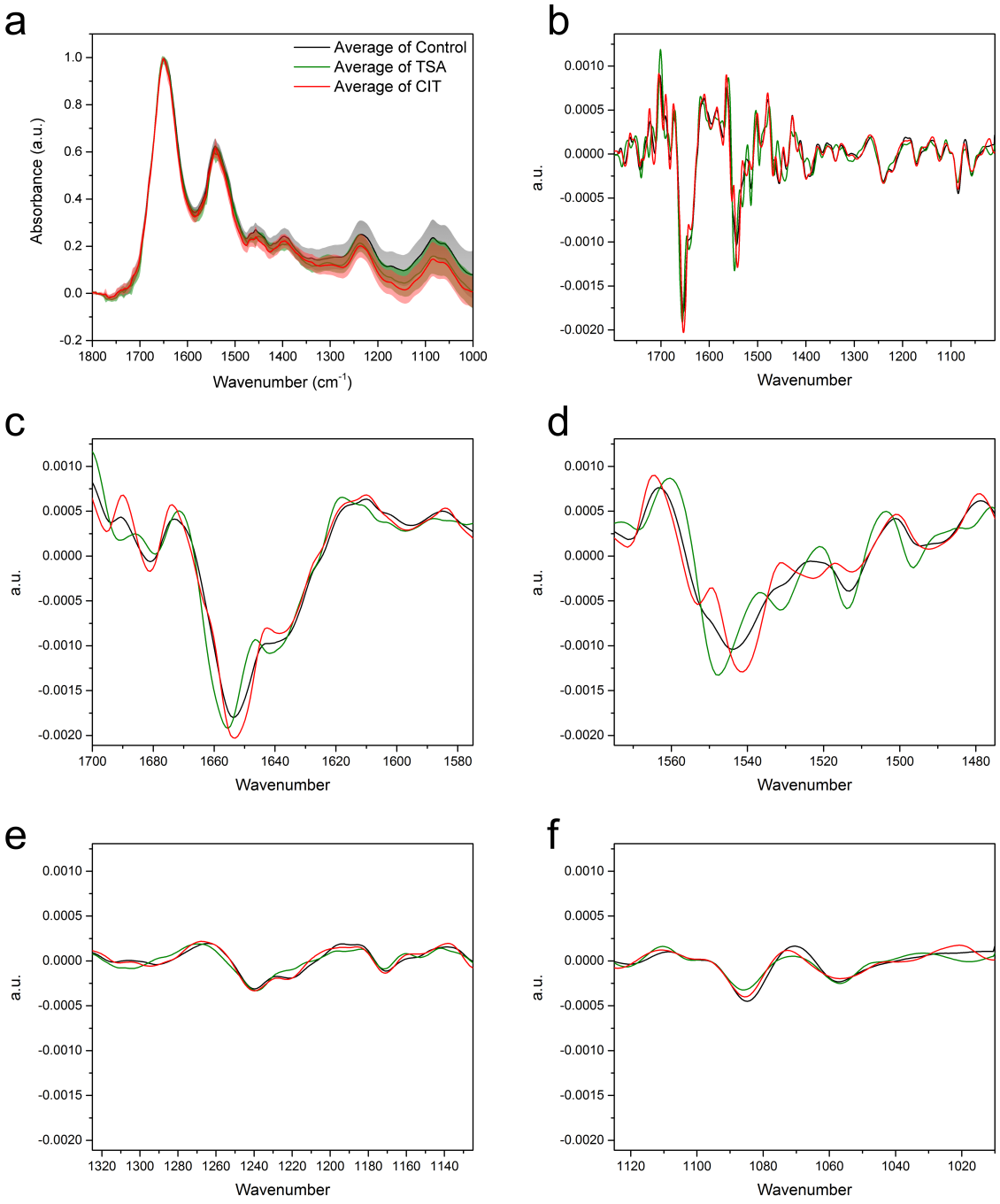

Figure 3.6.: *Second derivative spectra of cells subjected to different treatments. Reproduced from [1].* ***(a)*** *Average FTIR spectra and standard deviation for the three cell treatments; Control, TSA treated, and CIT treated (activated) as seen in Figure 3.5.* ***(b)*** *Second derivative of the average FTIR spectra seen in (a), calculated with 25-point quadratic Savitzky-Golay filter.* ***(c)*** *Amide I region: peptide C=O stretching.* ***(d)*** *Amide II region: primarily, NH bending.* ***(e)*** *Phosphate asymmetric stretching region: $\nu_{as}(PO_2^-)$.* ***(f)*** *Phosphate symmetric stretching region: $\nu_s(PO_2^-)$.*

Control		TSA treated		Activated (CIT treated)	
α 1653.7 cm^{-1}	β 1640.2 cm^{-1}	α 1655.3 cm^{-1}	β 1641.8 cm^{-1}	α 1652.9 cm^{-1}	β 1638.6 cm^{-1}
-0.0018	-0.00097	-0.00192	-0.00086	-0.00202	-0.00086
β / α		β / α		β / α	
0.54		0.45		0.43	

Table 3.1.: *Ratio of β-sheet to α-helix for Control, TSA treated and Activated cells. Reproduced from [1]. The ratio of β-sheet to α-helix as determined by the ratio between the $\sim$1656 cm^{-1} and $\sim$1642 cm^{-1} peaks. The maximum of the peaks was determined for each cell treatment.*

treatments. The main variation in peak position was found in the Amide I (Figure 3.6C) and Amide II (Figure 3.6D) regions of the spectra. The Amide I band, which is attributed to the carbonyl stretching of the peptide group, has a doublet at $\sim$1654 and $\sim$1640 cm^{-1}, associated with α-helix and β-sheet structures, respectively[176, 185]. Peak shifts between cell treatments were not significant (Table 3.1).

3.6. Primary B cells

Undoubtedly, cell lines are valuable tractable models to study a wide range of biological processes. However, primary cells offer an even more physiological outlook at what is happening in animal cells *in vivo*. In fact, the results between cell lines and primary cells are not always in agreement because of the inherent differences between them. These differences, quantified by diverging transcriptional and proteomic profiles of a number of cell types[186–189], commonly relate to cell cycle, proliferation and metabolic processes. Therefore, primary B cells were isolated from mouse spleens and immune activated in culture.

3.6.1. Characterisation of primary B cells

There are inherent differences between cultured cell lines and primary cells, as stated above. Therefore, it was important to characterise a number of properties of the isolated cells through the different timepoints. Beyond checking that the cells were indeed undergoing CSR in response to the IL-4 and LPS treatment (Figure 3.7E),

changes to size (Figure 3.7A-B) and cell cycle phase distribution (Figure 3.7C-D) were also monitored.

The size of the cells increased going from day 0 (D0) to day 1 (D1) and further to day 2 (D2), as measured by flow cytometry (Figure 3.7A). The nuclear size also increased, although to a lower degree. This was measured by staining the cell nuclei with the DNA dye Hoechst and imaging them in microfluidic chips (Figure 3.7B). The difference in size influences the additional flow cytometry measurements, as the cells stained to different levels. This was the case for both PI staining of the DNA and staining with fluorescently tagged anti-IgM antibody, evident by the changes in signal intensity between timepoints (Figure 3.7C). It was therefore not possible to compare cells from different timepoints directly using gates based on the same signal intensities. However, relative changes in cell cycle phase distribution and number of IgM+/- cells were still possible to extract and therefore used to compare the different timepoints.

Immediatly post isolation from mice spleens (D0), almost all of the primary B cells were found to be G0 stalled (1×DNA). For the following timepoints (D1 and D2), the proportion of cells in S (>1×DNA) and G2/M (2×DNA) phase increased (Figure 3.7C-D). The growth medium, IL-4 and LPS stimulate the cells to proliferate, so the oberserved change in cell cycle phase distribution was expected.

The addition of IL-4 and LPS also stimulates cells to undergo CSR. This was monitored by staining the cells with fluorescently tagged anti-IgM antibody. As expected, the proportion of IgM+ cells was reduced at D4 compared to D0 (Figure 3.7E), indicating that a subset of the cells had switched from producing the IgM B cell receptor isotype to the IgG1 isotype.

3.6.2. FTIR spectral data from primary B cells largely follow the same patterns

FTIR imaging was again used to assess chromatin changes. The primary B cells were fixed for FTIR imaging immediately after isolation (D0) and then at two timepoints (D1 and D2) following culture in activating B cell medium containing LPS and IL-4.

Comparison of the FTIR spectra of primary B cells between D0, D1 and D2 showed the expected differences (Figure 3.8b). Single cell DNA-to-protein ratios made this more evident, with clear reductions at D1 from D0, and further reductions at D2 (Figure 3.8d). Whilst the peak ratio values vary from those of the CH12F3-2A,

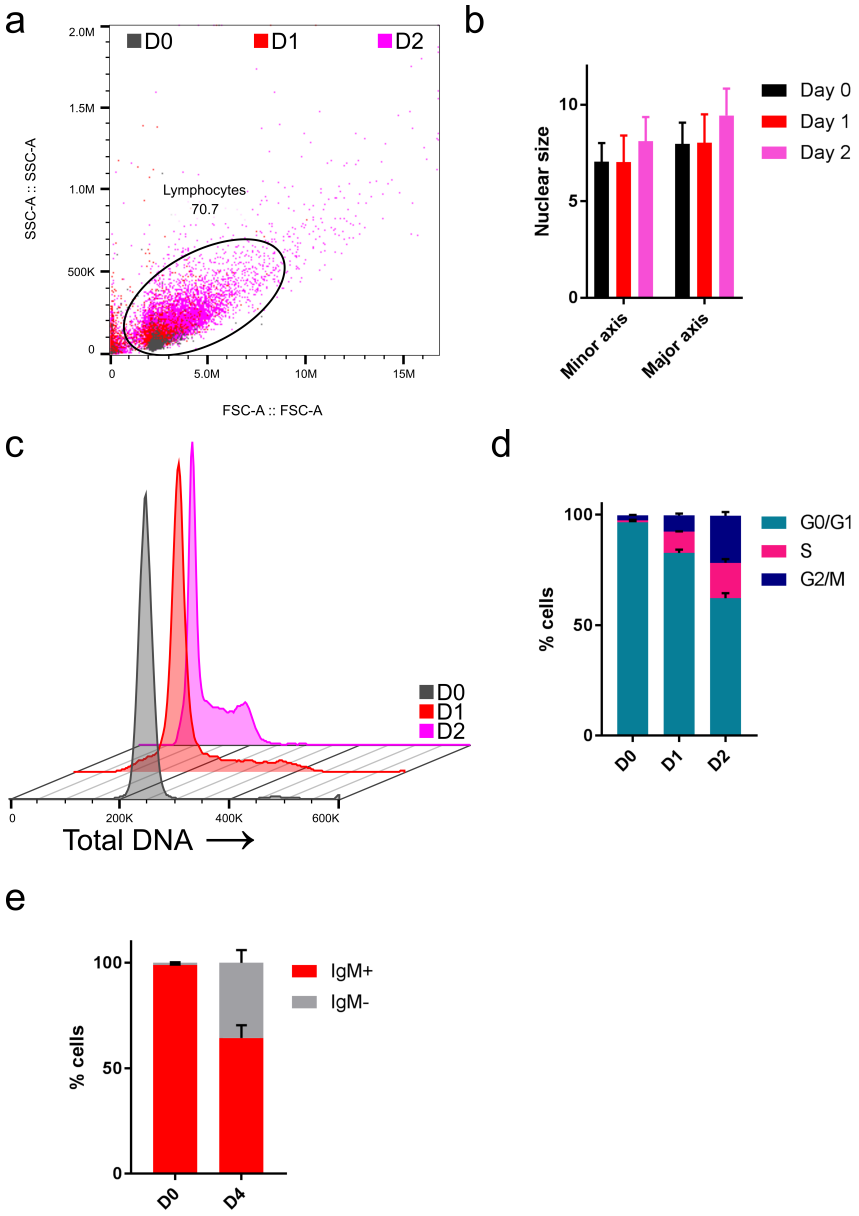

Figure 3.7.: *Size, cell cycle progression and class switch recombination for primary B cells. Reproduced from [1].* ***(a)*** *Flow cytometry data showing changing in size (FSC-A: forward scatter) and granularity (SSC-A: side scatter) for primary B cells at the timepoints D0, D1, and D2.* ***(b)*** *Nuclear size changes for primary B cells at the timepoints D0, D1, and D2. Minor axis (a) and major axis (b) as defined in Figure 4.5c were measured for nuclear stained cells from each timepoint.* ***(c)*** *Cell cycle phase distribution for primary B cells at the D0, D1, and D2.* ***(d)*** *Quantified cell cycle phase distribution for primary B cells at the timepoints D0, D1, and D2. As the G0 stalled cells from the spleen (D0) start proliferating in culture (D1 and D2), the proportion of cells in D and G2/M phase increases.* ***(e)*** *Class switch recombination for primary B cells stained with an anti-IgM fluorescently tagged antibody, as measured by flow cytometry. Cell right after isolation from spleen (D0) were compared with cells cultures in medium with IL-4 and LPS for four days (D4). A reduction og IgM+ cells is seen over this time period.*

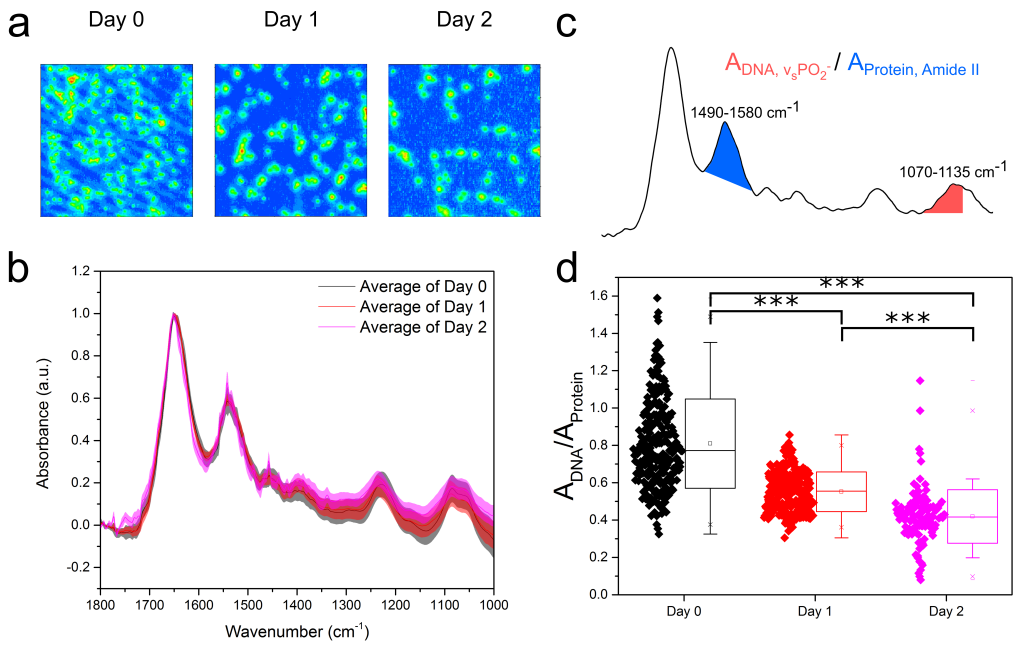

Figure 3.8.: *Primary murine B cells reveal are more complex picture. Reproduced from [1] with Figure 4.6.* ***(a)*** *FTIR images of cell samples fixed at immediately after isolation from mouse spleen (Day 0) and after being immune activated and cultures for 24 and 48 hrs (Day 1 and Day 2).* ***(b)*** *Average single cell spectrum for aech cell treatment. Standard deviation is marked as a shaded area.* ***(c)*** *Representative spectrum indicating the peak ratios used for the single cell analysis in (d).* ***(d)*** *DNA-to-Protein peak ratio showing the spectral changes associated with changes to DNA and chromatin in primary B cells at the single cell level. A t-test gave a statistically significant difference between samples (ns.: $P>0.05$, $*: P \leq 0.05, **: P \leq 0.01, ***: P \leq 0.001$).*

the changes between D0, D1, and D2 for the primary B cells follow the same expected pattern observed for CH12F3-2A activation with CIT (Figure 3.5H); thereby, strengthening the correlation between chromatin decondensation and reduction in this peak ratio.

3.7. Conclusion

A broad understanding of chromatin architecture dynamics is arguably one of the main hurdles to better understand cell function at the epigenomic level. Despite the numerous assays available to measure chromatin architecture, none so far can capture the full breadth of chromatin dynamics at the single cell level. That is why the FTIR imaging technique was optimised to visualise single cell chromatin changes during immune cell development. Immune B cells were chosen because of

their highly tractable properties in terms of proliferation, maturation, manipulation, and quantification.

3.7.1. Changes in DNA content can be assessed by FTIR imaging

Changes to intracellular DNA quantity and quality was assessed in single cells using a label-free chemically specific method based on FTIR spectroscopic imaging. The capability of FTIR to detect DNA changes was assessed by stalling cells in early S phase and G2/M phase. Focusing on DNA-to-protein peak ratios, the results show that stalled S and G2/M phase cells appeared significantly different from untreated control cells. The differences in this peak ratio between the differently treated cell populations followed the expected pattern considering the relationship between density and FTIR absorbance. Cells stalled in G2/M phase, where cells contain two-fold DNA content (2×), showed the highest intensity peak, while cells stalled in early phase, where cells only contain one-fold DNA content (1×), had the lowest. The untreated control cells, which contained cells in all phases, were in between the two.

3.7.2. Chromatin decondensation can be assessed by FTIR imaging

DNA quality, or chromatin chemical and conformational state, was also assessed using FTIR imaging, with the analysis focusing on the same peak ratio. TSA and CIT treatment of cells induce global transcriptional activation and specific B cell maturation, respectively. Both treatments result in chromatin decondensation, and both were associated with a decrease in the DNA-to-protein peak ratio. Assessment of cell cycle phase distribution demonstrated that these spectral changes were not originating from changes in intracellular DNA content, but rather changes to the chromatin architecture. This trend was further reproduced in primary B cells.

As the chromatin unravels passing from compact to an open and less ordered structure, the density of its components changes, with histone octamers essentially retaining their structure whilst the overall chromatin structure unfolds in terms of histone octamer spacing and decrease in DNA compaction. Due to the differential density, the DNA-to-protein ratio is a viable signature of chromatin structure and conformation. It is therefore reasonable to conclude that chromatin decondensation can be assessed through this peak ratio. Combining this technique with microfluidic devices to enable live cell imaging has the potential to provide a label-free method of assessing cell health or developmental state.

4. Single cell nuclear properties in response to mechanical deformation

The paper "Single Cell Imaging of Nuclear Architecture Changes"[1] forms the basis of the following chapter.

4.1. Background

The interaction between chromatin, the nuclear envelope and the cytoskeleton has been shown to alter transcription-associated responses through mechanotransduction[15, 27, 190, 191]. The mechanisms behind this nuclear mechanosensing are still not fully elucidated. Therefore, biomechanical properties of the nucleus are of great interest, for i) phenotypic characterisation of cell developmental changes, and ii) a better understanding of the mechanisms involved in mechanotransduction.

Auxeticity of the nucleus has previously been proposed to be an element in these signalling systems[124]. Auxeticity is the term used to describe the property of materials presenting a negative Poisson's ratio. This means that auxetic materials exhibit a cross-sectional expansion when stretched and a cross-sectional contraction when compressed. Most materials, on the contrary, are non-auxetic, becoming thinner when stretched and therefore having a positive Poisson's ratio. Nuclear auxeticity has been shown in transitioning ES cells, and chromatin decondensation has been determined to be a driver of this biomechanical property[124] (see subsection 1.4.3).

In this chapter, the role of chromatin conformation in mechanotranduction will be explored in B cells by deformability cytometry using microfluidic devices (Figure 4.1). Specifically, the biomechanical property *nuclear auxeticity* was examined.

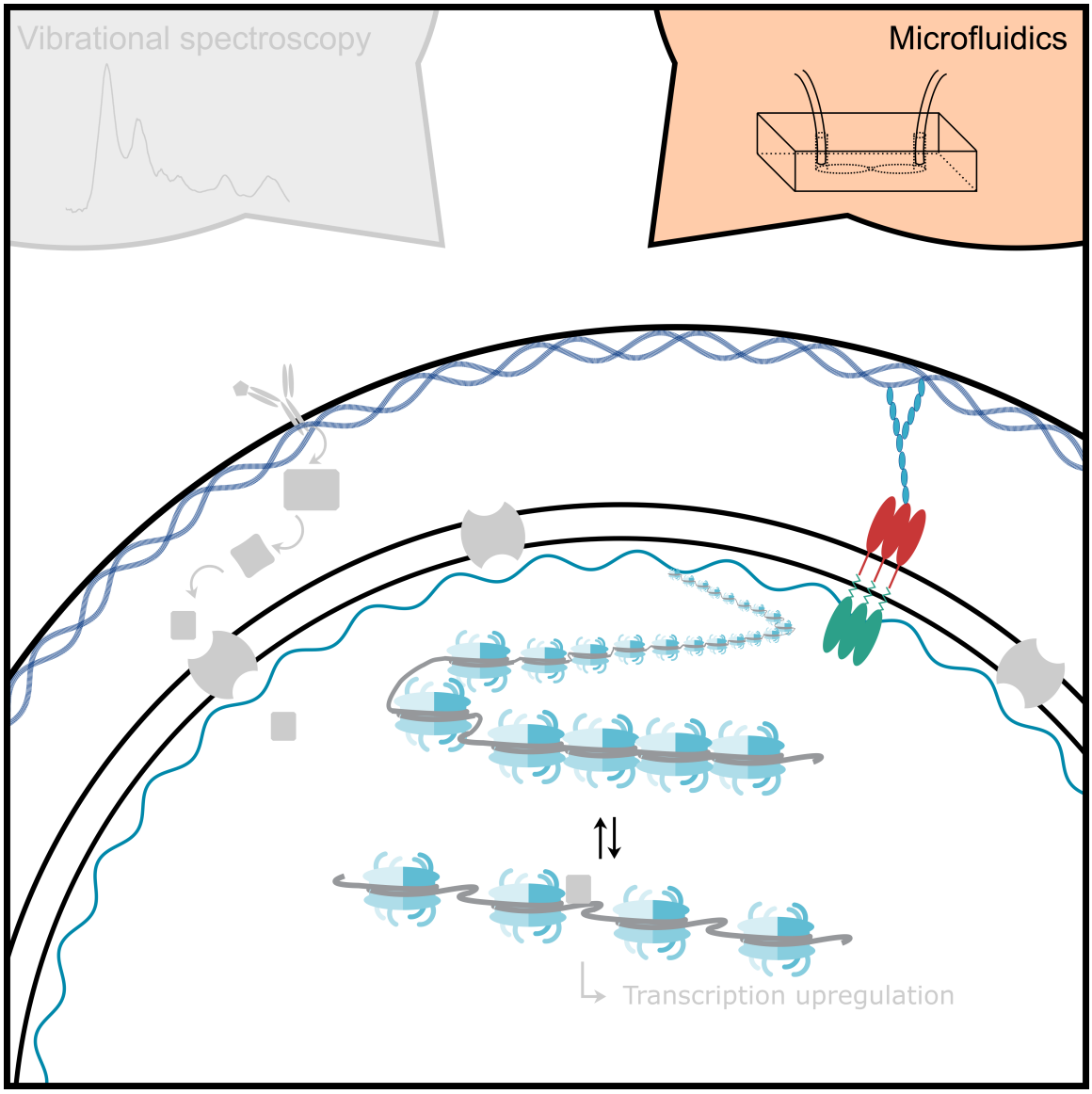

Figure 4.1.: *Thesis graphical summary - Chapter 4 focus.*
This chapter focuses on mechanotransduction and the biomechanical property nuclear auxeticity. The primary experimental technique used to assess this was deformability cytometry using microfluidic devices.

4.2. Chip design

In order to investigate possible auxetic properties in B cells, a specially designed microfluidic device was utilised. The device consisted of two large chambers for the fast delivery and collection of Hoechst stained live cells, connected via an array of channels with a square cross section of size $8\times8\mu m^2$, thus smaller than the typical size of the B cells under investigation (Figure 4.2a-b and Figure 4.3a). These channels enable stretching stresses to be imposed upon the cell nucleus caused by cytoskeletal strain when the cell is confined in the channel. Moreover, nuclei larger than the channel cross section also experience a transverse compression.

4.3. Image analysis

The nuclear deformation in response to the pressure applied to the outside of the cell was determined using a nuclear stain (Hoechst 33342) and an epifluorescence inverted microscope as described in section 2.7 and shown in Figure 4.3a-d. Further examination of changes in nuclear size was dependent on accurate identification of the nucleus within each frame and reliable tracking of the same cell between frames as described below.

4.3.1. Optimisation of thresholding for nucleus identification

Automatic identification of the nucleus in each frame required a thresholding algorithm. Distinguishing the nucleus from the background based on the fluorescence intensity appears relatively simple by eye (Figure 4.3b-d and Figure 4.4). However, a closer look at the intensity profile across a cell (Figure 4.4, inset) reveals a gradual transition from high intensity to background - with no discernible sharp edge or step. Therefore, three different thresholding algorithms (otsu[192], li[193] and yen[194]) were tested against manual measurements of 20 nuclei of cells translocating through the channels. Manual measurements were performed in Fiji[195] by drawing two lines (major and minor axis) through each cell nucleus and measuring the length of these lines.

Accurate measurements of the nuclei before entering and inside the channel - and the relation between the two - are of high importance for downstream analysis. Therefore, to assess the performance of the thresholding algorithms, the axial and transverse

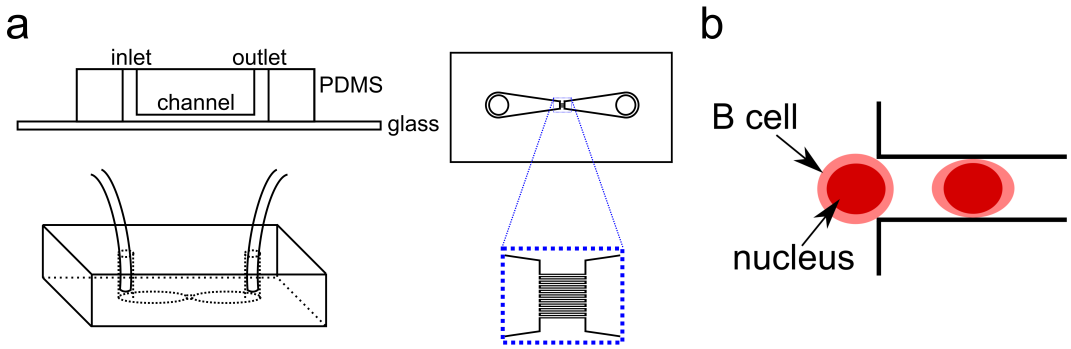

Figure 4.2.: *Chip design for investigating nuclear auxeticity in B cells. Reproduced from [1] with Figure 4.5.* ***(a)*** *Schematic of the microfluidic chip used to stretch cells.* ***(b)*** *Schematic of a cell moving through the channel. The cell is larger than the channel, but the nucleus is smaller.*

	$S_{T\text{-}dif}$	$S_{T\text{-}dif}$		$S_{A\text{-}dif}$	$S_{A\text{-}dif}$	
	$\bar{S}_{T\text{-}dif}$	σ	$\sum\|S_{T\text{-}dif}\|$	$\bar{S}_{A\text{-}dif}$	σ	$\sum\|S_{A\text{-}dif}\|$
otsu	-0.015	0.136	2.301	-0.175	0.152	4.026
li	-0.036	0.107	1.699	-0.089	0.121	2.698
yen	0.018	0.126	2.018	0.028	0.157	2.842

Table 4.1.: *Thresholding algorithms compared to manual measurements. $S_{X\text{-}dif}$ = Threshold(S_X) - Manual(S_X) was calculated for each nuclei. The mean, $\bar{S}_{X\text{-}dif}$, standard deviation, σ, and sum of the absolute values, $\sum|S_{X\text{-}dif}|$, were used to compare the performance of the three thresholding algorithms.*

strains were calculated for each algorithm and compared to the manual measurements. $S_{T\text{-}dif}$ and $S_{A\text{-}dif}$ were calculated for each nuclei:

$$S_{X\text{-}dif} = Threshold(S_X) - Manual(S_X) \tag{4.1}$$

The thresholding algorithm li exhibited the smallest divergence from the manual measurements - illustrated by the smallest sum, $\sum|S_{X\text{-}dif}|$, as well as the smallest standard deviation, σ (Table 4.1).

4.3.2. Cell tracking

After automatic identification of cell nuclei in each frame, a frame-by-frame one-to-one tracking was applied to follow each nucleus as it moved from left to right through the field of view (Figure 4.3e-g). Based on a white-light image of the field of view (Figure 4.3a), three zones were defined: the inlet (zone 0), the channels (zone 1) and

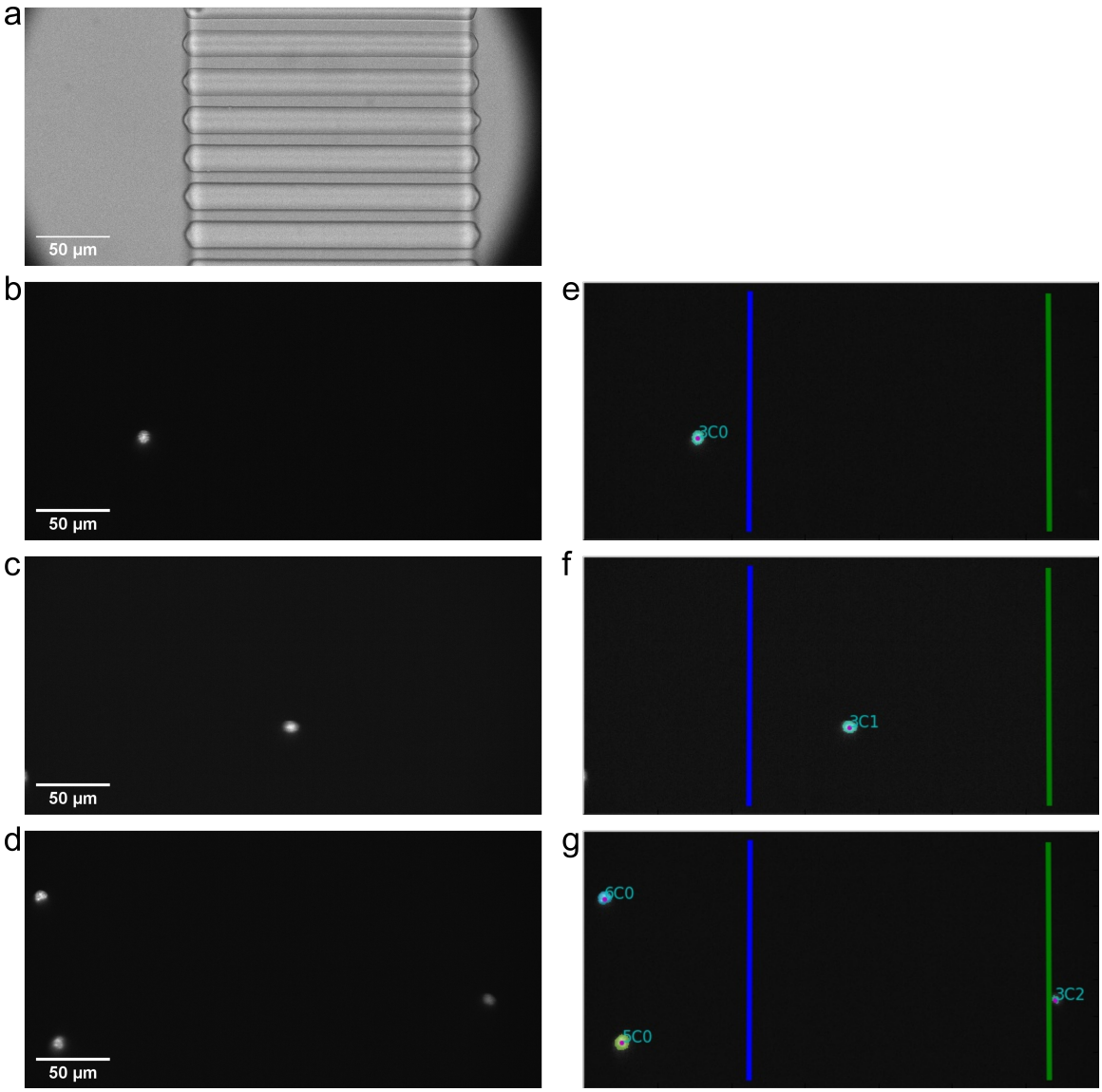

Figure 4.3.: *A cell translocating one of the microfluidic channels.*
(a-d) reproduced from [1]. ***(a)*** *White-light image of the microfluidic chip showing the channels.* ***(b-d)*** *Fluorescent images of a Hoechst stained cell translocating one of the microfluidic channels. The fluorescent shape is the nucleus.* ***(e-g)*** *The same frames showing the cell tracking at work.* ***(b and e)*** *Cell in the inlet approaching the channels.* ***(c and f)*** *The same cell translocating one of the microfluidic channels.* ***(d and g)*** *The same cell in the outlet. A further two cells on the left approaching the channels.*

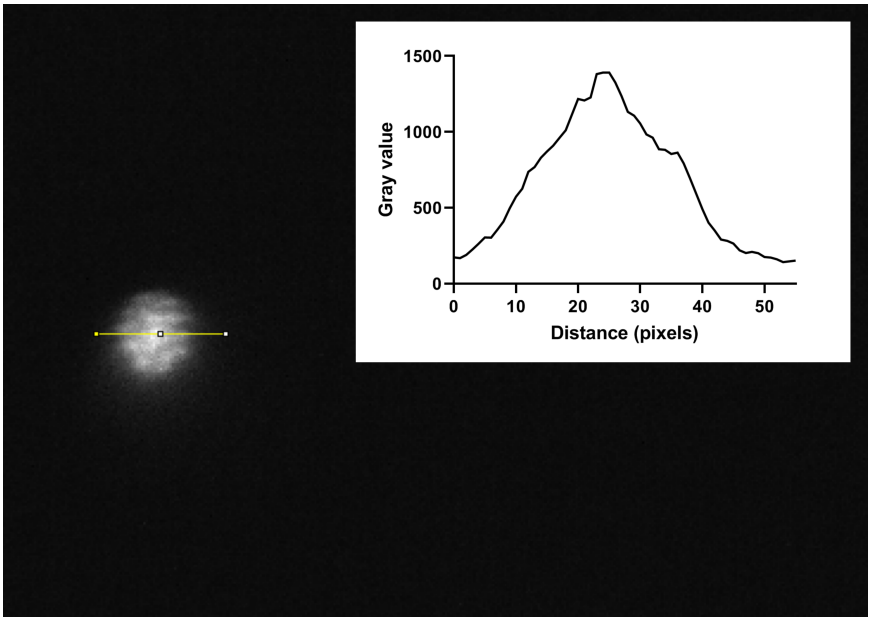

Figure 4.4.: *Intensity plot of example cell.*
A zoomed in version of a single cell, with a line drawn through it. The insert shows the intensity plot through the line.

the outlet (zone 2). Hence, properties of individual nuclei, such as axis sizes, could be recorded for each frame and as an average for each zone.

4.4. Nuclear deformation is affected by chromatin changes

The assay was used to examine the effects of TSA and CIT treatment of CH12F3-2A cells on nuclear deformation in response to applied mechanical stress. Both TSA and CIT initiate chromatin decondensation, as previously discussed (subsection 3.5.1. The transverse strain, quantifying the deformation of the nucleus due to the channel confinement in the direction perpendicular to the channel's longitudinal axis, was used as a proxy for nuclear auxeticity[124] (Figure 4.5a-b). By tracking single cells, as they moved through the channels, this axis size was determined for each cell before they enter the channel (a) and during the translocation through the channel (a'). The transverse strain was calculated from these values for each cell. A positive transverse strain indicates auxetic properties.

Untreated CH12F3-2A cells (Control) did not exhibit auxetic properties during the translocation through the channels. Instead their nuclei became thinner as indicated by the negative transverse strain (Figure 4.5c). In contrast, both TSA and CIT treated cells contained a subpopulation of cells that had positive transverse strains

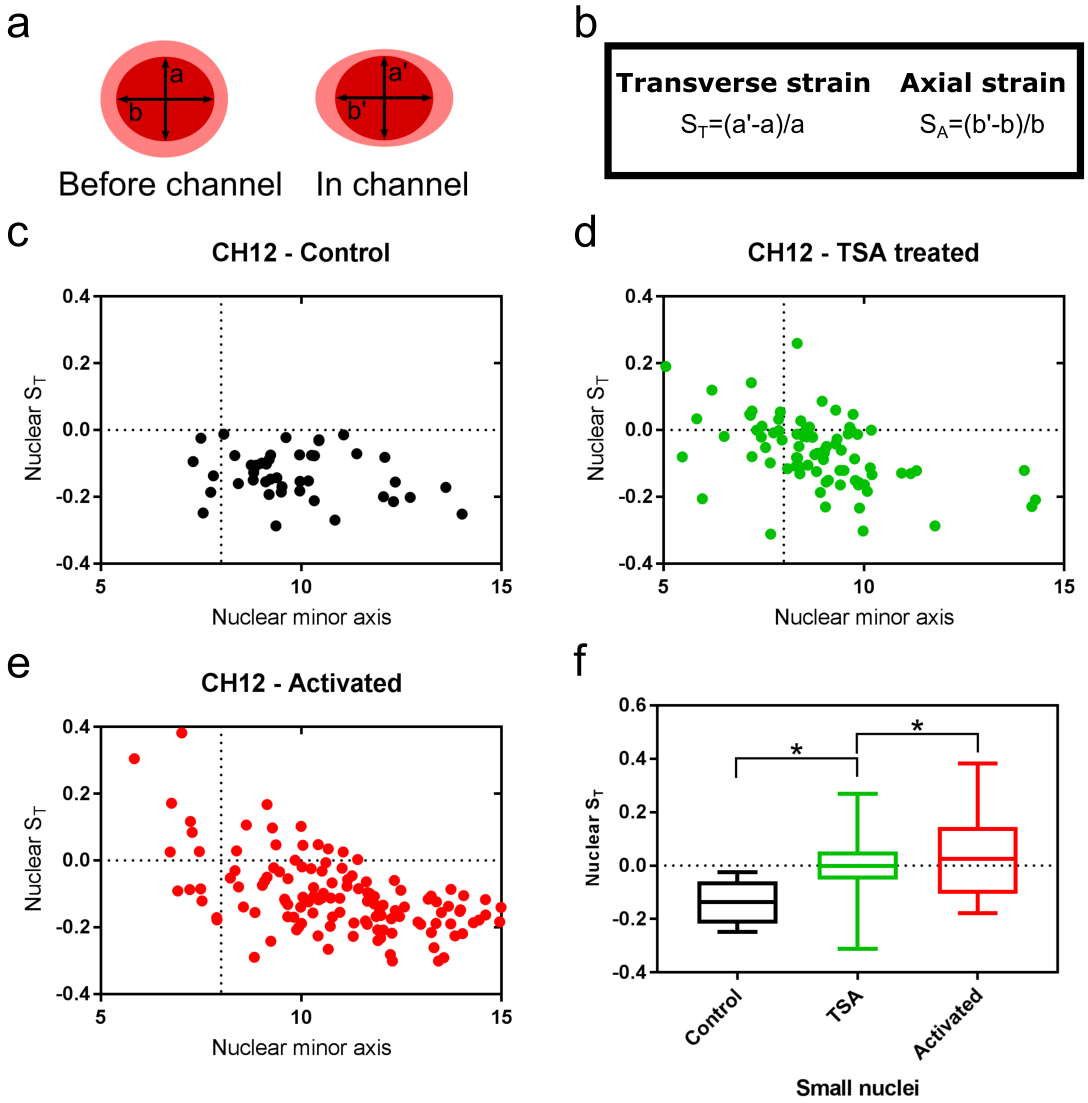

Figure 4.5.: *Chromatin decondensation is correlated with auxetic nuclei of B cells. Reproduced from [1] with Figure 4.2.* ***(a)*** *The axes measured for each nucleus before the channel and in the channel.* ***(b)*** *Transverse and Axial strain calculations based on the axes seen in (a).* ***(c)*** *Transverse strain versus nuclear minor axis for Control cells.* ***(d)*** *Transverse strain versus nuclear minor axis for TSA treated cells.* ***(e)*** *Transverse strain versus nuclear minor axis for Activated (CIT treated) cells.* ***(f)*** *Quantification of the change in transverse strain for small nuclei (¡8µm), i.e. nuclei smaller than the channel width. A t-test gave a statistically significant difference between samples (ns.: $P>0.05$, $*:\leq 0.05, **: P \leq 0.01, ***: P \leq 0.001$).*

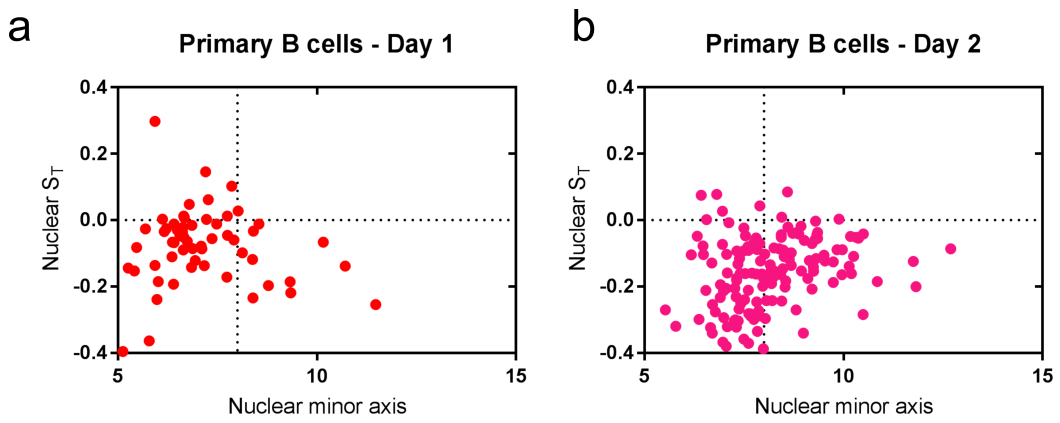

Figure 4.6.: *Primary murine B cells reveal are more complex picture. Reproduced from [1] with Figure 3.8.* ***(a)*** *Transverse strain versus nuclear minor axis for 'Day 1' primary B cells.* ***(b)*** *Transverse strain versus nuclear minor axis for 'Day 2' primary B cells.*

(Figure 4.5d-e). As expected, these cells were primarily found within the group of cells that had nuclei smaller than the channel width and thus could expand in volume in the channel exhibiting an auxetic behaviour. The difference in transverse strain values of small nuclei cells between treated and untreated cells were found to be statistically significant (Figure 4.5f). Finally, no correlation was found between auxeticity and cell speed.

4.5. A subset of activated primary B cells also have auxetic nuclei

The assay was also used to examine the effect of primary B cell activation through incubation with LPS and IL-4. Characterisation of these cells was described in section 3.6. The primary B cells were measured at two timepoints following activation: D1 and D2. Immediately after isolation (D0) from mouse spleens the cells were very small (see Figure 3.7a). Additionally, they were more prone to sticking to each other and to the entrance of the channels. Therefore, it was not possible to use the assay to examine these.

Similarly to TSA and CIT treated CH12 cells, the activated primary B cells contained a subpopulation of nuclei that had positive transverse strains (Figure 4.6a-b). Again, these cells were primarily found among cells with nuclei smaller than the channel width. Unlike the CH12 cells, the primary B cells had a large number of small nuclei that had negative transverse strains.

4.6. Conclusion

4.6.1. Correlation between chromatin decondensation and auxetic nuclei in B cells

The correlation between chromatin decondensation and nuclear mechanical properties was assessed using epifluorescence and microfluidics, examining the recently identified cellular property termed nuclear auxeticity[124]. Interestingly, both TSA treatment and CIT activation of B cells resulted in similar auxetic responses, while untreated controls did not. The data shows, for the first time, that lymphocyte maturation can elicit a mechanical conformational change within the overall cellular structure. The data also suggest that nuclear auxeticity correlates with actively decondensing chromatin, which also coincides with the stem cell reprogramming properties previously identified[124].

4.6.2. Primary murine B cells reveal a more complex picture

The primary cell data support the hypothesised correlation between nuclear auxeticity and actively decondensing chromatin. However, it does reveal a more complex picture, where nuclei size alone (in relation to channel size) does not determine the cells' potential for nuclear auxeticity. The activation of the primary B cells was verified by flow cytometry measurements of the resulting CSR (Figure 3.7e). For both CH12 and primary cells, only a subset of cells actually undergo CSR. However, the majority of cells are believed to initiate chromatin decondensation in response to the activation signalling initiated by the cytokines. If primary B cells respond differently *ex vivo* has yet to be determined. The nuclear auxeticity data certainly indicate that some heterogeneity exists.

5. Live cell vibrational spectroscopy measurements

5.1. Background

Vibrational spectroscopy measurements can provide label-free characterisation of intracellular biochemical changes in cells. While fixation of samples may introduce spectral artefacts, the techniques can still provide valuable insights into biochemical differences between cell populations, as long as sample preparation is consistent (as explored in chapter 3 using FTIR imaging). However, there are still several reasons supporting the pursuit and optimisation of vibrational spectroscopy live cell measurements.

Firstly, hydration is important for the native structure of both proteins and nucleic acids. Therefore, spectral information of live cells may reveal changes that fixed, dehydrated cell measurements cannot. Secondly, with the right setup it may be possible to follow the same cell as it responds to environmental stimuli or undergoes differentiation. Thirdly, the ability to characterise cells in label-free manner, followed by downstream processes of the same cells - with no interference from labels or destruction of the sample - is possibly the greatest potential of vibrational spectroscopy in biological and biomedical research.

Microfluidic devices, made from a variety of materials, have been used for live cell vibrational spectroscopy measurements[111–119]. The devices are often made from the standard FTIR and Raman substrate calcium fluoride. There are important limitations to this approach, including cost and fabrication difficulties. For conventional microscopy purposes, microfluidic chips are often made from the polymer PDMS ([125, 140, 143–145, 147, 148] and chapter 4). These devices are versatile and biocompatible. In contrast to the calcium fluoride based microfluidic devices, they are cheap to make. Because of this, they are single-use devices, hence preventing sample contamination. The PDMS chips are made via replica moulding - creating a negative imprint of a silicon mould. This process ensures high consistency between chips. Therefore, PDMS based devices could be a valuable alternative to calcium fluoride based devices.

In this chapter, the suitability of PDMS based microfluidic devices for live cell FTIR and Raman measurements will be explored.

5.2. Combining FTIR imaging with PDMS based microfluidic chips

In the design of a microfluidic chip for use with FTIR imaging in transmission mode, two goals were set. First, the channel height had to be be reduced to the size of a single cell - effectively reducing the path length and water contribution to the FTIR spectrum. Second, the thickness of the PDMS layer was to be reduced as much as possible, while still maintaining the integrity of the chip. This was necessary because PDMS is not transparent in the mid infrared region (4000 - 400 cm^{-1})[196].

The first goal could easily be addressed in the design of the silicon mould, where the channel height was set at 20 μm or less. The second goal required modifications to the chip during the replica moulding process. Fabrication of PDMS chips with a "sampling window", where the PDMS layer is very thin ($\sim$250 μm), set on top of the calcium fluoride substrate, was proposed (Figure 5.1a-b). This could allow for subtraction spectra to be calculated and the absorptions due to PDMS to be removed.

5.2.1. PDMS has high IR absorption within nucleic acid signal range

To test the feasibility of subtracting absorptions due to PDMS from cell measurements, FTIR images of thin PDMS layers were collected. The "sampling window" was constructed in three steps, 1) a thin layer of PDMS was spincoated onto the silicon mould, 2) a small cube was placed in the centre of the mould, and 3) more PDMS was added around the cube. The chip was placed on a calcium fluoride substrate and FTIR images of the sampling window were collected. Individual pixel spectra were extracted from the image. They all looked similar; a representative spectrum is shown in Figure 5.1c.

PDMS has high IR absorption within in the 3800-1000 cm^{-1} region, in particular around 1300-1000 cm^{-1}. The PDMS spectral profile has one sharp and one broad peak of high absorbance in this region. Furthermore, it shows saturation of the spectrum within the region. Therefore, it is not feasible to subtract the PDMS

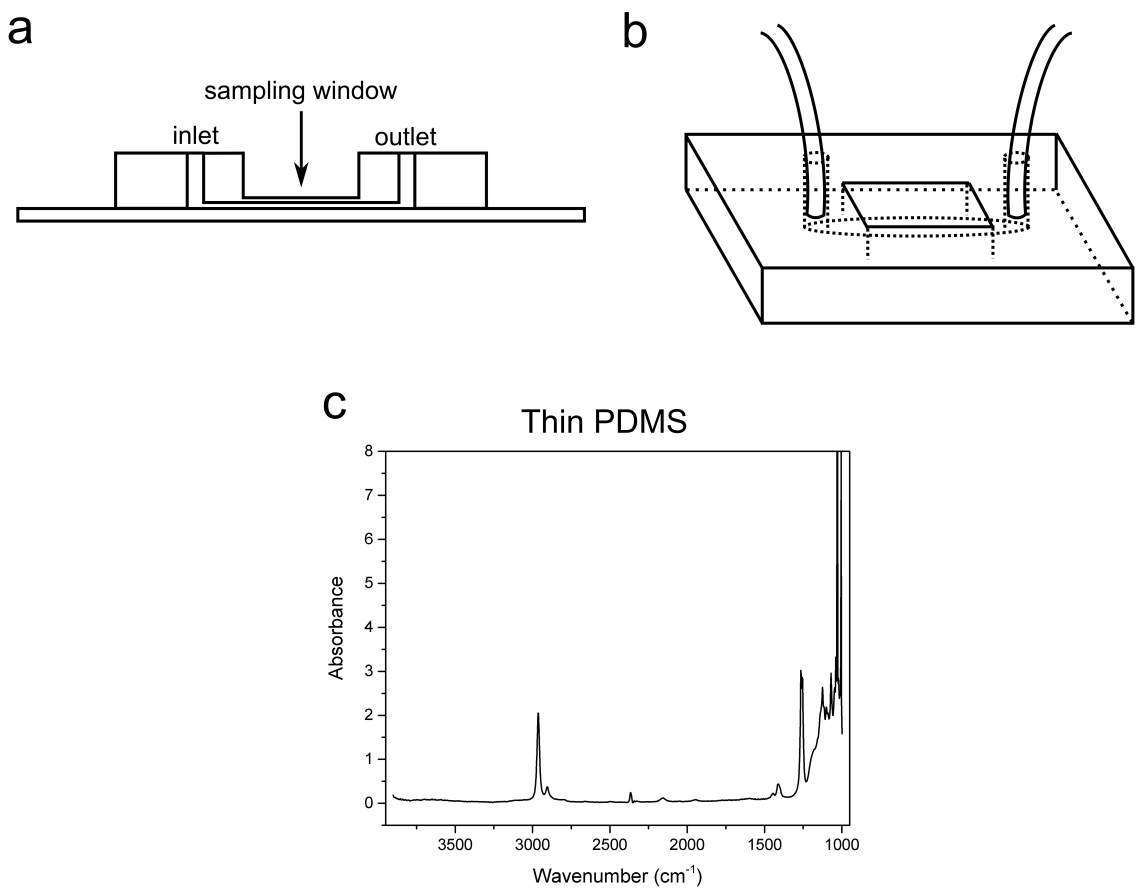

Figure 5.1.: *PDMS gives rise to high IR absorption.*
(a-b) *Graphical representation of chip design.* ***(c)*** *Single pixel spectrum of thin PDMS layer.*

spectrum from sample measurements in the 1300-1000 cm^{-1} region. Vibrational modes of nucleic acid, namely $\nu_s(PO_2^-)$ and $\nu_{as}(PO_2^-)$, are found within the 1300-1000 cm^{-1} region (Figure 2.2 and Appendix B). It was not possible to maintain the integrity of the microfluidic device with thinner PDMS layers. FTIR imaging in combination with PDMS based microfluidic chips was therefore not suitable for measurements of chromatin changes.

5.3. Combining Raman mapping with PDMS based microfluidic chips

Raman spectroscopy is a complementary technique to FTIR spectroscopy. Compared to FTIR imaging, Raman mapping poses fewer restrictions on microfluidic chip de-

sign. Water is a weak Raman scatterer and is therefore not a problem, so channel height need not be limited. Addtionally, Raman microscopy involves the use of a backscattering geometry and therefore there is no limitation from light transmission through thick samples. Further, by using a confocal system such as WiTec alpha300 R (subsection 2.5.2), PDMS can be excluded from the sampling volume of scattering. This removes the need for post-measurement subtraction of PDMS signal. For the design of a microfluidic chip for use with Raman mapping, two goals were therefore set. First, PDMS was to be excluded from the sampling area. Second, the cells had to be kept still during measurements, which are normally lengthy for spontaneous Raman techniques. Once the chip design was optimised further measurements were considered, including suspension media composition.

5.3.1. PDMS chip and 3D printed holder

Two chip designs were tested for Raman mapping of live cells. Both chips were bonded to glass coverslips and held upside down during the measurements (Figure 5.2a). A custom holder was 3D printed to hold the chip in place (Figure 5.2b).

The first chip design, the trap chip, consisted of a large chamber with PDMS structures (traps) for keeping cells in place (Figure 5.2c). The chamber height was 50 μm. Cells were flowed into the chip and left to settle on the glass for 30 min, before the chip was turned upside down and inserted into the chip holder. It was noted that cells outside of traps adhered to the glass and remained in place when the chip was turned upside down (Figure 5.2e). A single measurement was taken from within a cell (Figure 5.2g, marked by a circle, measurement point indicated by a black cross). The spectrum was dominated by high intensity peaks associated with PDMS. A measurement of the PBS media surrounding the cell (Figure 5.2g, red) confirmed that the peaks were not associated with the molecular composition of the cell. It was thus determined that the trap chip did not meet goal one; excluding PDMS from the sampling area.

The second chip design, the cavity chip, consisted of a large chamber with a height of 500 μm (Figure 5.2d). As before, cells adhered to the glass and remained still during measurements, so there was no need for PDMS traps (Figure 5.2f). A single measurement from the middle of a cell gave a spectrum consisting of peaks associated with biomolecules and water, and no PDMS associated peaks (Figure 5.2h). The cavity chip design met both goals set out and was used for the subsequent experiments.

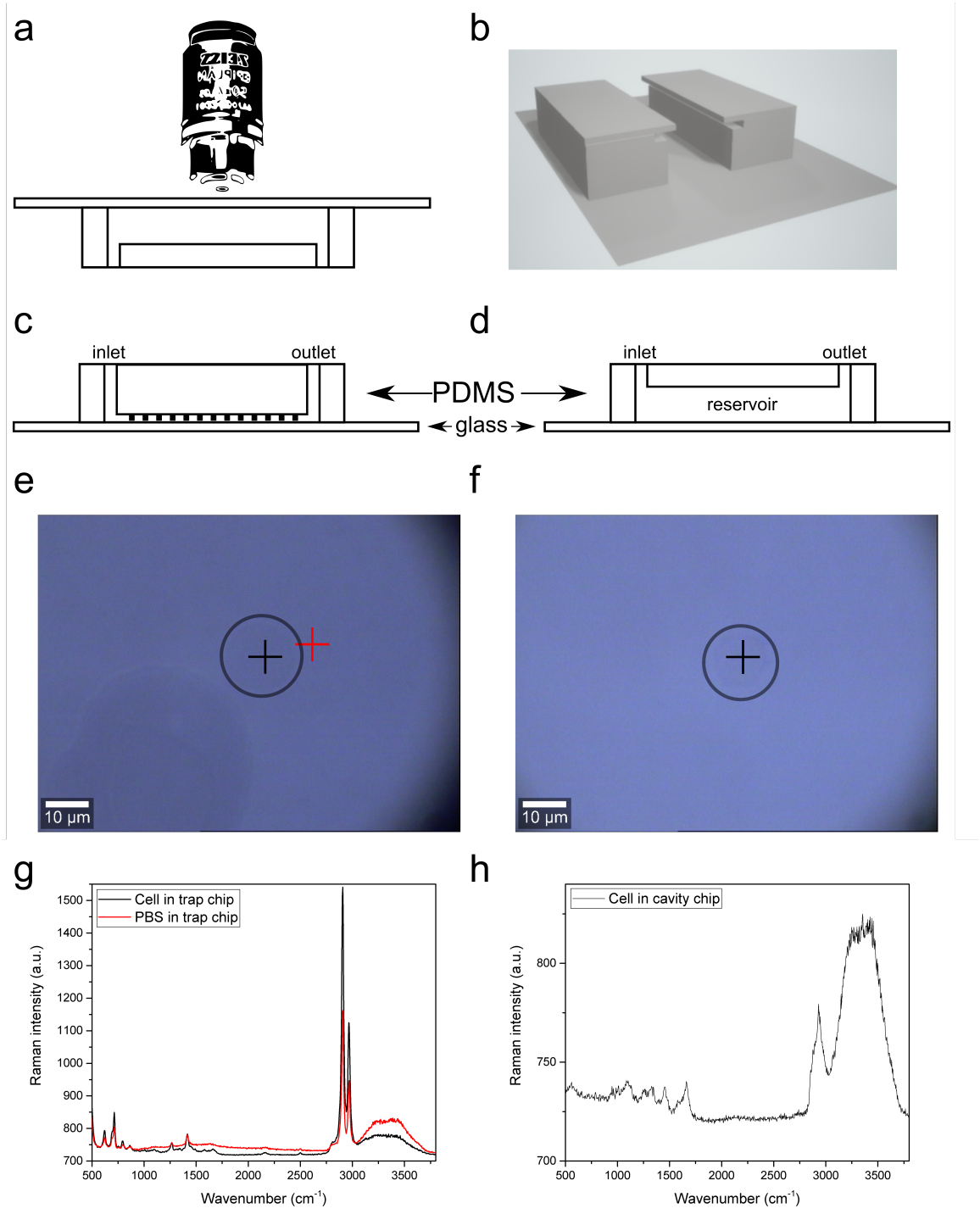

Figure 5.2.: *Chip design choice for Raman measurements.*
(a) *Chip held upside down for measurements.* ***(b)*** *Custom chip holder to hold chip upside down.* ***(c)*** *Trap chip design.* ***(d)*** *Cavity chip design.* ***(e)*** *Trap chip measurement positions.* ***(f)*** *Cavity chip measurement position.* ***(g)*** *Trap chip cell and PBS Raman spectra.* ***(h)*** *Cavity chip cell Raman spectrum.*

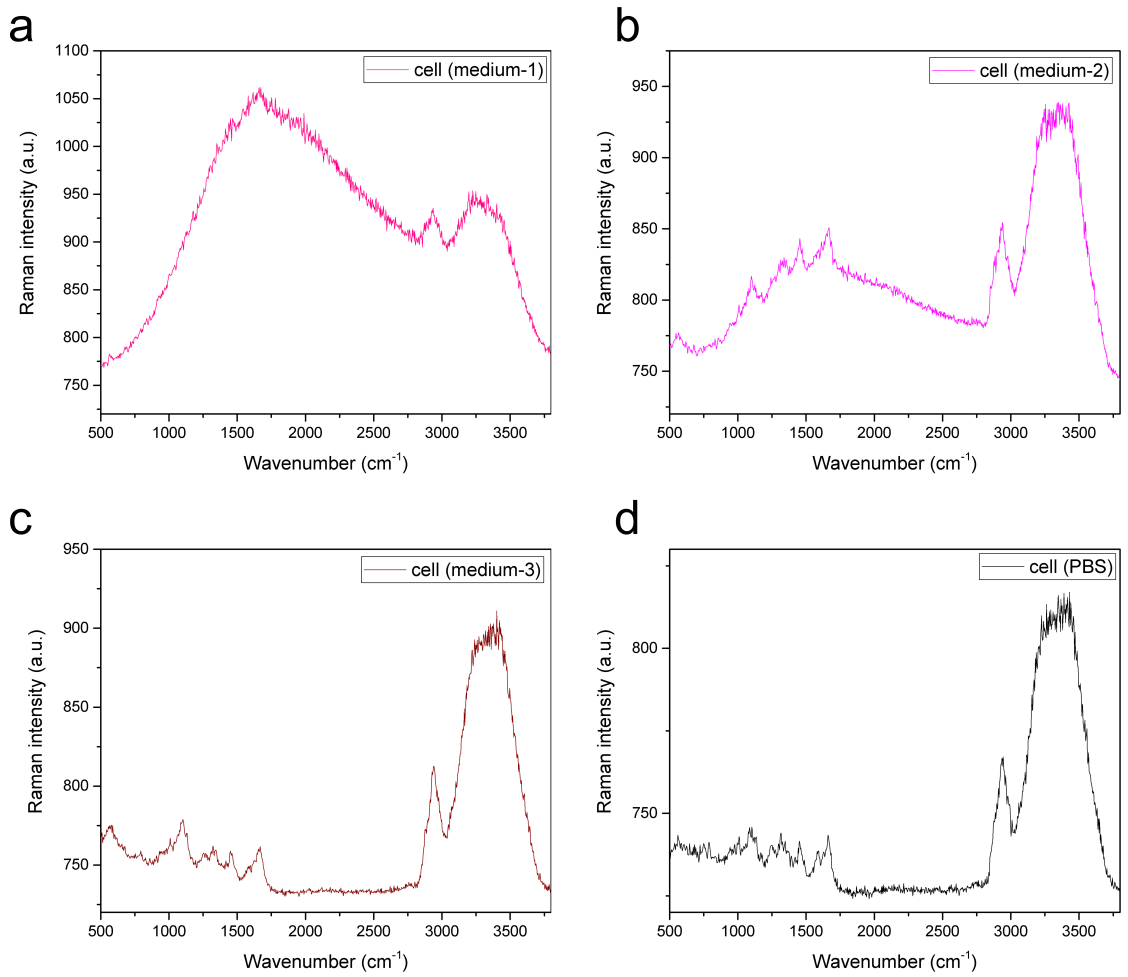

Figure 5.3.: *Live cell Raman measurements.*
(a) *Raman spectrum from cell in medium-1.* ***(b)*** *Raman spectrum from cell in medium-2.*
(c) *Raman spectrum from cell in medium-3.* ***(d)*** *Raman spectrum from cell in PBS.*

5.3.2. Media versus PBS

For live cell measurements, the chosen suspension medium is of great importance. Two - sometimes opposing - objectives should be kept in mind. First, the medium should be as similar as possible to the culture medium of the cells in order to ensure good cell health. Second, the medium should not interfere with the cell measurements and spectral interpretations. Culture medium contains, among other molecules, sugars and amino acids, so a compromise between the two objectives is necessary. Three different media compositions were tested (Figure 5.3) and compared with PBS, which is a phosphate-buffered saline solution with ion concentrations and osmolarity that matches the cells. Thus, PBS is the minimum suspension medium needed for cell viability during measurements.

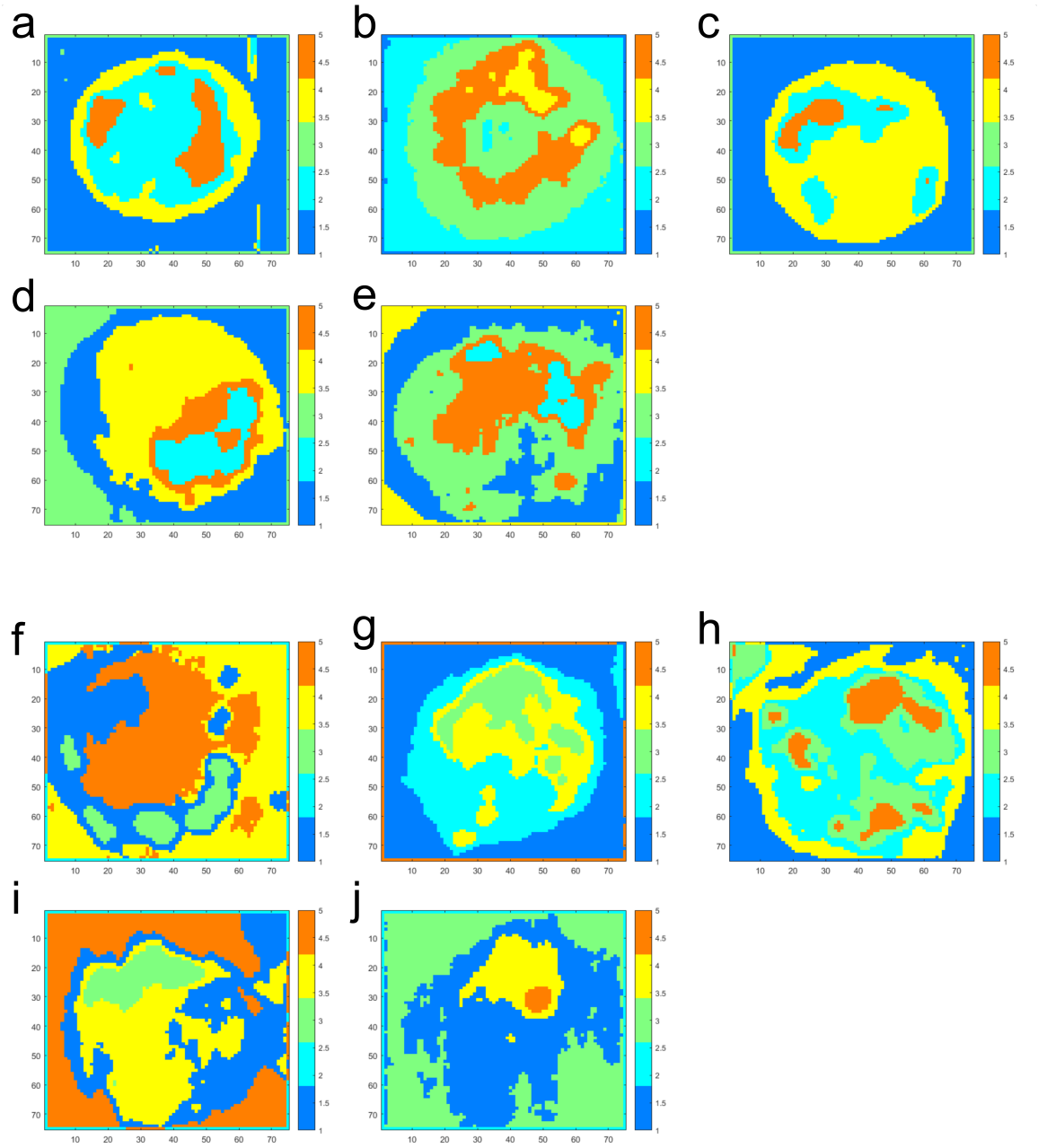

Figure 5.4.: *Raman maps of live cells in PBS and culture medium. K-means analysis, using five clusters, of Raman maps of cells.* ***(a-e)*** *Cells in PBS.* ***(f-j)*** *Cells in media-3.*

The first tested media composition, 'medium-1', was identical to the culture medium the cells were grown in (subsection 2.1.1). RPMI, the main constituent of the culture medium, contains the pH indicator Phenol red, which is a major source of fluorescence. The Raman spectrum from a cell in this medium reflected this (Figure 5.3a).

The second media composition, 'medium-2', was made with Phenol red-free RPMI. A Raman spectrum from a cell showed that some fluorescence remained (Figure 5.3b). This was determined to originate from the NCTC-109, which also contained Phenol red, or the fetal bovine serum (FBS), which comes from blood. The cells are unable to proliferate without FBS. Medium depleted of FBS therefore offers no advantages over PBS in terms of cell viability.

The final media composition, 'medium-3', was identical to 'medium-2' bar the omission of NCTC-109. A Raman spectrum from a cell (Figure 5.3c) showed no fluorescence and a spectrum very similar to that of a cell in PBS (Figure 5.3d). To further examine the suitability of this media composition for Raman mapping of live cells, five Raman maps of cells in PBS and five Raman maps of cells in 'medium-3' were compared (Figure 5.4). K-means cluster analysis using five clusters was applied to each map. The performance of this analysis provided insights into the similarity of spectra from the cell and spectra from the surrounding medium.

For each map, it is possible to discern the cell from the surrounding medium. It varies between cells how good this separation is. The five Raman maps of cells in PBS (Figure 5.4a-e) have smoother boundaries between cell and medium, compared with the five Raman maps of cells in 'medium-3' (Figure 5.4). For especially three 'medium-3' cells, the segmentation is ambiguous in multiple areas of the maps (Figure 5.4f,i,j). The analysis also reveals intracellular structures for most cells. These vary in size and shape between cells as well.

5.4. Conclusion

5.4.1. PDMS based microfluidic chips are suitable for Raman mapping

Live cell analysis have previously been shown using both FTIR imaging and Raman mapping[111–119]. PDMS based microfluidic chips are compatible with both techniques depending on the wavenumber range of interest. However, because of the high

IR absorption of PDMS in the 1300-1000 cm^{-1} region, it is not suitable for transmission mode FTIR imaging of chromatin changes.

For this thesis work, vibrational spectroscopy measurements of live cells in PDMS based microfluidic devices were therefore performed using Raman mapping. The cavity chip design was shown to be the most suitable, as it enabled the exclusion of PDMS from the sampling area.

5.4.2. PBS versus culture medium

The viability and health of cells during measurements are important factors. For time course experiments, culture medium is a necessity to enable cell proliferation. Raman maps of cells in media composition 'medium-3', which is similar to the culture medium used for CH12F3 cells, was shown to be possible with minimal spectral interference from the medium. NCTC-109, the only removed component, is not necessary for cell proliferation. The chip holder has space for the attachment of tubing, which would allow for the media exchange necessary for continuous cell maintenance. Control of CO_2 levels and temperature of the medium (or the whole microscope sample area), could enable continuous measurements of single live cells.

The k-means cluster analysis of Raman cell maps indicated a larger similarity between cells and 'medium-3', than between cells and PBS. This similarity may complicate downstream analysis of the Raman spectra. For this thesis work, single live cell maps of activated and control (unactivated) CH12F3 cells were required. Continuous measurements were not needed. Spectral quality and clarity was prioritised. All further live cell measurements were therefore performed on cells suspended in PBS.

6. Label-free live cell chemical imaging using Raman spectroscopy

The manuscript "Single Cell Label-free Probing of Chromatin Dynamics during B Lymphocyte Maturation"[2] forms the basis of the following chapter.

6.1. Background

Raman microscopy of live cells provides a snapshot of the biochemical composition of the cells. The spectral output of Raman measurements could potentially be used for phenotypic characterisation of single cells. To do so in a meaningful way, the underlying biochemical pathways and structures affecting the Raman spectra must be unravelled.

In yeast and bacteria, a linear correlation has been found between Raman and transcriptomic measurements[102]. Understanding this correlation, and predicting Raman data from transcriptomic data - and vice versa - has great potential for improving our understanding of the spectral output from Raman measurements. The transcripts with the highest importance for the linear correlation were identified in both yeast and bacteria. In yeast, these were primarily non-coding RNAs. In bacteria, they were primarily ribosome-related transcripts. The correlation between them does not mean that the Raman spectra directly measure the expression levels of the transcripts in question. Instead the downstream effects - i.e. changes to expression levels of large groups of genes and the resulting change in biochemical compositions of the cells - are quantified by Raman. Thus, by analysing the correlation between Raman spectra and transcript expression levels, the key cellular pathways affecting the biochemical profile assessed by Raman spectroscopy may be identified.

To my knowledge, i) this correlation between Raman spectra and transcriptomic readouts has never been studies in mammalian cells, and ii) it has not been examined in the context of cell differentiation. To explore this correlation in mammalian cells, B lymphocytes were again chosen as a model cell system. Immune activation of these

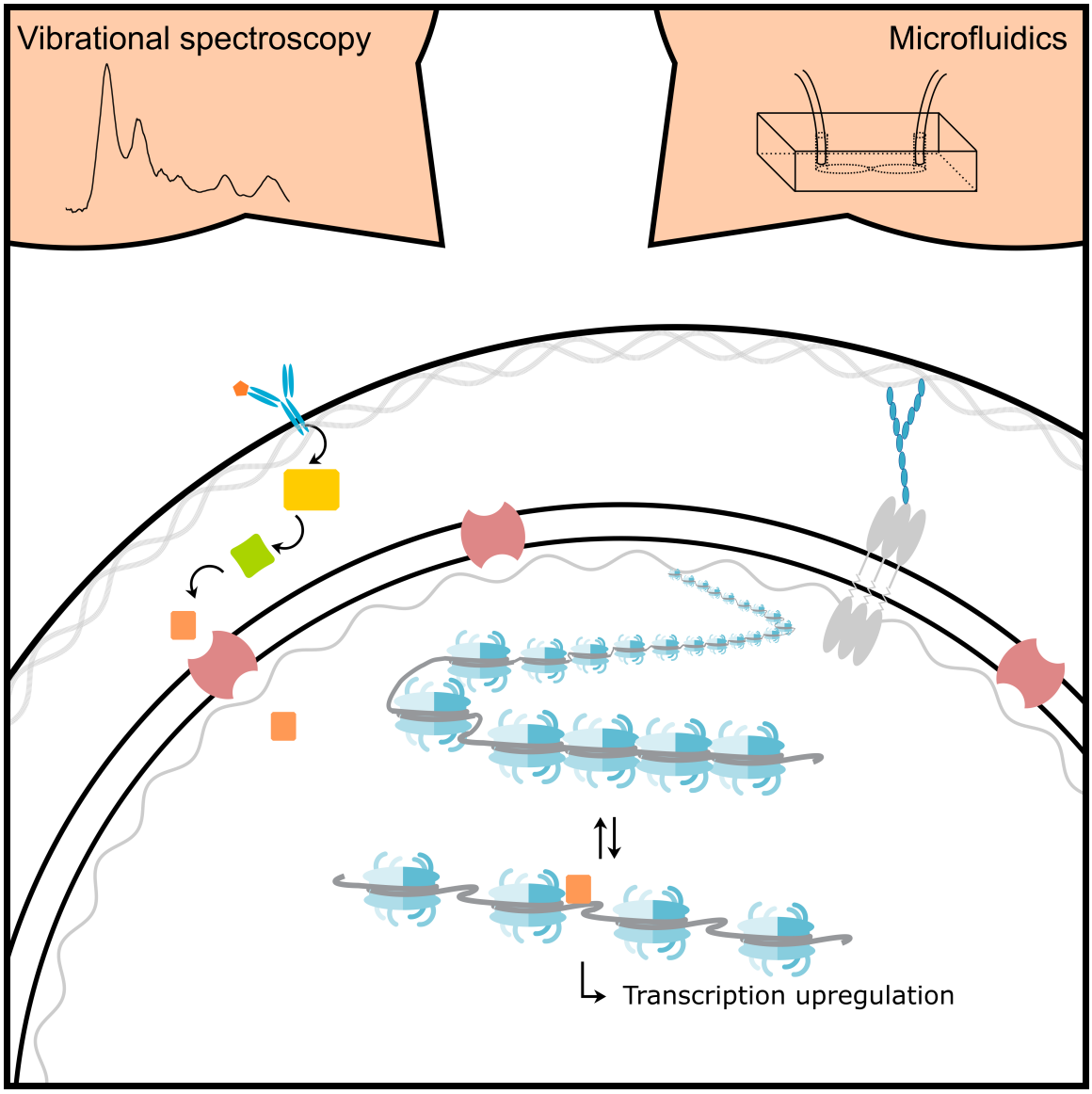

Figure 6.1.: *Thesis graphical summary - Chapter 6 focus.*
This chapter focuses on detecting chromatin decondensation in single live cells using microfluidic devices and the label-free technique Raman mapping. It further explores the correlation between Raman spectral data and transcriptomic data.

cells intiates large-scale changes to the transcriptomes, resulting in the differentiation of naïve B cells into mature B cells and class switch recombination (CSR) of the immuglobulin receptor. A large number of regulatory proteins and RNAs have been shown to be involved[9, 52, 55, 197–200]. However, the complex coordination of regulatory pathways and expression modulations is not yet fully understood. Novel techniques and approaches are needed to identify key regulatory RNAs and proteins previously unlinked to the B cell activation differentiation process.

In this chapter, the use of microfluidic devices and Raman mapping for the measurement and quantification of changes to chromatin conformation and general biochemical composition in single live B cells will be explored. The intracellular biochemical changes occurring during B cell activation will be examined by Raman, and the correlation between Raman spectral profiles and transcriptomic profiles will be used to establish the key biological pathways influencing the Raman spectra (Figure 6.1).

6.2. Identifying nucleus and cytoplasm in single cell Raman maps using common K-means

Raman maps were collected from 118 live CH12F3 cells suspended in isotonic PBS-filled microfluidic chambers. The cells remained in place throughout the measurements. Common k-means analysis was applied to identify cell (vs background) pixels, as well as to distinguish the nucleus from the cytoplasm within each cell (Figure 6.2a-c). Additional examples are shown in Figure 6.3a-c. Inspection of the cluster centroid spectra (Figure 6.2b) informed the segmentation.

The quality of the segmentation was assessed in two ways. Firstly, the mean nucleus spectrum was compared to the mean cytoplasm spectrum (Figure 6.2d). The most pronounced differences were associated with nucleic acid and lipid/fatty acid signals, with higher intensities found in the nucleus. Secondly, the size of the nucleus relative to the whole cell was assessed and compared with that from epifluorescence microscopy images of CH12F3 cells incubated with nucleic acid stains (Figure 6.2e). No statistically significant difference was found between the Raman and epifluorescence data. A larger variance was seen for the Raman data - possibly attributed to a number of smaller and kidney shaped nuclei (Figure 6.3f-g). These were not excluded as they were not outliers in the Raman spectral dataset.

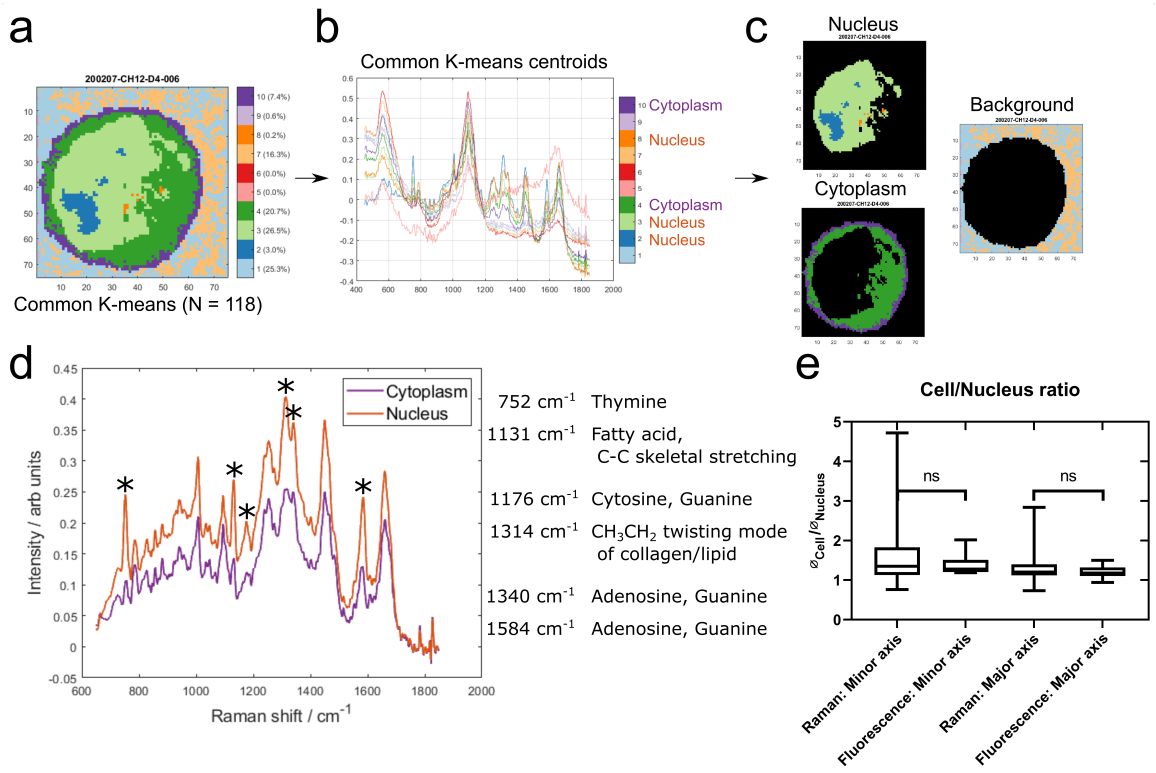

Figure 6.2.: *Identifying nucleus and cytoplasm associated areas using common K-means.* ***(a)*** *An example cell map (specifically sample 200207-CH12-D4-006) after common K-means with 10 clusters, which was used to analyse 118 individual cell maps concurrently.* ***(b)*** *The 10 common K-means centroid spectra. Spectral assignments were used to identify the clusters associated with cytoplasm (4 and 10) and nucleus (2, 3, and 8).* ***(c)*** *Example cell map (as seen in (a)) with nucleus (top left, cytoplasm (bottom left) and background (right) associated pixels highlighted.* ***(d)*** *Comparison of the mean cytoplasm and nucleus spectrum across all cells. The largest peak differences are highlighted and peak assignments are listed.* ***(e)*** *Comparison of nucleus/cell ratio between Raman maps and epifluorescence microscopy images.*

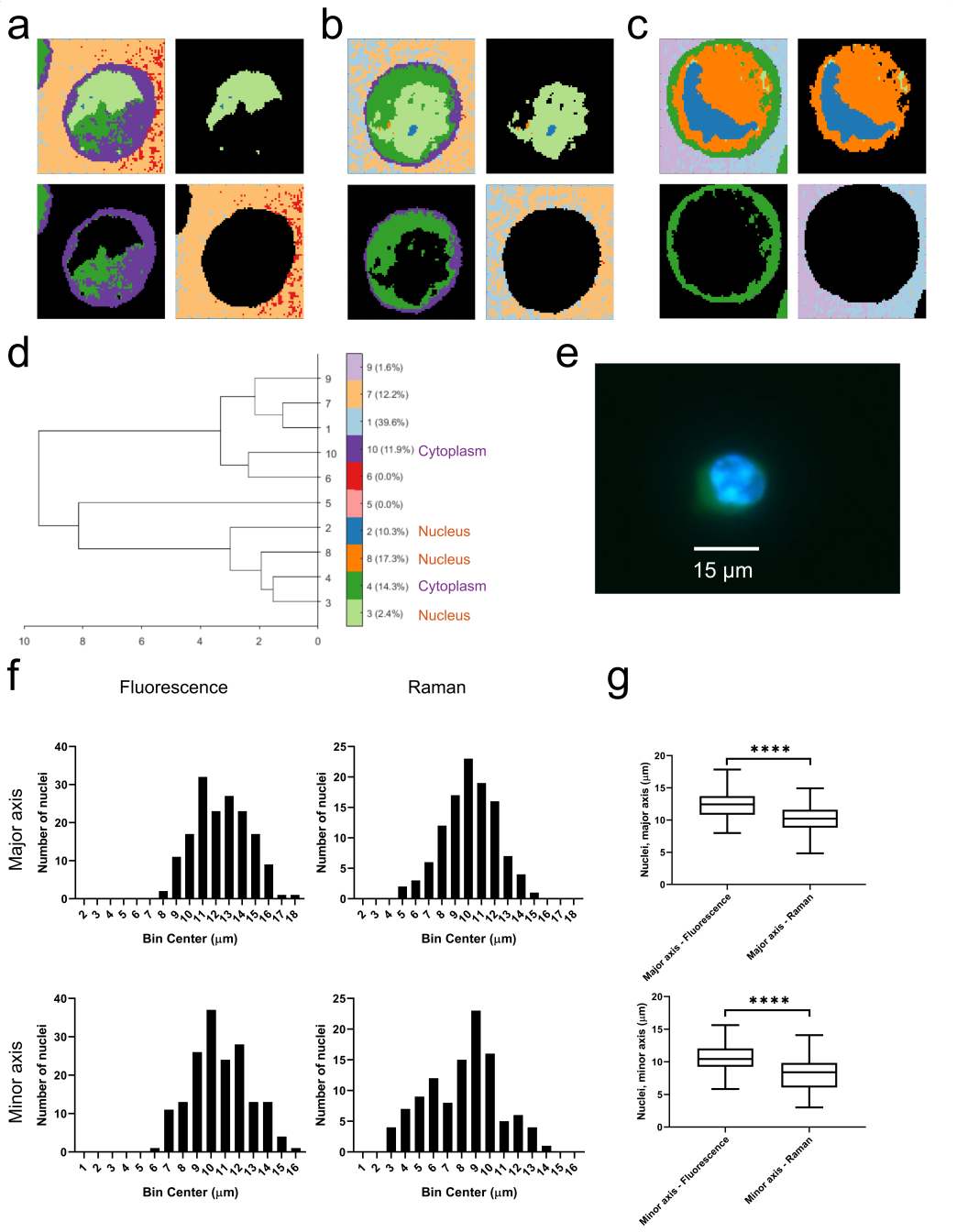

Figure 6.3.: *Assessing the cell and nucleus segmentation.*
(a-c) *Additional example cell maps (specifically samples 200114-CH12-D4-009 (a), 200212-CH12-D0-002 (b), and 200228-CH12-D0-007 (c)) after common K-means with 10 clusters, as presented in Figure 6.2a-c. Nucleus (top right), cytoplasm (bottom left), and background (bottom right) associated pixels highligted.* ***(d)*** *Hierarchical clustering analysis plot of the common K-means. The clusters idenfitied as cytoplasm and nucleus are annotated.* ***(e)*** *Epifluorescence image of a CH12F3 cell: the nucleus is stained with Hoechst (blue) and the whoel cell with SYTO13 (green).* ***(f)*** *Histograms showing the nucleus size distribution (major axis, left and minor axis, rigth) of the cells measured from Raman maps (top) and epifluorescence microscopy images (bottom).* ***(g)*** *Quantification of (b). A t-test gave a statistically significant difference between samples (ns.: $P>0.05$, $*$: $P \leq 0.05, **$: $P \leq 0.01, ***$: $P \leq 0.001$).*

6.2.1. Assessing the cell and nucleus segmentation

The additional cell map examples (Figure 6.3a-c) provide a clearer idea of how the cell and nucleus segmentation worked. Three clusters were determined to be associated with nucleus. The primary nucleus cluster varies between cell maps. That is also the case for the cytoplasm and background clusters. The Hierarchical Clustering Analysis (HCA) plot (Figure 6.3d) depicts the relationship between the ten clusters. All three nucleus clusters (2, 3, and 8) are similar to each other. One cytoplasm cluster (4) resembles the nucleus clusters, while the other one (10) is more similar to the background clusters. The ten clusters were assigned to either nucleus, cytoplasm or background based on the centroid spectra (Figure 6.2b), the HCA plot, and their effect on the cell and nucleus segmentation within each cell map. The cell versus background segmentation was straight forward, as seen in both the example maps and centroid spectra. Nucleus versus cytoplasm segmentation was based on peaks associated with nucleic acid, which is more abundant in the nucleus. Cluster 4 proved to be the most difficult to assign - it was found to be at the interface between nucleus and cytoplasm, as shown by the example maps and HCA plot (Figure 6.3a-d). The assignment of cluster 4 to cytoplasm was based on the centroid spectrum and the resulting nucleus size distribution of all maps.

The size and shape of the nuclei vary between maps, as seen in Figure 6.2c and Figure 6.3a-c. This variation was quantified and assessed by measuring the major and minor axes of each nucleus and comparing them to those derived from epifluorescence images Figure 6.3e-g). For both major and minor axes, the Raman mapped nuclei were smaller than the epifluorescence images nuclei. As both the measurement techniques and experimental setup were different between the two, this was not of great concern. Indeed, the Cell/Nucleus ratio was similar between the Raman maps and epifluorescence images (Figure 6.2e).

6.3. Quantifiable spectral differences between non-activated and activated B cells

To assess large-scale chromatin conformational and transcriptomic alterations, two groups of CH12F3 cells were compared: non-activated cells (D0) and cells at 96 hours post immune activation with cytokine (CIT: anti-CD40, IL-4, and TGFβ) cocktail (D4), as shown in Figure 6.4a. The immune activation of the cells was verified by

quantifying the percentage of IgM-producing cells versus IgA-producing cells using flow cytometry (Figure 6.6).

A prerequisite for further analysis and correlation with the transcriptomes was the ability to separate D0 and D4 cells based on their Raman spectra. Focusing on the nucleus, a number of spectral differences are apparent between D0 and D4 cells (Figure 6.4b). Namely, a peak at 786 cm^{-1} shows a large variation between the two activation states. The neighbouring peak at 752 cm^{-1} does not show this variation. Both of these peak are associated with nucleic acid[201–203]. The distribution of the 752 cm^{-1}-to-786 cm^{-1} peak ratios was found to be significantly different between D0 and D4 cells (Figure 6.4c). This nucleic acid peak ratio therefore has the potential to provide a measure of activation status through the measurement of change to DNA structure and environment within the cells.

To further explore the spectral differences between D0 and D4 cells, multivariate approaches were applied. An unsupervised method, Principal Component Analysis (PCA), showed a separation between D0 and D4 cells (Figure 6.4d-e and Figure 6.5a-c). Four PCs had a statistically significant difference between D0 and D4 scores. The loading spectra of those showed a range of peaks associated with both nucleic acid, lipid and protein (Figure 6.5d-g). Nucleic acid peaks around 786 cm^{-1} (PC1) and 752 cm^{-1} (PC1, PC4, and PC5) were amongst these, supporting the use of that peak ratio to distinguish between D0 and D4. Although a number of other nucleic acid peaks were identified, it is clear that intracellular changes of proteins and lipids are also drivers for the spectral differences.

A supervised method, Linear Discriminant Analysis (LDA) was then applied, building on the PC scores and determining a classifier to discriminate between D0 and D4 cells. The two groups showed a very good separation (Figure 6.4f). Using leave-one-out analysis, it was determined that the LDA classifier had a sensitivity of 73.1% and a specificity of 81.1% for identification of D4 cells. The loading plot for the classifier, representing the spectral data separating D0 and D4 cells, consisted of a range of peaks (Figure 6.4g). Nucleic acid peaks in the 751-790 cm^{-1} range are again present. The largest peaks include nucleic acid, protein, sugar and lipid, such as guanine and cytosine (782 cm^{-1}, 1251 cm^{-1}, 1577 cm^{-1})[204, 205], phosphodiester (812 cm^{-1}, 897 cm^{-1}, 1424 cm^{-1})[205], tryptophan (754 cm^{-1}, 761 cm^{-1}, 880 cm^{-1})[204, 206–209], polysaccharide structure and glucose (841 cm^{-1}, 1117 cm^{-1})[203, 210, 211] and CH_2 deformation (1304 cm^{-1}, 1321 cm^{-1})[203, 212].

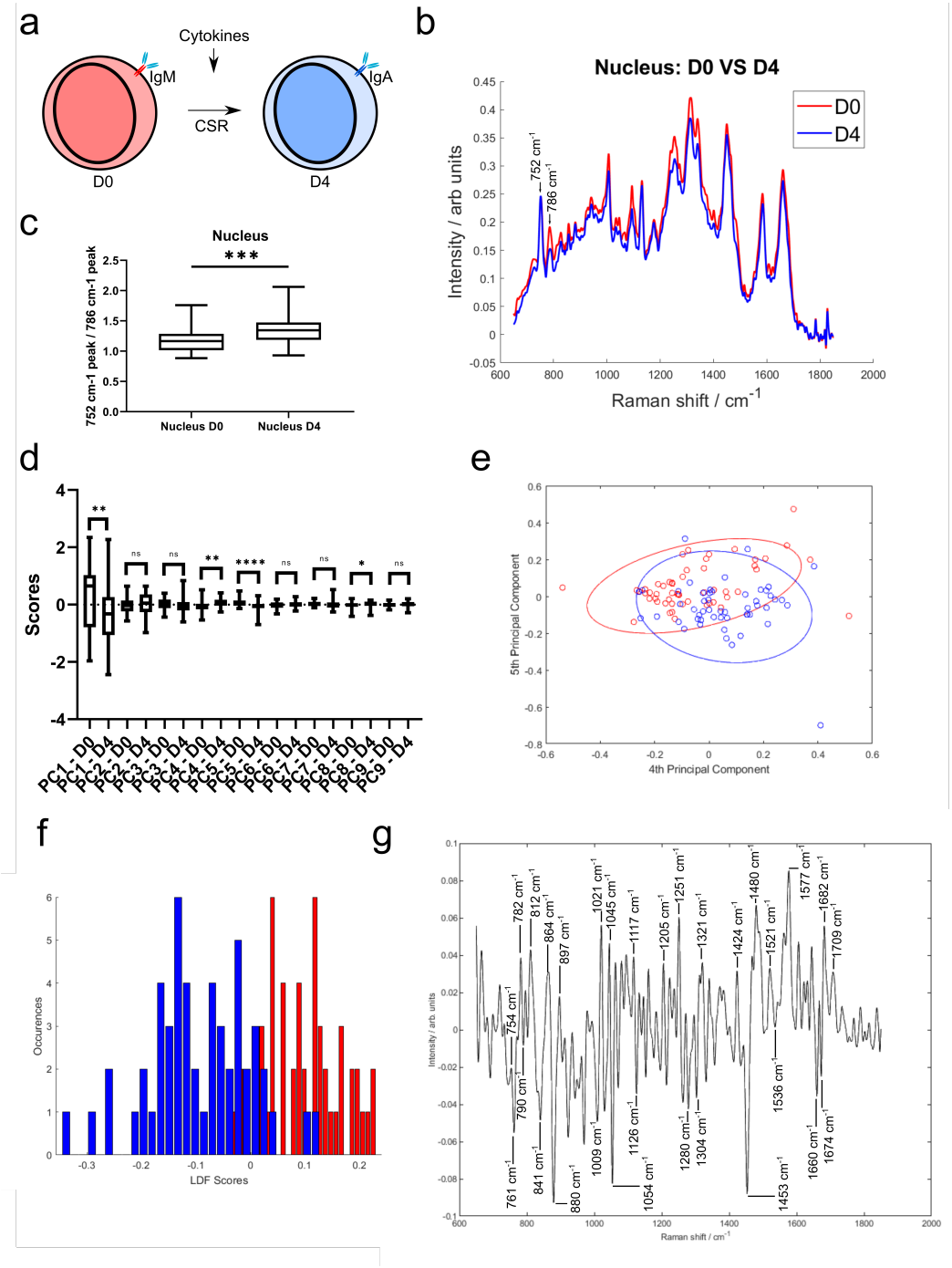

Figure 6.4.: *Quantifiable spectral differences between D0 and D4 cells.*
(a) *Schematic representation of a CH12F3 cell undergoing class switch recombination in response to exposure to the cytokine cocktail. The expressed B cell receptor constant region changes from IgM to IgA.* ***(b)*** *The mean nucleus spectrum of D0 and D4 cells. Two neighbouring peaks are highlighted.* ***(c)*** *Peak ratio (752 cm^{-1} peak/786 cm^{-1} peak). A t-test gave a statistically significant difference between samples (ns.: $P>0.05$, $*$: $P\leq0.05$, $**$: $P\leq0.01$, $***$:$P\leq0.001$).* ***(d)*** *Principal Component analysis. Comparison of the first 9 PC scores. A t-test was applied to identify the principal components with a statistically significant difference between D0 and D4.* ***(e)*** *PCA analysis. Scores plotted for components 4 and 5. 90 percent confidence intervals indicated.* ***(f)*** *LDA analysis. Histogram of the distribution in the training model.* ***(g)*** *LDA analysis. Loading spectrum.*

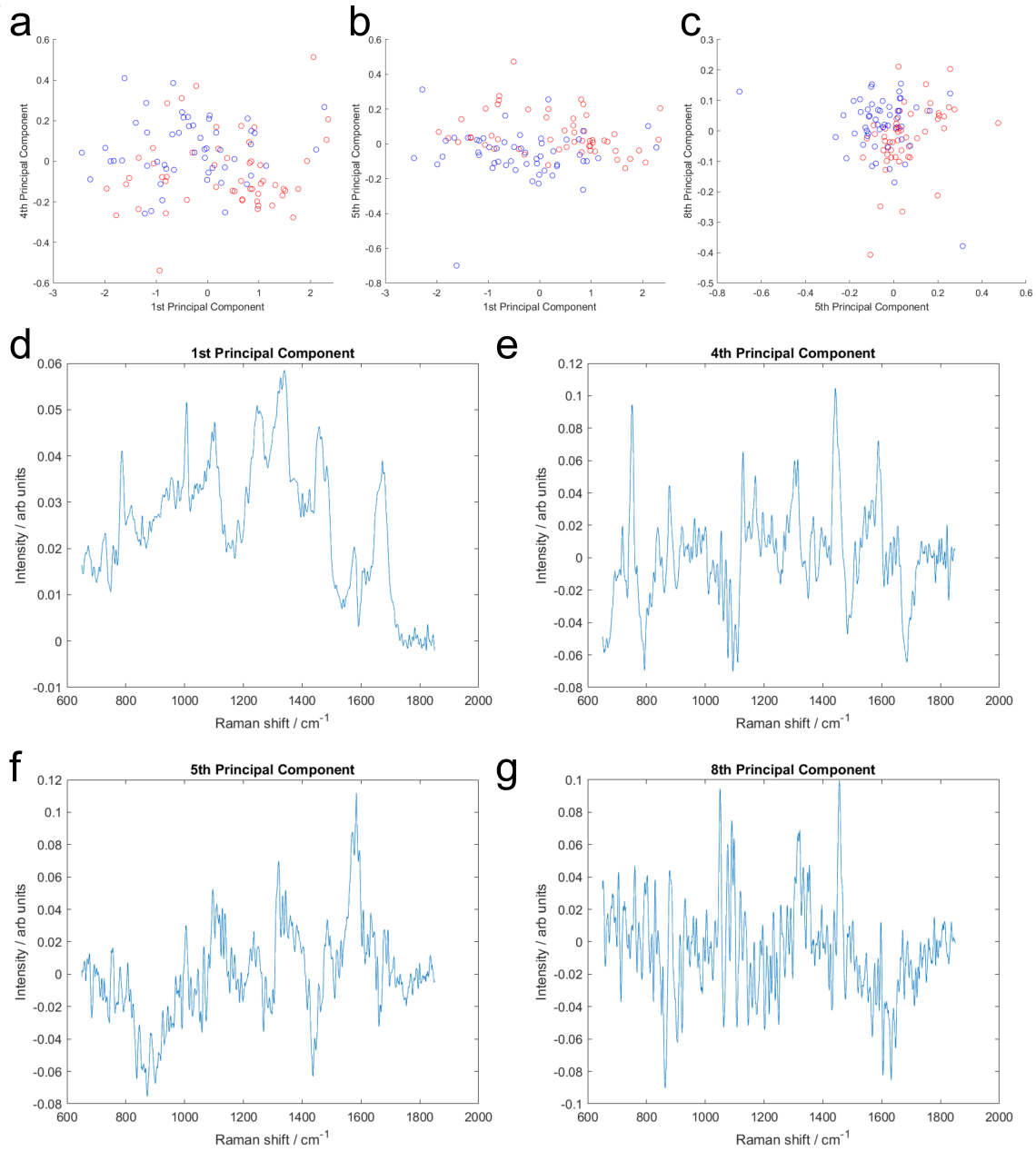

Figure 6.5.: *PCA and LDA analysis for discrimination between D0 and D4 cells.* ***(a)*** *PCA scores; PC1 versus PC4.* ***(b)*** *PCA scores; PC1 versus PC5.* ***(c)*** *PCA scores; PC5 versus PC8.* ***(d)*** *PCA loadings; PC1.* ***(e)*** *PCA loadings; PC4.* ***(f)*** *PCA loadings; PC5.* ***(g)*** *PCA loadings; PC8.*

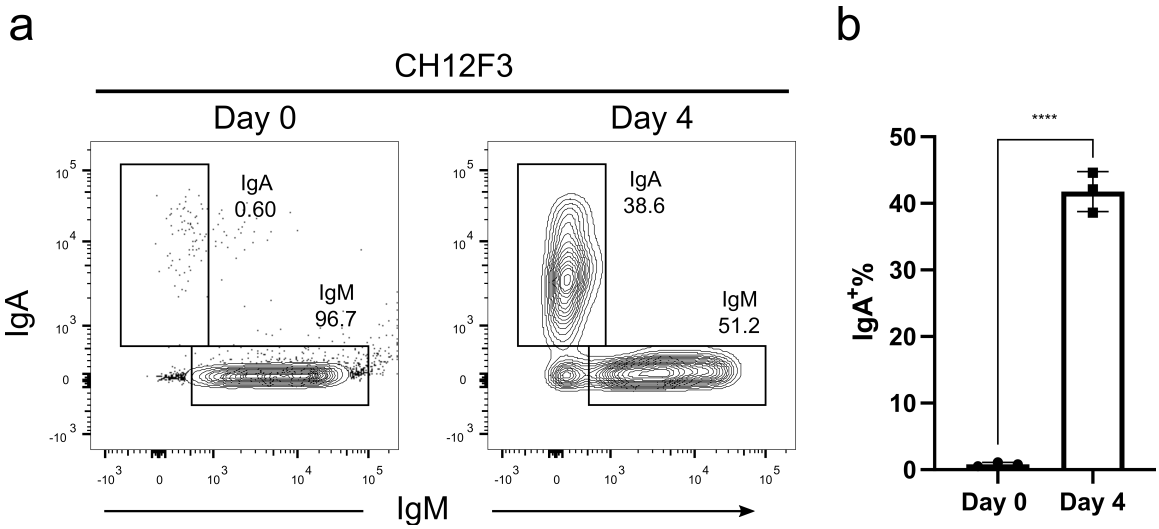

Figure 6.6.: *Monitoring CSR in CH12F3 cells.*
(a) *CSR in CH12F3 upon CIT stimulation monitored by identifying IgM- and IgA producing cells using flow cytometry.* ***(b)*** *Quantification of IgA+ cells for D0 and D4.*

6.4. Differing transcriptomic profiles of non-activated and activated B cells

The transcriptomic profiles of D0 and D4 cells were determined and analysed. Read counts were measured for a total of 17,725 transcripts, and differential gene expression analysis using DESeq2 was applied to identify genes that were up- or down-regulated in response to immune activation. Figure 6.7a shows transcripts with the largest change of expression between D0 and D4 samples, clustered based on Euclidean distance. The two transcripts *Ighm* and *Igha*, which code for the immunoglobulin heavy chain constant regions of IgM and IgA, respectively, are highlighted. *Ighm* expression is down-regulated in D4, while *Igha* is up-regulated. This is a hallmark of the CH12F3 class switching response and in agreement with the IgM to IgA isotype switching measured by flow cytometry (Figure 6.6).

The expression profiles of D0 and D4 cell samples clearly illustrate that several thousands of genes are up- or down-regulated upon immune activation of CH12F3 cells. These data are in line with published results regarding genes that are over-expressed during B cell maturation[213]. For example, we could identify that genes AID, Bcl11a, CD40, and Ccr6 go up 1-, 3-, 2.6-, and 8.7-fold in D4 compared to D0, respectively. This further illustrates the validity of our RNA-seq results. Further whole transcriptomic profiling, including PCA analysis (Figure 6.7b) and network comparison

(Figure 6.7c), demonstrated a clear separation between D0 and D4 samples and the validity of our experimental approach.

PCA analysis on the expression profiles of D0 and D4 CH12F3 cohort samples were performed using Clustvis software[164]. Differences were assessed after $\log_2$ transformation of normalised read counts at a threshold of $p<0.05$ for multiple comparisons. The variation in expression profile between D0 and D4 CH12F3 samples was displayed in first and second dimensions (PC1 vs PC2). Statistical significance was set at false discovery rate (FDR)<0.05. As a result, we could observe that the thee D0 samples cluster in proximity together, as do the three D4 samples. But the D0 versus D4 clustered markedly separately from each other when plotted on the same graph (Figure 6.7b). This further validates the distinction in overall transcriptional profile of our cohorts. To further identify the specific bases for this distinction, Genemania pathway analysis tool[214] was used. After including all hits in D4 expressed at $\log_2$ fold change >1 with FDR<0.05, the top pathways were identified to include the chemokine signalling pathway, leukocyte activation, immune cell differentiation, and B cell activation amongst other B cell related processes (Figure 6.7c). This further validates the specificity and consistency of the experimental design.

6.5. Linear correlation between transcriptomic and Raman data

Alterations in gene expression can ultimately cause changes in intracellular protein levels, as well as in other biomolecules through changes to metabolic pathways and intracellular structures. All these changes are bound to affect Raman spectral readouts. That a correlation exists between transcriptomic data and Raman spetra, as demonstrated for yeast and bacteria[102], is therefore not unexpected, albeit it was hard to predict whether a linear correlation would exist in a complex mammalian cell such as a B lymphocyte.

To test this hypothesis, a Partial Least Squares (PLS) regression analysis was applied to create a model for the prediction of Raman data from transcriptomic data of CH12F3 cells. A PLS regression model was determined from three D0 samples (D0-1, D0-2, D0-3) and three D4 samples (D4-1, D4-2, D4-3) of transcriptomic and Raman data (Figure 6.8a and Figure 6.9a).

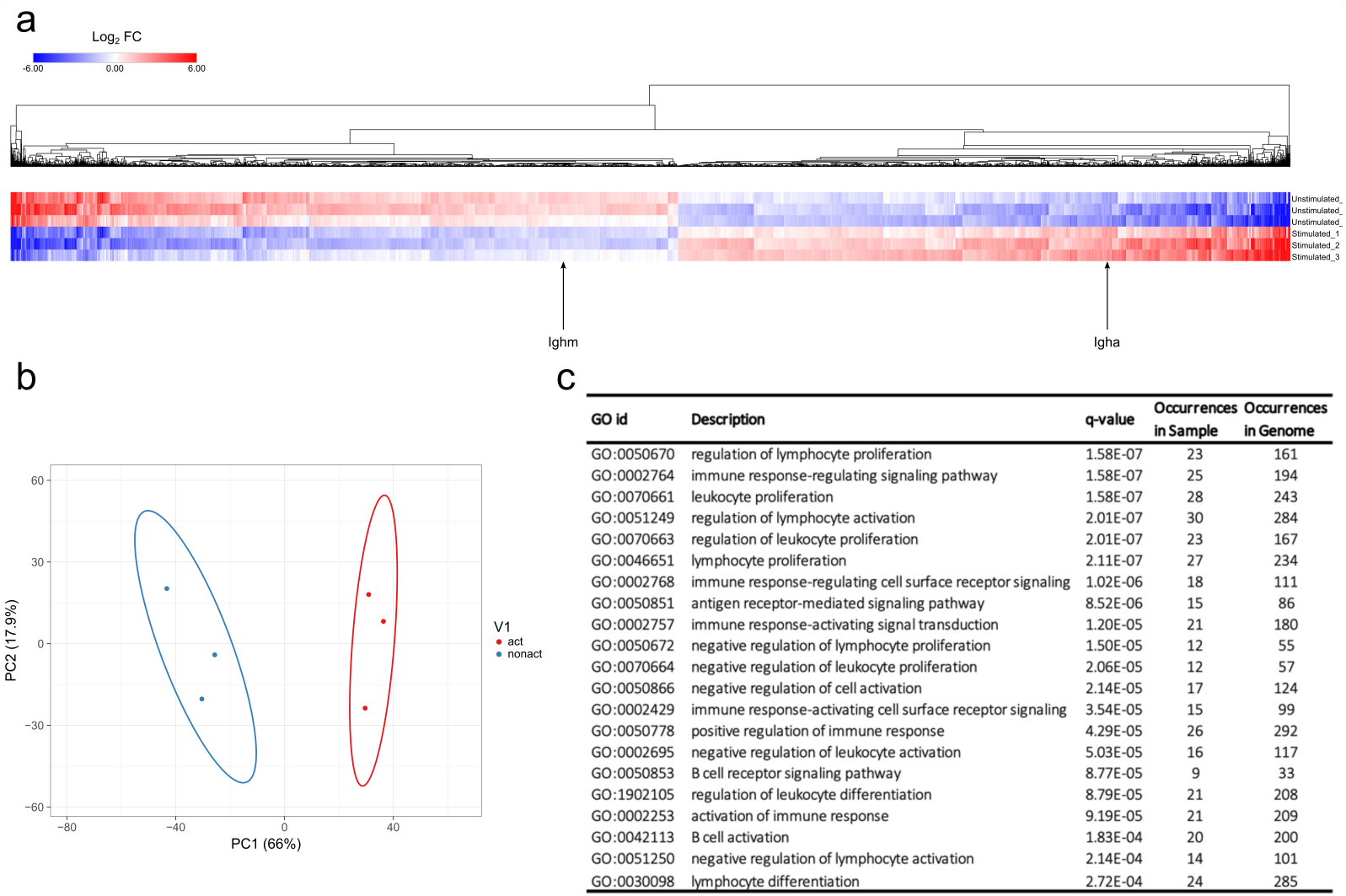

GO id	Description	q-value	Occurrences in Sample	Occurrences in Genome
GO:0050670	regulation of lymphocyte proliferation	1.58E-07	23	161
GO:0002764	immune response-regulating signaling pathway	1.58E-07	25	194
GO:0070661	leukocyte proliferation	1.58E-07	28	243
GO:0051249	regulation of lymphocyte activation	2.01E-07	30	284
GO:0070663	regulation of leukocyte proliferation	2.01E-07	23	167
GO:0046651	lymphocyte proliferation	2.11E-07	27	234
GO:0002768	immune response-regulating cell surface receptor signaling	1.02E-06	18	111
GO:0050851	antigen receptor-mediated signaling pathway	8.52E-06	15	86
GO:0002757	immune response-activating signal transduction	1.20E-05	21	180
GO:0050672	negative regulation of lymphocyte proliferation	1.50E-05	12	55
GO:0070664	negative regulation of leukocyte proliferation	2.06E-05	12	57
GO:0050866	negative regulation of cell activation	2.14E-05	17	124
GO:0002429	immune response-activating cell surface receptor signaling	3.54E-05	15	99
GO:0050778	positive regulation of immune response	4.29E-05	26	292
GO:0002695	negative regulation of leukocyte activation	5.03E-05	16	117
GO:0050853	B cell receptor signaling pathway	8.77E-05	9	33
GO:1902105	regulation of leukocyte differentiation	8.79E-05	21	208
GO:0002253	activation of immune response	9.19E-05	21	209
GO:0042113	B cell activation	1.83E-04	20	200
GO:0051250	negative regulation of lymphocyte activation	2.14E-04	14	101
GO:0030098	lymphocyte differentiation	2.72E-04	24	285

Figure 6.7.: *Transcriptomes of D0 and D4 cells.*
(a) *Heatmap of the log2 fold change of transcripts from D0 and D4 samples, calculated using the DESeq2 software. Transcripts with $|log_2$ fold change$| > 0.5$ and FDR< 0.05 are shown. Two transcripts, Ighm and Igha, are highlighted. Ighm and Igha code for the immunoglobulin heavy chain constant regions of IgM and IgA receptors, respectively.* ***(b)*** *PCA analysis showing separation of D0 and D4 samples.* ***(c)*** *Functional enrichment analysis of differentially expressed transcripts between D0 and D4. Table displaying significantly enriched gene ontology (GO) terms and associated biological processes.*

Using a leave-one-out approach, the validity of the linear regression model was tested on each sample in turn; one sample, i, was left out, and a PLS regression coefficients matrix, $BETA_{-i}$, was determined from the remaining five samples. This matrix was then used to predict the Raman scores of the left-out sample.

$$R_{\text{predicted}} = BETA_{-i} \cdot T_i \tag{6.1}$$

To assess the validity of these predictions and thus the PLS regression model, the predicted Raman data were compared to the single cell D0 and D4 data for each sample. Plotting the predicted PC scores against the single cell scores shows D0-2 and D4-2 within their exprected regions (Figure 6.8b) and the rest around the intersection between D0 and D4 (Figure 6.9b-e). Further, by converting the predicted PC scores into their respective LDF scores, the predicted group membership (D0 or D4) could be assessed (Figure 6.8c). The three D0 samples are found within the D0 region, while the D4 samples are found within the D4 region.

These results show that a linear correlation exists between transcriptomic profiles and Raman spectra of CH12F3 cells. Specifically, the variation in transcript expression levels between D0 and D4 cells is reflected in variation in Raman spectra of D0 and D4 cells - and transcriptomic data can be used to predict Raman data of CH12F3 cells.

6.5.1. Predicting Raman data from transcriptomic data using PLS regression models

The linear correlation between Raman data and transcriptomic data, as determined by the PLS analysis, is visualised in Figure 6.9a for component 1. The D0 samples cluster together, as do the D4 samples. This is the basis for the model which enabled the prediction of Raman data from transcriptomic data (Figure 6.8b-c and Figure 6.9b-e).

In addition to the Raman nucleus data (Figure 6.8 and Figure 6.9), Raman whole cell and cytoplasm data were also used for PLS analysis (Figure 6.10). The whole cell data analysis results were largely identical to those of the nucleus data analysis (Figure 6.10a). For cytoplasm data, the results differed more. However, the linear correlation was still clear (Figure 6.10b), and it was still possible to accurately predict Raman data from transcriptomic data (Figure 6.10c-f).

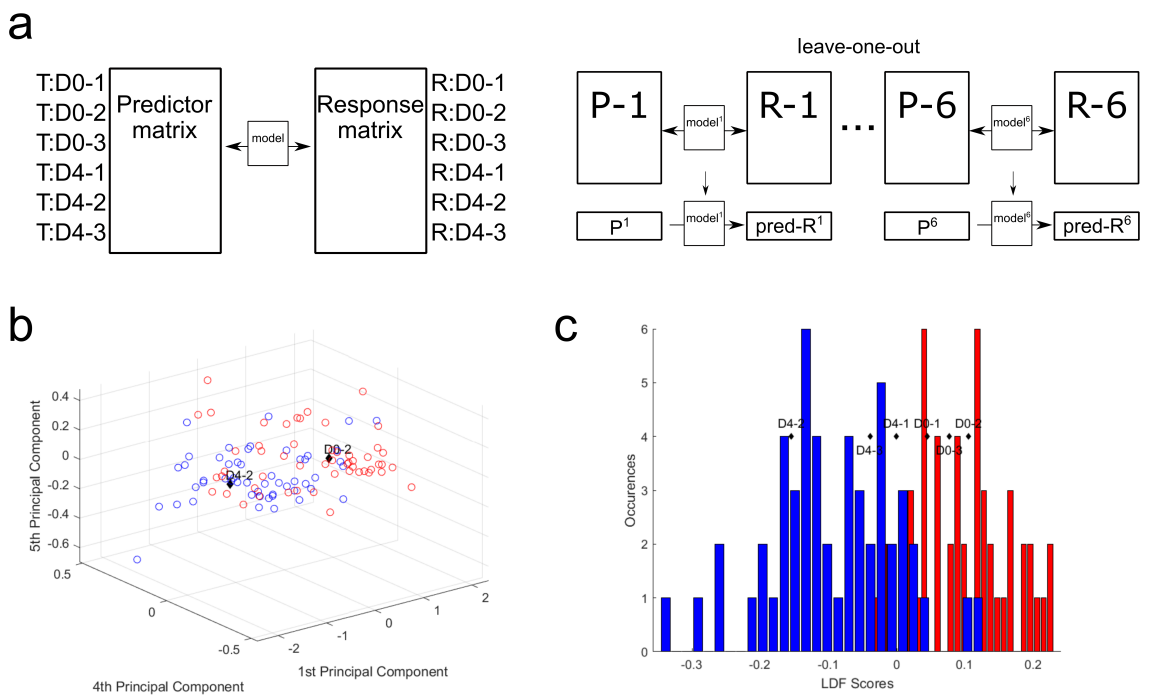

Figure 6.8.: *Partial least squares regression model correlates Raman and transcriptomic data.*
(a) *Partial least squares regresion model.* ***(b)*** *Raman scores predicted from transcriptomic read counts. Predicted D0-2 and D4-2 plotted with the single cell scores from PC1, PC4, and PC5.* ***(c)*** *Predicted Raman scores converted to LDA scores and plotted against the LDA scores histogram.*

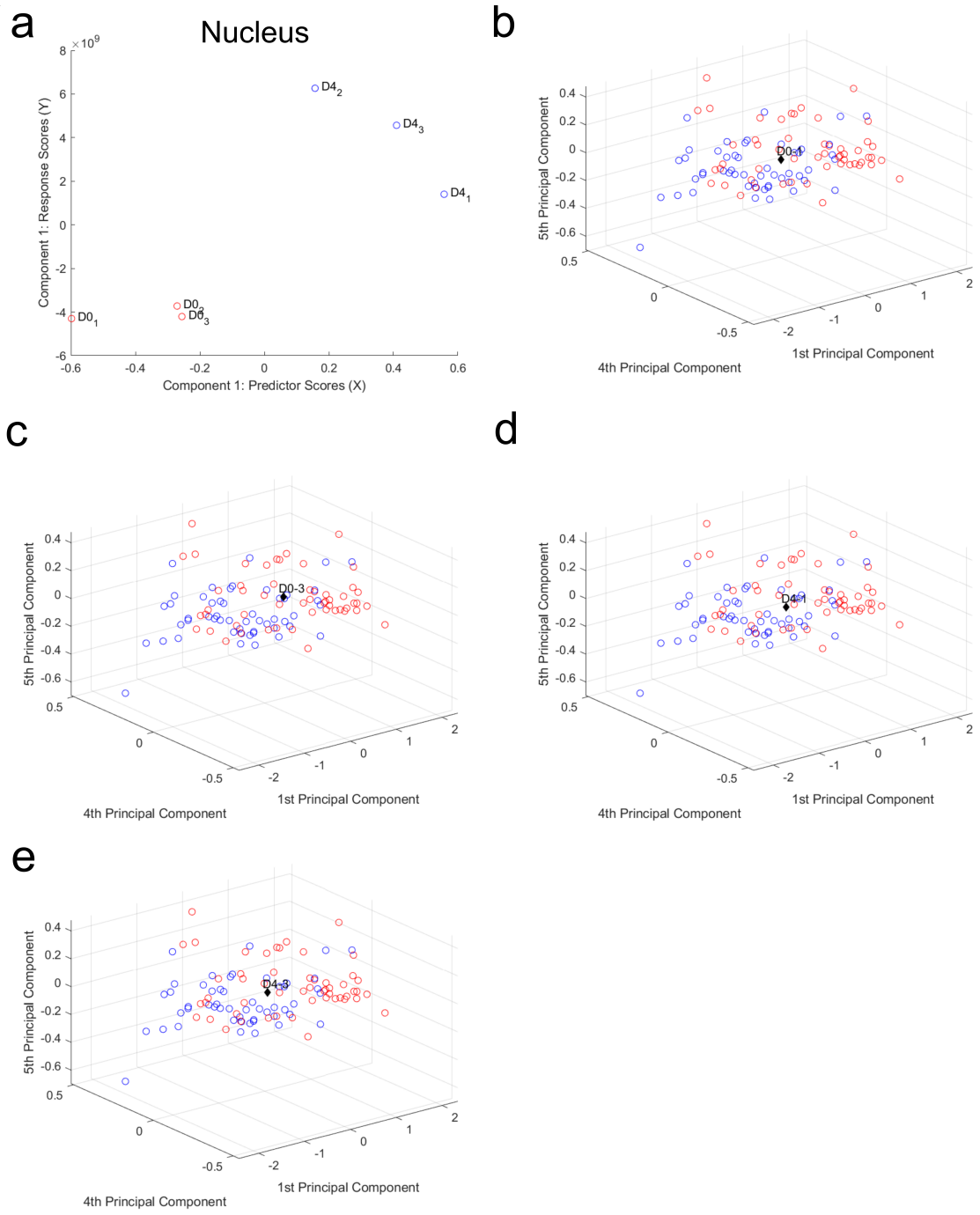

Figure 6.9.: *PLS regression model can predict Raman data from transcriptomic data.* ***(a)*** *PLS regression analysis shows a linear correlation between Raman nucleus data and transcriptomic data for component 1.* ***(b-e)*** *Raman scores predicted from transcriptomic read counts. D0-1 (b), D0-3 (c), D4-1 (d), and D4-3 (e) plotted with the single cell scores from PC1, PC4, and PC5.*

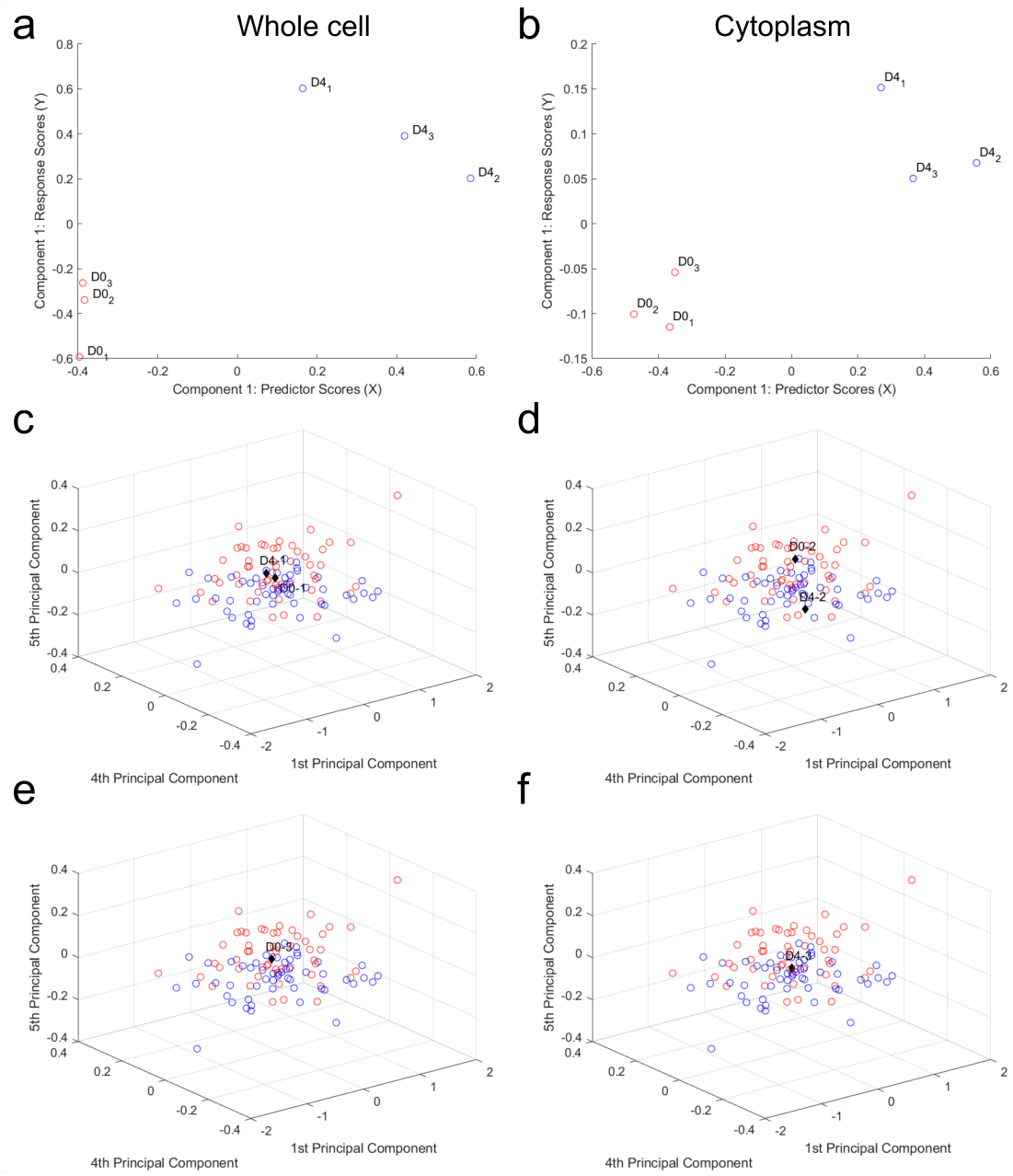

Figure 6.10.: *PLS regression model correlates Raman whole cell and cytoplasm data with transcriptomic data.*
(a) *PLS regression analysis shows a linear correlation between Raman whole cell data and transcriptomic data for component 1.* ***(b)*** *PLS regression analysis shows a linear correlation between Raman cytoplasm data and transcriptomic data for component 1..* ***(c-h)*** *Raman cytoplasm PLS model: Raman scores predicted from transcriptomic read counts. D0-1 and D4-1 (c), D0-2 and D4-2 (d), D0-3 (e), D4-3 (f) plotted with the single cell scores for PC1, PC4, and PC5.*

6.6. Identification of key transcripts for the correlation between Raman data and transcriptomic data

The importance of each transcript for the regression model is of particular interest, as this may reveal genes or pathways that are essential for the immune activation process. As shown in Figure 6.7, thousands of transcripts are differentially expressed between D0 and D4. However, translation levels, protein modifications, and other regulatory mechanisms add further complexity to the final biochemical composition of the cell. A transcriptional profile does not account for these additional layers of regulation. Identifying transcripts of high importance for the correlation with the intracellular biochemical changes as measured by Raman microscopy may therefore be of great value. The Variable Importance in Projection (VIP) score was determined for each transcript. The top 20 transcripts for the PLS regression are shown in Figure 6.11a. These hits were termed the VIP list. Upon further analyses of the protein coding entries in the VIP list, it was identified that many of the hits do indeed correlate with expression profiles from *in vivo* activated B cells isolated from murine germinal centre splenocytes (Figure 6.11b), and their expression quantifications (Figure 6.11c) correlate with post-activation B cell responses. It is worth noting that germinal centre splenocytes and CH12F3 cells are not directly comparable given the immortalised nature of the CH12F3 cell line. That is why the *in vivo* germinal centre B cell response was configured into three broad groups termed pre-, mid-, and post-activation (Figure 6.11b-c). Two representative *in vivo* cohorts were taken for each of these broad groups as represented in Figure 6.11b to ensure maximum congruency between *ex vivo* and *in vivo* analyses.

Ighm and *Igha* are both found in the top four gene hits (Figure 6.11a). Although their change in expression levels results in the isotype switching from IgM to IgA, it is worth noting that they by no means are the most differentially expressed genes (Figure 6.7). Their high importance for the correlation with the Raman data therefore underlines that the transcripts with the highest fold change are not necessarily the most informative of the changing biochemical composition of a cell. The importance of IgM and IgA expression in the immune activation process is obvious, and their high presence on the VIP list supports the validity of the PLS regression model. Additional transcripts in the top 20 include regulatory and ribosomal RNAs, which is in line with data from yeast and bacterial analysis[102]. A large number of regulatory proteins are also on the list, including a number of heat shock proteins, which have previously been shown to be important for CSR[215]. Actin is also high on the list, in

a

VIP score	Transcript name	Transcript type	Gene name	
42.54684	ENSMUSG00000064339	Mt_rRNA	mt-Rnr2	mitochondrially encoded 16S rRNA
35.21075	ENSMUSG00000092341	lncRNA	Malat1	metastasis associated lung adenocarcinoma transcript 1
31.19724	ENSMUSG00000095079	IG_C_gene	Igha	immunoglobulin heavy constant alpha
29.12567	ENSMUSG00000076617	IG_C_gene	Ighm	immunoglobulin heavy constant mu
28.97717	ENSMUSG00000037742	protein_coding	Eef1a1	Elongation factor 1-alpha 1
27.09382	ENSMUSG00000029580	protein_coding	Actb	actin, beta
24.65058	ENSMUSG00000065037	misc_RNA	Rn7sk	RNA, 7SK, nuclear
24.38713	ENSMUSG00000097971	lncRNA	Gm26917	predicted gene, 26917
21.2204	ENSMUSG00000064351	protein_coding	mt-Co1	mitochondrially encoded cytochrome c oxidase I
20.35244	ENSMUSG00000047139	protein_coding	Cd24a	CD24a antigen
18.47201	ENSMUSG00000034994	protein_coding	Eef2	eukaryotic translation elongation factor 2
14.85389	ENSMUSG00000031779	protein_coding	Ccl22	chemokine (C-C motif) ligand 22
14.37985	ENSMUSG00000011179	protein_coding	Odc1	ornithine decarboxylase, structural 1
13.17376	ENSMUSG00000026864	protein_coding	Hspa5	heat shock protein 5
13.09707	ENSMUSG00000015656	protein_coding	Hspa8	heat shock protein 8
12.81861	ENSMUSG00000032399	protein_coding	Rpl4	60S ribosomal protein L4
10.87438	ENSMUSG00000049775	protein_coding	Tmsb4x	thymosin, beta 4, X chromosome
10.64323	ENSMUSG00000024359	protein_coding	Hspa9	heat shock protein 9
10.40896	ENSMUSG00000022797	protein_coding	Tfrc	transferrin receptor
10.36869	ENSMUSG00000020048	protein_coding	Hsp90b1	heat shock protein 90, beta (Grp94), member 1

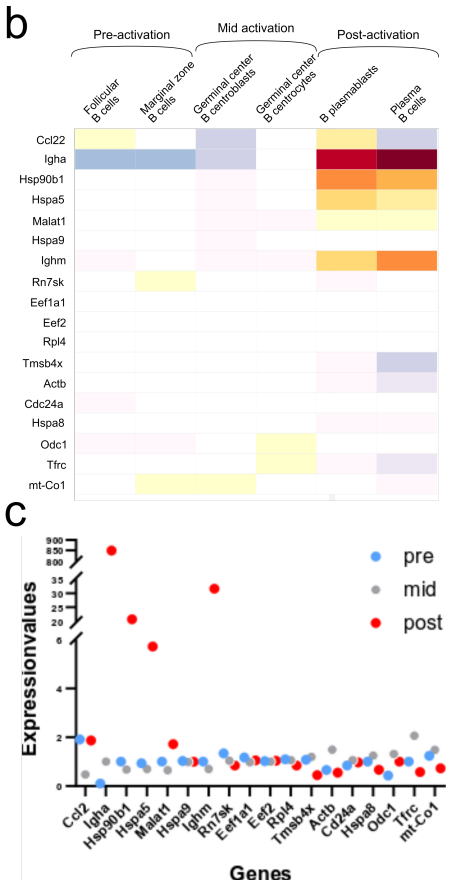

Figure 6.11.: *VIP transcript list and their expression ex vivo.*
(a) *The 20 transcripts with the highest Variable Importance in Projection (VIP) scores.* ***(b)*** *Expression of VIP genes in vivo. Median normalised gene expression values in different B cell subsets in vivo as annotated in Immunological Genome Projects. Further subclassified into pre-, mid-, and post-activation correlating to activation for CSR in CH12F3.* ***(c)*** *Quantification of normalised expression values of VIP genes in the dot plot.*

agreement with studies showing a regulatory role of the actin cytoskeleton in B cell activation[216, 217], as well as possibly the role of monomeric actin in DNA damage response (DDR) and chromatin modifications which happen during cell development and DNA repair[218–220].

A PLS regression model was also determined for whole cell and cytoplasm Raman data (Figure 6.10a-b). These allowed for predictions in line with the nucleus data (cytoplasm shown in Figure 6.10c-f). The top 20 VIP transcripts for those models (Table 6.1 and Table 6.2) were largely identical to the nucleus list. The values and order of the transcripts varied slightly, but only one transcript differed between the nucleus and whole cell list. For cytoplasm compared to nucleus, only three transcripts were different in the top 20 hits.

VIP score	Transcript name	Transcript type	Gene name	
41.68459	ENSMUSG00000064339	Mt_rRNA	mt-Rnr2	mitochondrially encoded 16S rRNA
31.63403	ENSMUSG00000037742	protein_coding	Eef1a1	Elongation factor 1-alpha 1
30.71642	ENSMUSG00000095079	IG_C_gene	Igha	immunoglobulin heavy constant alpha
30.42896	ENSMUSG00000092341	lncRNA	Malat1	metastasis associated lung adenocarcinoma transcript 1
29.63411	ENSMUSG00000076617	IG_C_gene	Ighm	immunoglobulin heavy constant mu
28.14179	ENSMUSG00000029580	protein_coding	Actb	actin, beta
23.71356	ENSMUSG00000097971	lncRNA	Gm26917	predicted gene, 26917
23.70888	ENSMUSG00000065037	misc_RNA	Rn7sk	RNA, 7SK, nuclear
22.0795	ENSMUSG00000064351	protein_coding	mt-Co1	mitochondrially encoded cytochrome c oxidase I
20.93438	ENSMUSG00000047139	protein_coding	Cd24a	CD24a antigen
20.11123	ENSMUSG00000034994	protein_coding	Eef2	eukaryotic translation elongation factor 2
15.38487	ENSMUSG00000011179	protein_coding	Odc1	ornithine decarboxylase, structural 1
14.87474	ENSMUSG00000031779	protein_coding	Ccl22	chemokine (C-C motif) ligand 22
14.05003	ENSMUSG00000032399	protein_coding	Rpl4	60S ribosomal protein L4
13.63799	ENSMUSG00000015656	protein_coding	Hspa8	heat shock protein 8
11.70491	ENSMUSG00000026864	protein_coding	Hspa5	heat shock protein 5
11.58428	ENSMUSG00000049775	protein_coding	Tmsb4x	thymosin, beta 4, X chromosome
11.54382	ENSMUSG00000024359	protein_coding	Hspa9	heat shock protein 9
10.83353	ENSMUSG00000057113	protein_coding	Npm1	Nucleophosmin
10.81621	ENSMUSG00000022797	protein_coding	Tfrc	transferrin receptor

Table 6.1.: *VIP list for Whole cell Raman data PLS regression analysis.*

VIP score	Transcript name	Transcript type	Gene name	
36.48182	ENSMUSG00000037742	protein_coding	Eef1a1	Elongation factor 1-alpha 1
36.38903	ENSMUSG00000064339	Mt_rRNA	mt-Rnr2	mitochondrially encoded 16S rRNA
34.47657	ENSMUSG00000076617	IG_C_gene	Ighm	immunoglobulin heavy constant mu
27.54574	ENSMUSG00000095079	IG_C_gene	Igha	immunoglobulin heavy constant alpha
27.18289	ENSMUSG00000097971	lncRNA	Gm26917	predicted gene, 26917
27.03748	ENSMUSG00000029580	protein_coding	Actb	actin, beta
24.54971	ENSMUSG00000065037	misc_RNA	Rn7sk	RNA, 7SK, nuclear
24.41311	ENSMUSG00000064351	protein_coding	mt-Co1	mitochondrially encoded cytochrome c oxidase I
24.35519	ENSMUSG00000092341	lncRNA	Malat1	metastasis associated lung adenocarcinoma transcript 1
21.69827	ENSMUSG00000034994	protein_coding	Eef2	eukaryotic translation elongation factor 2
19.10295	ENSMUSG00000047139	protein_coding	Cd24a	CD24a antigen
15.70651	ENSMUSG00000032399	protein_coding	Rpl4	60S ribosomal protein L4
15.32205	ENSMUSG00000011179	protein_coding	Odc1	ornithine decarboxylase, structural 1
13.15234	ENSMUSG00000031779	protein_coding	Ccl22	chemokine (C-C motif) ligand 22
12.79875	ENSMUSG00000057113	protein_coding	Npm1	Nucleophosmin
12.78879	ENSMUSG00000015656	protein_coding	Hspa8	heat shock protein 8
12.50920	ENSMUSG00000058655	protein_coding	Eif4b	Eukaryotic translation initiation factor 4B
12.18672	ENSMUSG00000024359	protein_coding	Hspa9	heat shock protein 9
10.85725	ENSMUSG00000049775	protein_coding	Tmsb4x	thymosin, beta 4, X chromosome
10.57061	ENSMUSG00000051506	protein_coding	Wdfy4	WD repeat and FYVE domain containing 4

Table 6.2.: *VIP list for Cytoplasm Raman data PLS regression analysis.*

6.7. Conclusion

6.7.1. The 752/786 cm^{-1} peak ratio

The cell segmentation used to isolate nucleus and cytoplasm regions within each cell using the Raman spectral maps proved useful for highlighting DNA Raman peaks. The 752/786 cm^{-1} peak ratio, shown to be statistically different between between D0 and D4, has potential as a measure of activation status. If it is to be used as such, the biological significance of this peak ratio is of interest. The structure of DNA likely plays a role here. There are three biologically relevant double helical structures of DNA: A-DNA, B-DNA, and Z-DNA. B-DNA is the most common. A Raman peak at 784-787 cm_1 has been shown to have a strong intensity for B-DNA, but much lower the other two. The peak consists of two subpeaks; the breathing mode of the cytosine ring and the phosphodiester symmetric stretch of B-DNA backbone[201, 221]. During B to Z transition of DNA, the phosphodiester symmetric stretch signal downshifts[201]. As Z-DNA is associated with the rate of transcription[222, 223], it is plausible that the restructuring of DNA during activation could account for the difference between D0 and D4.

6.7.2. A linear correlation exists between Raman data and transcriptomic data

Both the PCA and LDA analysis revealed a myriad of spectral differences that allowed for the classification of D0 versus D4 cells. These included a large number of nucleic acid associated peaks, but also protein, lipid and sugar peaks. Classification of cell types or cell states based on Raman spectra has great clinical and research potential. However, understanding the biological significance of the spectral changes is of importance if these tools are to be implemented as a standard technique in biological laboratories. Peak assignments based on single molecule measurements provide some help with interpretation of the spectral changes. Correlation with transcriptomic data and identification of top VIP transcripts could add further value to the Raman data.

Here, it was shown that a linear correlation between Raman data and conventional transcriptomic data exists in CH12F3 cells. Raman data were predicted based on transcriptomic profiles. When comparing the predicted Raman data to single cell data, the classification of each prediction was within the expected groups (D0 vs D4). The analysis also identified the transcripts with the highest importance for the

correlation with Raman spectra of non-activated and activated CH12F3 cells (Figure 6.11a). The immunoglobulin genes *Ighm* and *Igha* both featured in the top hits, highlighting the value of the PLS regression model as a valid phenotypic measurement of B cell activation. A number of regulatory RNAs and proteins were also in the top 20, some known to be involved in the regulation of CSR and activation, and others not previously shown to be involved. Further experiments exploring the role of these transcripts in B cell activation and CSR could be of great interest in the field of adaptive humoral immunity.

7. Discussion and Conclusions

The following chapter contains sections of the papers "Single Cell Imaging of Nuclear Architecture Changes"[1], and "Single Cell Label-free Probing of Chromatin Dynamics during B Lymphocyte Maturation"[2].

In this thesis, I explored novel techniques for assessing chromatin and transcriptional changes, as well as nuclear mechanical properties during B cell activation. FTIR imaging and Raman mapping of single cells enabled label-free monitoring of chromatin conformation and other intracellular biochemical changes in response to immune and transcriptional activation. Deformability cytometry enabled assessment of mechanical properties of the nucleus, namely nuclear auxeticity. Together these biochemical and mechanical nuclear properties were identified as key markers with a potential use for phenotypic characterisation of single cells.

A number of other molecular biology techniques are in use for chromatin studies. These include chromatin immunoprecipitation sequencing (ChIP-seq), which is used to analyse interactions between protein and DNA, and Hi-C, which is used to analyse chromatin organisation. Vibrational spectroscopy may provide complementary information to these techniques by quantifying biochemical and structural changes of chromatin. While the resolution is not at a sequencing level, the label-free and non-invasive nature of the techniques make them well suited for simultaneous or sequential analysis with other techniques. Further, correlation between vibrational spectroscopy data and transcriptomic data has the potential to refine the biological interpretations of the spectral data.

7.1. Mechanical signalling and chromatin

A correlation between chromatin decondensation and nuclear auxeticity was shown in B cells (chapter 4). This was in agreement with previous work on embryonic stem (ES) cells[124]. The correlation with chromatin condensation state presents nuclear

auxeticity as a potential factor in mechanical signalling, known as mechanotranduction. The biological mechanisms behind this mechanical property are still to be investigated.

7.1.1. Biological mechanisms of nuclear auxeticity

Despite the lack of a conclusive biological mechanism for the observations, it could be postulated that the link between the pertubations in chromatin architecture initiated by TSA or CIT treatment and the observed nuclear auxeticity could either be due to: 1) a passive conformational change whereby the chromatin decondensation created by transcriptional activation or B cell maturation causes an increase in nuclear volume via increase in fluid influx; and/or 2) an active conformational change resulting from the tight crosstalk between cytoskeletal and chromatin architecture which has been well documented so far[15, 20, 190, 224–227]. It has been shown that increased nuclear membrane tension can alter nuclear pore complex (NPC) permeability. NPCs are known to undergo conformational changes to constrict or dilate the NPC in response to mechanical forces[228–230]. Most of these signalling cascades are mediated by nuclear membrane proteins known as lamins. Lamin-A/C-deficient and -mutant cells fail to adequately trigger mechanoresponsive genes following mechanical stimuli[27–29].

The biological mechanism linking chromatin decondensation to nuclear auxeticity could be further investigated by examining nuclear auxeticity in cell lines with knockouts or knockdowns of nucleo-cytoskeletal genes or by chemically inhibiting nucleo-cytoplasmic translocation of molecules using Leptomycin B. Nucleo-cytoskeletal genes of interest in this context may be identified by ChIP which is used to examine proteins binding to chromatin. Additionally, comparisons of expression levels - or intracellular localisation and abundance of nucleo-cytoskeleton components - between control and CIT/TSA treated cells could provide valuable information and guide studies to determine the key regulators of nuclear auxeticity. For such investigations, RNA-sequencing as well as fluorescence and super-resolution microscopy have been widely applied.

7.1.2. A role for lamin A/C in nuclear auxeticity

Although lamins, in particular lamin-A/C, are important for mechanical properties of the nucleus[26] and play a role in mechanotranduction[27–29], their role in nuclear

auxeticity is less clear. This is because lamin-A/C are not expressed in ES cells. High expression of lamin-A/C occurs later during cell differentiation[231, 232]. In agreement with this, when a role for lamin-A/C in ES cell nuclear auxeticity was considered, expression was found to be low to undetectable. Further, no change in expression was seen between naïve and transitioning ES cells[124]. Curiously, lamin-A/C is expressed in all adult cells - with the exception of T cells and B cells[233]. Perhaps, the absence of lamin-A/C is a prerequisite for nuclear auxeticity in response to chromatin decondensation.

7.1.3. Regulated and bilateral cytoskeletal/nuclear crosstalk

It could be further postulated that this potential cytoskeletal/nuclear crosstalk is: i) bilateral, whereby mechanical signals from the nuclear architecture can also affect cytoskeletal dynamics, and ii) regulated, whereby these crosslinking signals are pronounced during important cellular transitions and less acute during static cellular growth. A working rationale could be that much like mechanotransduction mechanisms at the cell surface could lead to substantial conformational changes in chromatin and ultimately transcriptional control; so too could chromatin conformational changes lead to alteration in overall mechanical properties of the cell. Interestingly, studies have previously shown that lymphocytes could be susceptible to mechanical signalling[74, 234], but a direct mechanical signalling from the surface of the cells to the chromatin has not yet been shown. This hereby proposed regulated and bilateral crosstalk could potentially mediate a feedback loop for mechanical transduction signalling that ensures adequate cell development and function.

7.1.4. Nuclear auxeticity in primary B cells

While a subset of B cell nuclei showed auxetic properties, many did not. Such discrepancy could be attributed to i) the dormant G0 state of non-activated primary B cells, and/or ii) inherent robustness of primary cells against mechanical manipulation. Non-immunised B cell splenocytes are known to exist in a quiescent G0 state which drastically decreases the active properties of these cells[235] thereby hindering the manifestation of adequate auxetic properties in the timeframe studied. In addition, it has been shown that primary cells are naturally more robust in various signalling cascades due to inherent redundancies that are retained in primary cells and which tend to be lost in cancer cell lines used in culture[236, 237]. This is not thought to be

a strong contributing factor though, because some auxetic primary B cell nuclei were indeed observed. Taken together, the FTIR and nuclear auxeticity data do hold true in both B cell lines and primary B cells, however, the likelihood of technical limitations inherent to primary B cells should be taken into consideration for the nuclear auxeticity measurements.

Further experiments may help elucidate the more complicated intracellular response to immune activation seen in primary B cells. Atomic force microscopy has also been used to examine nuclear auxeticity and could be used here to assess if primary cells do indeed have an inherent robustness against mechanical manipulation or if technical limitations of the technique were the main cause of the differences seen between the cell line and the primary B cells. Further comparisons of the nucleo-cytoskeletal components in CH12F3 cells and primary B cells using RNA sequencing and fluorescence microscopy may also add to our understanding of the inherent differences that exist between the two.

7.1.5. Future perspectives: auxeticity and its mechanisms

In summary, I have optimised a novel tool for assessing chromatin architecture at the single cell level. By assessing both biochemical and mechanical changes for the same cell treatments, changes in chromatin architecture were correlated with nuclear auxeticity. The data corroborates previous work done in stem cells and raises the question if nuclear auxeticity is a general feature of cellular development. If so, this suggests that nuclear auxeticity could be a general phenomenon of active global cellular transcription and/or a property of cellular development whereby the nuclear architecture develops a specific property to accommodate the extensive pertubations and modifications taking place throughout the chromatin.

It would be interesting though in the future to identify mechanisms that interfere with nuclear auxeticity to study the effect of its blockade on normal cellular development and differentiation. Furthermore, mechanotransduction has been implicated in key cellular developmental processes, including the immune system[74, 238], and is speculated to account for lack of efficiency in cellular differentiation or trans-differentiation *ex vivo*. Indeed, the use of B cell organoids, 3D structures mimicking the mechanical forces displayed in lymphoid tissues *in vivo*, have been shown to greatly enhance antibody diversification in B cells through immune activation, indicating a role of mechanical and structural properties[239]. Understanding the role of auxeticity and the

potential feedback loop between the nucleus and cytoskeleton, could further advance our understanding of the role of chromatin conformation and mechanical forces - and the interplay between the two - in cell development.

Finally, these observations need not be confined to B cell biology. Many of the observations herein could be applicable to other cell types undergoing differentiation, re-differentiation, or trans-differentiation whereby fundamental and global chromatin changes are required. Cancer cells have been known to take advantage of trans-differentiation to maintain their survival and/or malignancy according to the cancer stem cell hypothesis[240, 241]. It would be interesting if these assays could be tested in the future as a diagnostic tool for tumour progression or severity at the single tumour cell level.

7.2. Monitoring chromatin changes in single cells with vibrational spectroscopy

Chromatin changes during B cell immune and transcriptional activation was assessed in single cells using FTIR imaging and Raman mapping (chapter 3 and chapter 6). Because chromatin conformation is an important marker of the transcriptional state and health of a cell, quantification of chromatin changes has great potential in both biomedical research and clinical settings. The label-free aspect of vibrational spectroscopy makes it even more compelling.

Potential applications are not confined to lymphocytes. Label-free phenotypic characterisation of stem cells could aid quality control of the cells used in research and treatment regimes. Fertility treatments could also benefit through label-free characterisation of sperm cells, whose health is tightly correlated with their chromatin condensation state[242–244]. Identification of FTIR and Raman spectral markers of intracellular chromatin changes are therefore of great interest.

7.2.1. Measuring chromatin changes in single cells using FTIR imaging

Using image segmentation analysis, single cell spectra were extracted from FTIR images of untreated control B cells, as well as CIT and TSA treated B cells. The single cell data revealed spectral changes in response to the chromatin decondensation occuring within the cells treated with CIT or TSA. Peaks associated with the

vibrational modes of nucleic acid, $\nu_s(PO_2^-)$ and $\nu_{as}(PO_2^-)$, were found to decrease in intensity relative to peaks associated with protein. A DNA-to-protein peak ratio for monitoring chromatin condensation state in single cells could therefore be determined. Specifically the ratio between $\nu_s(PO_2^-)$ and Amide II.

It is important to note that this peak ratio was also affected by the cell cycle phase of the cells - specifically the change in intracellular DNA content. As such, the FTIR imaging could not stand alone in confidently determining the chromatin changes. In this work, cell cycle phase distribution measurements using flow cytometry were used to support the results. For other cell types, this may not be necessary depending on the objective. Sperm cells for example are haploid and their DNA content does not change.

The DNA-to-protein ratio is a reasonable spectral measurement of chromatin structure; the ratio decreases as chromatin unravels and becomes more open with a less ordered structure. This principle is likely to be universal throughout cell types. However, due to the biochemical differences between cell types, the spectral analysis that enables phenotypic characterisation of single cells will need to be optimised for each cell type and measurement condition.

7.2.2. Measuring chromatin change in single live cells using Raman mapping

Raman maps of live control and CIT treated B cells provided further insights. Using common k-means cluster analysis, the nucleus was identified within each cell. The extracted nuclei spectra corroborated the previous FTIR data; DNA associated peaks were affected by chromatin changes. The relative change in a peak associated with $\nu_s(PO_2^-)$, 786 cm^{-1}, was again used as a marker for chromatin decondensation.

Interestingly, this peak is a marker of the phosphodiester symmetric stretch of B-DNA. A downshift in signal is seen during B to Z transition of DNA[201], which has a known association with active transcription[222, 223]. The structural changes to DNA that occur in response to chromatin decondensation and the following transcriptional upregulation are therefore a plausible cause of the spectral markers. The following PCA and LDA analyses further explored the peak differences between control and CIT treated cells. Peaks associated with nucleic acids were prominent and additional markers of Z-DNA (812 cm^{-1} and 1424 cm^{-1}) featured. This supports the use of the $\nu_s(PO_2^-)$ peak as a spectral marker of intracellular chromatin changes.

7.2.3. Future perspectives: label-free chromatin conformation monitoring

The CIT treated CH12F3 cells were measured 24 hours post-treatment for FTIR imaging and 96 hours post-treatment for Raman mapping. For primary B cells measured with FTIR imaging, two timepoints were examined (24 hours and 48 hours). This spectral data indicated an ongoing change to chromatin structure. Additional timepoints using both FTIR imaging and Raman mapping could provide additional information about the chromatin dynamics and the spectral effects of these during B cell activation. This could serve to validate and further inform the use of the peak ratios discussed herein for phenotypic characterisation of single cells.

The potential applications for phenotypic characterisation of single cells based on chromatin condensation state are numerous. If this is to be used in conjunction with other measurement techniques, or indeed to inform downstream analyses, live cell measurements are a requirement. Microfluidic devices enable this. Cost and fabrication difficulties of suitable devices should be considered in the endeavour to make label-free vibrational spectroscopy measurements of single live cells a readily available tool within biomedical and biological research. In this thesis I examined the suitability of PDMS based microfluidic chips for both FTIR imaging and Raman mapping (chapter 5). While the strong signal of PDMS was a factor for both experimental approaches, PDMS based devices had potential for both. It was most suitable for Raman mapping using a confocal microscope, so PDMS could be entirely excluded from the sampling area.

Further optimisations to experimental setup is needed for routine measurements. A Raman system with an inverted microscope would greatly simplify the measurement process, as the chip would not need to be placed upside down for the measurements. For the setup used here, the chip holder does a good job at keeping the chip in place. It also has space for tubing to be attached to the chip - enabling time course measurements of cells in culture medium with ongoing replenishment. Following the same cell over a number of hours (or even days) would add new layers to our understanding of the spectral markers associated with the activation initiated chromatin changes. Indeed, it may reveal interesting subpopulations as it did for the cell deformability measurements of auxeticity.

7.3. Correlation between Raman and transcriptomic data

Determining specific spectral markers for phenotypic characterisation of cells during differentiation or transcriptional activation have many potential applications, as discussed previously. However, the spectral data collected from cells do of course contain even more chemical information. Indeed, Raman spectroscopy measures the biochemical composition of the whole cell, and the biological origin of each Raman peak is of great interest. Raman maps were collected of two populations of single live B cells; untreated D0 cells and CIT treated D4 cells, 96 hours post-treatment (chapter 6). Principal component analysis (PCA) and linear discriminant analysis (LDA) revealed significant spectral differences between the two groups, including peaks associated with nucleic acid, protein, lipids and sugars.

To unravel this myriad of spectral differences, the Raman data were correlated with transcriptomic data using a partial least squares (PLS) regression model. Furthermore, a VIP list of the transcripts with the highest importance for the model was generated. The nucleus and cytoplasm was identified for each cell using common k-means cluster analysis. All downstream analyses including PCA, LDA and PLS regression were performed using 'nucleus', 'cytoplasm', and 'whole cell' spectral data in parallel. This separation was used to 1) identify key peaks associated with nucleic acid, and 2) facilitate the detection of potential differences in PLS model and VIP transcript lists for each cellular compartment.

7.3.1. Nucleus, cytoplasm or whole cell spectra?

Looking at the whole Raman spectrum and downstream analyses, it is apparent that the spectra identified as from the nucleus are unlikely to be "pure" spectra (completely free of cytoplasmic signal). The similar VIP transcript lists of especially the 'nucleus' and 'whole cell' analyses support this. Although a confocal microscope was used, optical signal from cytoplasm above and below the nucleus was likely measured too. The relatively large nucleus of CH12F3 cells and the round shale of the cells could have contributed to this. For larger and flatter adherent cells with smaller nuclei relative to overall cell size, this may not occur to the same extent. Here it could be interesting to determine if a PLS regression model and its top VIP transcripts differed more between distinct cellular regions than for CH12F3 cells.

7.3.2. PLS model can predict Raman data from transcriptomic data

The PLS analysis determined that a linear correlation exists between Raman data and transcriptomic data of CH12F3 cells. Using a leave-one-out approach, the PLS model was used to predict Raman data from transcriptomic data. Plotting the predicted Raman data among single cell experimental data illustrated the validity of the model. The reverse - predicting transcriptomic data from Raman data - is also possible, as shown in yeast and bacteria[102]. In this context, phenotypic characterisation of single cells based on Raman measurements becomes particularly powerful. Accurately predicting the upregulation of pathways and intracellular processes - without the need for RNA extraction and sequencing - has a large number of potential applications within both research and clinical settings, for example for disease detection.

The VIP transcript lists provided a number of interesting regulatory RNAs and proteins; some with known roles in B cell immune activation - and some with no known roles. These "unknowns" could play an important part in B cell activation and it would be interesting to further explore this. This also suggests that the methodology could have the potential to identify novel molecular factors that other conventional assays might miss.

7.3.3. Future perspectives: the correlation between Raman and transcriptomic data

Additional time points between D0 and D4 could further elucidate the correlation between Raman spectra and transcriptomic profiles. As there is some, although minor, inter-sample variability due to confluency levels and number of cell passages, it may also be beneficial to extract RNA and measure Raman spectra of cells from the same population on the same day. Should technology one day allow it, single-cell transcriptomics combined with Raman measurements would be a very powerful approach to unravelling the direct relationship between the two complementary data types. Indeed, there is still much to be determined, but there most certainly is a correlation between transcriptomic profiles and Raman spectra. Understanding the origin of this correlation in different case studies will add value to Raman measurements of biological samples and aid interpretation of spectral changes. Furthermore, the work outlined here, suggest that Raman may also aid in the identification of key regulatory transcripts for immune activation. Future work will demonstrate if

this can be translated to elucidating other cell developmental processes, occurring in healthy cells or during disease.

7.4. Combining biochemical and biophysical measurements of live cells

A combination of biochemical and biophysical signalling cascades are responsible for cell survival and function. No single pathway stands alone. Mechanical properties of the nucleus can be altered through biochemical pathways. Transcription activation can be initiated through mechanotranduction. This crosstalk between nucleus and cytoskeleton, conveying and responding to both mechanical and chemical stimuli, highlights the value of comparing chemical and mechanical data for the same cells and cell treatments (Figure 7.1).

Simultaneous biochemical and biomechanical measurements could provide additional valuable information. Incompatibilities between current techniques can make this difficult. The nuclear stain used for the deformability cytometry measurements in this thesis would interfere with the spectral data collected through FTIR imaging and Raman mapping. Additionally, the measurement times of both Raman mapping and FTIR imaging are too long for cells in motion. For simultaneous measurements, novel techniques and experimental setups are needed.

Brillouin spectroscopy, an emerging tool within mechanobiology, is a label-free optical technique for probing the mechanical properties of a sample[245, 246]. Recently, mechanical properties of cell nuclei have been measured using this technique - comparing untreated with TSA treated cells. A softening of the nucleus in response to chromatin decondensation was shown[126]. Experimental setups combining Raman spectroscopy and Brillouin spectroscopy allow for simultaneous collection of Raman and Brillouin measurements from the same sample, indeed the same spatial location[247, 248]. Experimental setups such as these may provide new insights into the crosstalk between biochemical and biomechanical signalling pathways.

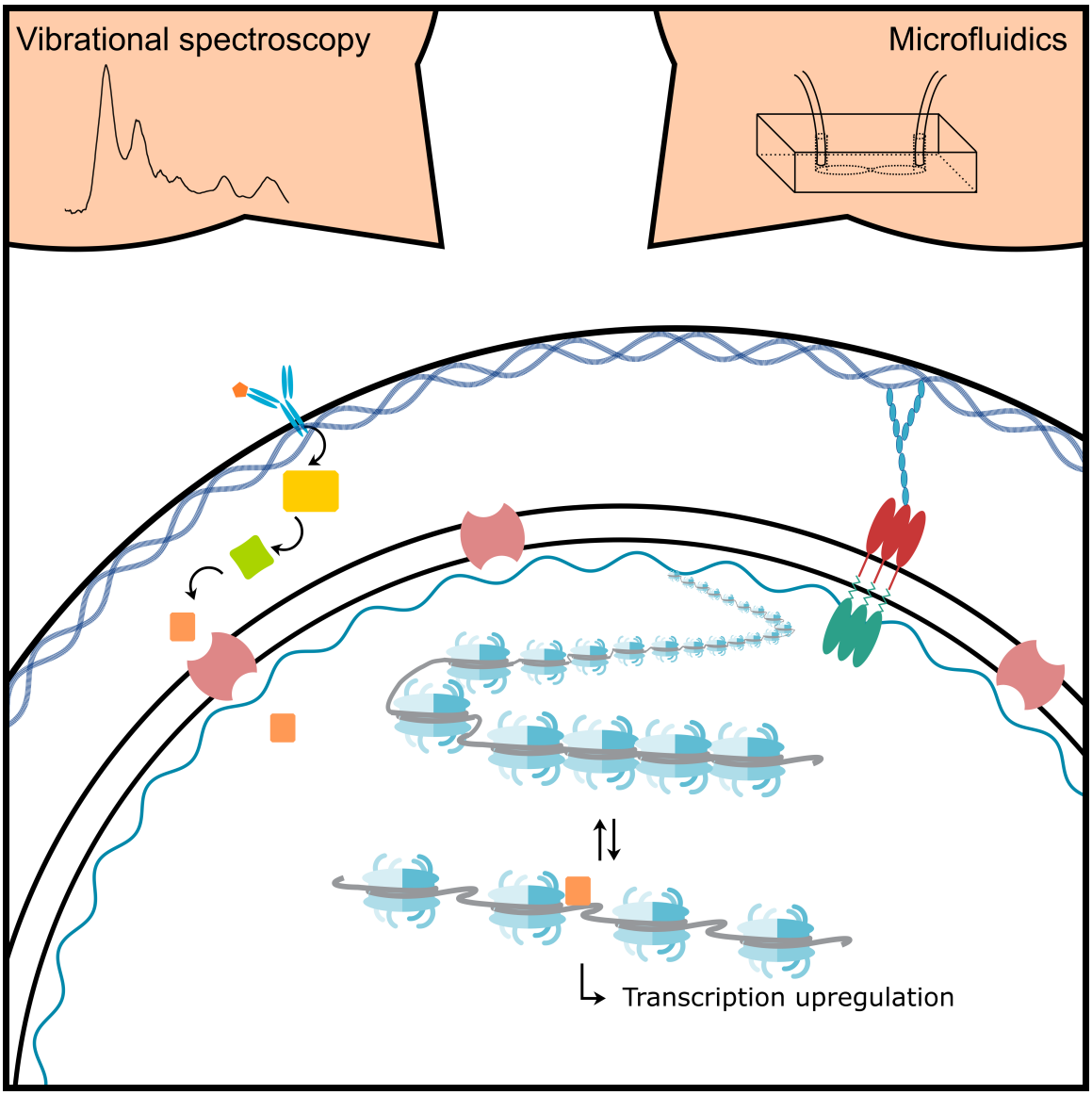

Figure 7.1.: *Thesis graphical summary.*
This thesis focused on the intracellular regulation and signalling that results in chromatin changes which in turn lead to the transcriptional changes that determine cell fate. Both biochemical signalling and mechanotransduction play a role, and as such chemical as well as mechanical measurements are needed to shed light on these processes.

A. Supporting Information: Cell treatments and flow cytometry analysis

A.1. Cell cycle analysis

Figure A.1 shows the analysis steps that are performed prior to cell cycle analysis. The first step is gating the live (or healthy) population based on FSC and SSC (Figure A.1a). This step is performed for all flow cytometry analyses in order to exclude debris and dead cells.

The second step is gating the single cells, or singlets, based on height and area of the propidium iodide signal (Figure A.1b). A logarithmic scale is used for the majority of flow cytometry analysis of changes in intracellular molecule content. For cell cycle analysis, DNA content only doubles between the G1 and G2 phases. Therefore a linear scale is necessary. Gating for single cells is important in order to exclude cell doublets, which could affect the cell cycle phase distribution.

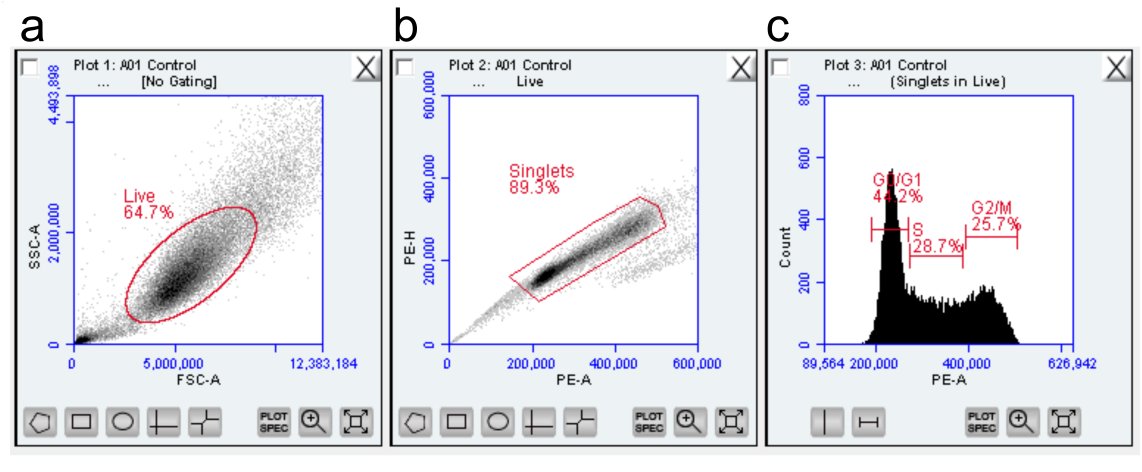

Figure A.1.: *Cell cycle analysis steps.*
a *The first gate, live cells, excludes debris and dead cells.* ***b*** *The second gate, singlets, only includes single cells.* ***b*** *Analysis of the cell cycle phase distribution is now possible.*

A.2. Endocycling in response to Nocodazole treatment of CH12 cells

A curious process was observed during the optimisation of Nocodazole treatment of CH12 cells for G2/M phase stalling. For long incubation times (18 hours), the cells did not stall in G2/M phase as expected. Instead, the cells began the process of endoreduplication, or endocycling. During this, cells continue replicating the nuclear genome but do not go through mitosis. The result is single cells, which have an intracellular DNA content higher than G2/M phase cells (>2× DNA content).

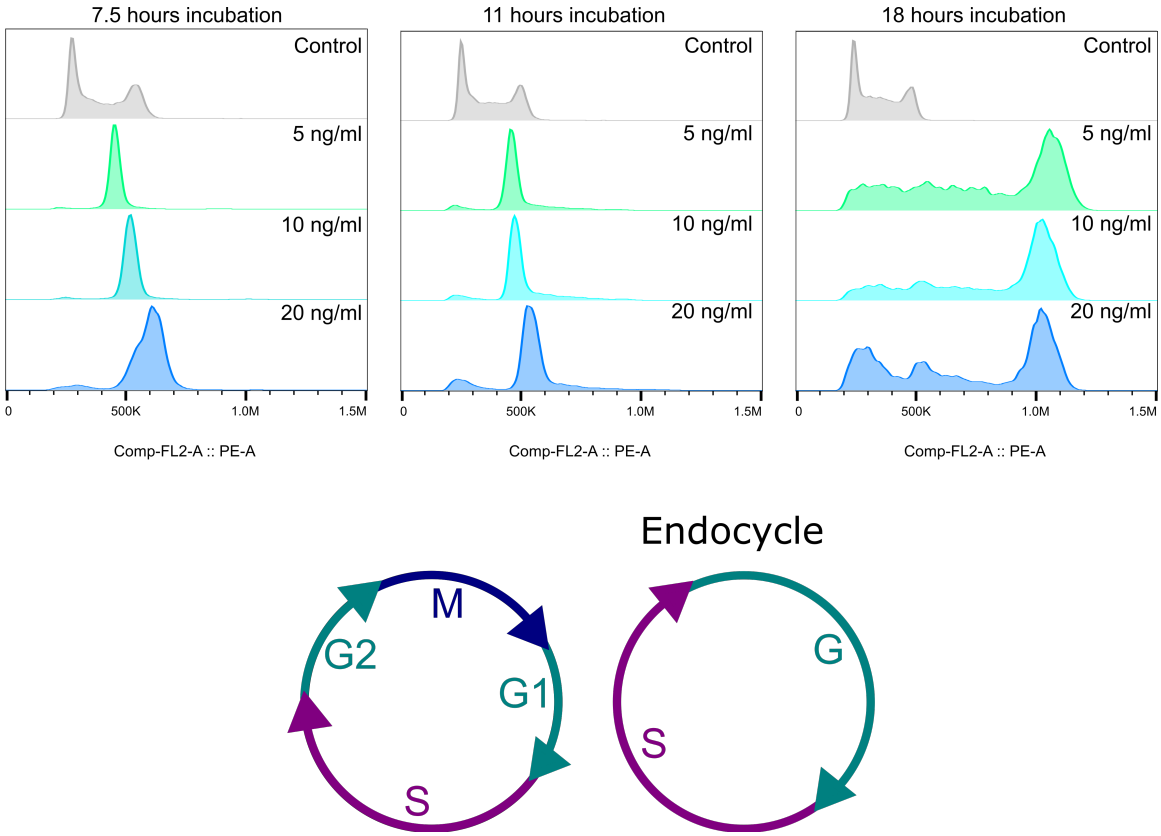

Figure A.2.: *Endocycling in response to Nocodazole treatment of CH12 cells. For long incubation times (18 hours), the intracellular DNA content increased to >2×. This happens when cells, instead of going through normal cell cycle progression, commence a process called endocycling.*

B. Supporting Information: FTIR spectral interpretations

B.1. Peak assignments

Peak position	Assignment	Ref
3600-3500	Amide A, ν(N-H)	[176]
3490	ν_3, ν_{as}OH	[176]
3300	Amide A, NH stretching	[185]
3277	ν_2, ν_{as}OH	[176]
3100	Amide B, NH stretching	[185]
2956	$\nu_{as}CH_3$ acyl chain lipids	[176]
2922	$\nu_{as}CH_2$ acyl chain lipids	[176]
2874	ν_sCH_3 acyl chain lipids	[176]
2852	ν_sCH_2 acyl chain lipids	[176]
1740	ν(C=O) ester carbonyl	[176]
1715	B-DNA base pairing vibration (νC=O & νC=N)	[176]
1708	A-DNA base pairing vibration (νC=O & νC=N)	[176]
1720-1666	νC=O from purine and pyrimidine	[176]
1695	Z-DNA base pairing vibration (νC=O & νC=N)	[176]
1690	RNA,$\nu_a(C_2{=}O)$	[176]
1660-1665	DNA,$\nu(C_5{=}O)$,δ(N=H), RNA,ν(C6=O)	[176]
1650	Amide I, α-helical	[176, 185]
1642	ν2,$\delta(H_2O)$	[176]
1635	Amide I, β-pleated sheet	[176, 185]
1610	DNA and RNA,$\nu C_4{=}$C5 imidazole	[176]
1605	DNA,δNH_2	[176]
1578	DNA and RNA,νC=N imidazole ring	[176]

1545-1530	Amide II	[176, 185]
1418,1425,1408	A-DNA, B-DNA, Z-DNA deoxyribose	[176]
1457	$\delta_{as}CH_3$ of cellular proteins	[176]
1450	CH_2	[176]
1400	COO_2^- of fatty acids and amino side chains	[176]
1300-1250	Amide III	[176, 185]
1244	RNA,$\nu_{as}PO_2^-$	[176]
1240,1225,1215	A-DNA, B-DNA, Z-DNA, $\nu_{as}PO_2^-$	[176]
1185	A-DNA, ribose	[176]
1160,1120	RNA,ν(C=O) ribose	[176]
1080	DNA,$\nu_sPO_2^-$	[176]
1060,1050	DNA, RNA,ν(C-O) ribose	[176]
1038	RNA,ν(C=O) ribose	[176]
1015	DNA and RNA,ν(C-O) ribose	[176]
1014-1018	Z-DNA marker band	[176]
996	RNA, uracil ring motions	[176]
970, 915	DNA, RNA, ribose-phosphate skeletal motions	[176]
899,894,929	A-DNA, B-DNA, Z-DNA	[176]
806,830-840	A-DNA, B-DNA	[176]

Table B.1.: *FTIR spectral interpretations. Adapted from [176]*

C. Supporting Information: Raman spectral interpretations

C.1. Peak assignments

Peak position	Assignment	Ref
600-800	Nucleotide conformation	[249]
607	Glycerol	[249]
608	Cholesterol	[249]
614	Cholesterol ester	[249]
618	C-C twisting (protein)	[249]
620	C-C twist aromatic ring (xylene)	[249]
621	C-C twisting mode of phenylalanine (proteins)	[249]
630	Glycerol	[249]
630-670	ν(C-S) *gauche* (amino acid methionine)	[249]
639	Tyrosine ring breathing	[249]
640	C-S stretching and C-C twisting of proteins; tyrosine	[249]
643	C-C twisting mode of tyrosine	[249]
645	C-C twisting mode of phenylalanine (proteins)	[249]
646	C-C twisting mode of tyrosine	[249]
662	C-S stretching mode of cystine (collagen type I)	[249]
666	G,T (ring breathing modes of the DNA bases), backbone in RNA	[249]
667-669	C-S stretching mode of cytosine (collagen type I)	[249]
667-669	T,G (DNA/RNA)	[249]
669	C-S stretching mode of cytosine	[249]
669	ν_7(δ: porphyrin deformation),observed in the spectra of single human RBC	[249]

671	Ring breathing of tryptophan	[249]
678	Ring breathing modes in the DNA bases	[249]
	G (ring breathing modes in the DNA bases) /C-2'-endo-anti	[249]
700-745	ν(C-S) *trans* (amino acid methionine)	[211, 249]
702	Cholesterol, cholesterol ester	[249]
717-719	C-N (membrane phospholipids head)/adenine	[249]
	$CN^{+}(CH_3)_3$ (lipids)	[249]
718	Choline group	[211, 249]
719	C-N (membrane phospholipid head) /nucleotide peak	[249]
	Symmetric stretch vibration of choline group $N^{+}(CH_3)_3$,characteristic for phospholipids	[211, 249]
	Phosphatidylcholine, sphingomyelin	[211, 249]
720-722	DNA	[249]
724	Nucleic acids	[249]
725	A (ring breathing mode of DNA/RNA bases)	[249]
726	C-S (protein), CH_2 rocking, adenine	[249]
727-728	C-C stretching, proline (collagen assignment)	[249]
	Lipid	[249]
728	Ring breathing of tryptophan	[249]
729	A (DNA/RNA)	[249]
733	Phosphatidylserine	[211, 249]
735	C-S stretch (one of three thiocyanate peaks, with 2095 and 445 cm^{-1})	[249]
742	DNA, tryptophan	[249]
746	T (ring breathing mode of DNA/RNA bases)	[249]
748	DNA	[249]
749	Symmetric breathing of tryptophan (protein assignment)	[249]
750	$CH_{2,6}$ out-of-plane bending, observed in the spectra of single human RBC	[249]
	Lactic acid	[249]
752	ν_{15} (porphyrin breathing mode)	[249, 250]
752	Thymine	[251, 252]
752-755	Symmetric breathing of tryptophan	[206–208, 249]
755-756	Symmetric breathing of tryptophan	[203, 249]

759	Tryptophan	[203, 249]
	Ethanolamine group	[211, 249]
	Phosphatidylethanolamine	[211, 249]
760	Tryptophan, δ(ring)	[204, 209, 249]
766	Pyrimidine ring breathing mode	[249]
776	Phosphatidylinositol	[211, 249]
780	Uracil-based ring breathing mode	[249]
781	Cytosine/uracil ring breathing	[203, 249]
782	U,T,C (ring breathing modes in the DNA/RNA bases)	[204, 249]
784-745	Phosphodiester; cytosine	[205, 249]
784-787	C ring breathing mode	[201, 221]
	Backbone O-P-O for B-DNA	[201, 221]
	Higher intensity for B-DNA than Z-DNA or A-DNA	[201, 221]
785	U,T,C (ring breathing modes in the DNA and RNA bases)	[249, 253]
	Backbone O-P-O	[249, 253]
786	DNA: O-P-O, cytosine, uracil, thymine	[203, 249]
	Pyrimidine ring breathing mode	[202, 249]
787	Nucleic acids	[249]
	Phosphatidylserine	[211, 249]
788	O-P-O stretching DNA	[204, 249]
791	Pyrimidine	[249]
800-1200	Backbone geometry and phosphate ion interactions	[249]
802	Uracil-based ring breathing mode	[249]
810	Phosphodiester (Z-marker)	[205, 249]
811	O-P-O stretching (RNA)	[204, 249]
812	Phosphodiester (Z-marker)	[205, 249]
813	One of the two most distinct peaks for RNA (with 1240cm^{-1})	[249]
	C-C stretching (collagen assignment)	[249]
	O-P-O (RNA)	[204, 249]
815	Proline, hydroxyproline, tyrosine, $\nu_2PO_2^-$ stretch of nucleic acids	[249]
816	Collagen	[249]

817	C-C stretching (collagen)	[249]
820	Protein band	[249]
	Proteins, including collagen I	[249]
820-930	C-C stretch of proline and hydroxyproline	[249]
822	Phosphodiester	[205, 249]
823	Out-of-plane ring breathing, tyrosine (protein assignment)	[249]
823-826	Phosphodiester	[205, 249]
826	O-P-O stretch DNA	[203, 249]
827	Proline, hydroxyproline, tyrosine, $\nu_2PO_2^-$ stretch of nucleic acids	[249]
828	Out-of-plane ring breathing, tyrosine	[203, 204, 249]
	Phosphodiester stretching DNA/RNA	[203–205, 249]
830	Proline, hydroxyproline, tyrosine, $\nu_2PO_2^-$ stretch of nucleic acids	[249]
	C-H out-of-plane bending in benzoid ring	[249]
831	Asymmetric O-P-O stretching, tyrosine	[249]
838	Deformative vibrations of amine groups	[249]
840	α-Anomers	[211, 249]
	Glucose-saccharide band	[211, 249]
	Saccharide (α)	[211, 249]
840-860	Polysaccharide structure	[210, 249]
842	Glucose	[203, 249]
847	Monosaccharides (α-glucose), (C-O-C) skeletal mode	[249]
	Disaccharide (maltose), (C-O-C) skeletal mode	[249]
852	Proline, hydrocyproline, tyrosine	[249]
	Tyrosine ring breathing	[249]
	Glycogen	[249]
853	Ring breathing mode of tyrosine and C-C stretch of proline ring	[203, 249]
	Glycogen	[249]
854	(C-O-C) skeletal mode of α-anomers (polysaccharides, pectin)	[249]
	Ring breathing tyrosine (proteins)	[249]
855	Proline, tyrosine	[206, 249]

	ν(C-C), proline + δ(CCH) ring breathing, tyrosine	[206, 249]
	δ(CCH) phenylalanine, olefinic	[249]
	Collagen	[249]
855-856	Proline, hydroxyproline, tyrosine	[249]
	C-C stretching, proline (collagen)	[249]
856	Amino acid side chain vibrations of proline and hydroxyproline	[249]
	(C-C) vibration of the collagen backbone	[249]
859	Tyrosine, collagen	[203, 249]
860	Phosphate group	[211, 249]
	Phosphatidic acid	[211, 249]
867	Ribose vibration, one of the distinct RNA modes (with 915 and 974 cm^{-1})	[249]
868,870,872	Lipid	[249]
868	C-C stretching, hypro (collagen)	[249]
	Monosaccharides (β-fructose), (C-O-C) skeletal mode	[209, 249]
	Disaccharide (sucrose), (C-O-C) skeletal mode	[209, 249]
	Polysaccharides, amylase	[209, 249]
	Polysaccharides, amylopectin	[209, 249]
869	Proline	[203, 249]
870	C-C stretching, hypro (collagen)	[249]
873	Hydroxyproline, tryptophan	[249]
874	C-C stretching, hypro (collagen)	[249]
875	Antisymmetric stretch vibration of choline group $N^+(CH_3)_3$, characteristic of phospholipids	[211, 249]
	Phosphatidylcholine, sphingomyelin	[211, 249]
876	ν(C-C), hydroxyproline (protein)	[249]
	C-C stretching, hydroxyproline (collagen)	[249]
877	C-C-N^+ symmetric stretching (lipids)	[204, 249]
	C-O-C ring (carbohydrate)	[204, 249]
879	Hydroxyproline, tryptophan	[208, 249]
880	Tryptophan, δ(ring)	[209, 249]
883	$\rho(CH_2)$, protein	[249]
884	Proteins, including collagen I	[249]

885	Disaccharide (cellobiose), (C-O-C) skeletal mode	[249]
889	Methylene rocking	[249]
890	Protein bands	[249]
	β-Anomers	[211, 249]
891	Saccharide band	[211, 249]
893	Backbone, C-C skeletal	[249]
893-896	Phosphodiester, deoxyribose	[205, 249]
898	Monosaccharides (β-glucose), (C-O-C) skeletal mode	[209, 249]
	Disaccharide (maltose), (C-O-C) skeletal mode	[209, 249]
	Adenine	[207, 249]
904	C-C skeletal stretching	[249]
906	Tyrosine	[249]
912	Calcium oxalate	[249]
913	Glucose	[211, 249]
915	Ribose vibration, one of the distinct RNA modes (with 915 and 974 cm^{-1})	[249]
918	Proline, hydroxyproline	[249]
	Glycogen and lactic acid	[249]
920	C-C stretch of proline ring/glucose/lactic acid	[203, 249]
	C-C, praline ring (collagen)	[249]
921	Proline ring/glucose/lactic acid/praline ring	[249]
922	C-C stretch	[249]
928-940	ν(C-C), stretching; probably in amino acids proline and valine	[249]
931	Carbohydrates peak for solutions and solids	[249]
932	Skeletal C-C, α-helix	[249]
933	Proline, hydroxyproline, μ(C-C) skeletal of collagen backbone	[249]
934	C-C backbone (collagen)	[249]
935	C-C stretching mode of proline and valine and protein backbone (α-helix conformation)	[249]
	Glycogen	[249]
	P(CH_3 terminal, proline, valine + μ(CC) α-helix keratin (protein)	[203, 249]
937	Proline (collagen type I)	[249]

	Amino acid side chain vibrations of proline and hydroxyproline	[249]
	C-C backbone (collagen)	[249]
	Glycogen	[249]
	ν(C-C) residues (α-helix)	[249]
	C-O-C glycodides (carbohydrates)	[249]
	Collagen	[249]
937-938	Proline, hydroxyproline, ν(C-C) skeletal of collagen backbone	[208, 249]
938	C-C stretch backbone	[203, 249]
941	Skeletal modes (polysaccharides, amylose and amylopectin)	[209, 249]
950	Proline, valine, polysaccharides	[249]
	Calcium phosphate stretch band	[249]
951	$\nu_s(CH_3)$ of proteins (α-helix)	[249]
956	Carotenoids (absent in normal tissues)	[249]
957	Hydroxyapatite, carotenoid, cholesterol	[203, 249]
960	Symmetric stretching vibration of $\nu_1 PO_4^{3-}$ (phosphate HA)	[208, 249]
	Calcium-phosphate stretch band (high quantities of cholesterol)	[249]
	Quinoid ring in-plane deformation	[249]
	Calcium hydroxyapatite	[249]
962	Phosphate symmetric stretching vibration of calcium hydroxyapatite	[249]
966	Hydroxyapatite	[249]
968	Lipids	[249]
970	Phosphate monoester groups of phosphorylated proteins and cellular nucleic acids	[249]
971	ν(C-C) wagging	[249]
972	Lipid	[249]
972-923	C-C backbone (collagen)	[249]
973	$\rho(CH_3)$, δ(CCH) olefinic (protein)	[249]
974	Ribose vibration, one of the distinct RNA modes (with 874 and 915 cm^{-1})	[249]
980	C-C stretching β-sheet (protein)	[204, 249]
991	Single human RBC, phenylalanine, NADH	[249]

996	C-O ribose, C-C	[249]
999	ν_{45}(CC) in single human RBC	[249]
1000	Phenylalanine	[249]
	Bound and free NADH	[249]
1001	Symmetric ring breathing mode of phenylalanine	[203, 207, 249]
1002	C-C aromatic ring stretching	[249]
	Phenylalanine	[249]
1003	Phenylalanine, C-C skeletal	[249]
1004	Phenylalanine, ν_s(C-C), symmetric ring breathing	[206, 208, 249, 254–256]
1005	Phenylalanine	[204, 249]
	Carotenoids	[249]
1006	Carotenoids (absent in normal tissues)	[249]
	Phenylalanine, δ(ring)	[209, 249]
1007	Phenylalanine, carbamide	[249]
1008	Phenylalanine	[249]
	ν(CO), ν(CC), δ(OCH), ring (polysaccharides, pectin)	[209, 249]
1011	Tryptophan ring breathing	[249]
1016	Carbohydrates peak for solids	[249]
1017	Ribose	[249]
1018	Stretching C-O ribose	[249]
1022	Glycogen	[249]
1023	Glycogen	[249]
1025	Carbohydrates peak for solutions	[249]
	Glycogen	[249]
1029, 1030	O-CH_3 stretching of methoxy groups	[249]
1030	Phenylalanine of collagen	[208, 249]
	ν(CC) skeletal, keratin (protein)	[249]
	C-H bending	[249]
1031	δ(C-H), phenylalanine	[206, 207, 249]
	Phenylalanine, C-N stretching of proteins	[249]
	Carbohydrate residues of collagen	[249]
1032	CH_2CH_3 bending modes of collagen and phospholipids	[249]
	C-C skeletal stretch	[249]

	Phenylalanine (collagen)	[208, 249]
	Proline (collagen)	[249]
1033	Collagen	[249]
	C-H, Phenylalanine	[249]
	ν(CO), ν(CC), ν(CCO) (polysaccharides, pectin)	[249]
1034	Phenylalanine (collagen)	[208, 249]
1035	Collagen	[249]
1043	Carbohydrates	[249]
	Proline (collagen)	[249]
1044	Symmetric stretching of $\nu_3PO_4^{3-}$ of HA	[208, 249]
	Proline	[249]
1048	Glycogen	[249]
1053	C-O stretching	[249]
1057	Lipids	[249]
1060-1095	PO_2^- stretching (DNA/RNA)	[204, 249]
	Chain C-C stretching (lipids)	[204, 249]
	C-O, C-C stretching (carbohydrates)	[204, 249]
1060-1130	C-C skeletal stretching	[249]
1061	C-C in-plane bending	[249]
	C-N stretching	[249]
	Ceramide	[249]
1063	C-C skeletal stretch random conformation	[249]
1064	Skeletal C-C stretch of lipids	[203, 249]
	Acyl chains	[211, 249]
	ν(C-C) *trans*	[249]
1065	Palmitic acid	[211, 249]
	Fatty acid	[211, 249]
	Proline	[249]
1066-1067	Proline (collagen)	[249]
1070	Triglycerides (fatty acids)	[249]
1070-1090	Symmetric PO_2^- stretching of DNA	[249]
1071	Glucose	[249]
1073	Carbonate symmetric stretching vibration of calcium carbonate apatite	[249]
1074	Glucose, triglycerides, C-C (lipid)	[249]
1076	C-C (lipid)	[249]

	Symmetric stretching vibration of $\nu_3PO_4^{3-}$ of HA	[208, 249]
1078	ν(C-C) or ν(C-O), phospholipids	[249]
	Symmetric phosphate stretch	[249]
	Carbohydrate peaks	[249]
	ν(CC) skeletal	[249]
1080	Typical phospholipids	[249]
	Phosphate vibrations (phosphodiester groups in nucleic acids)	[249]
	Collagen	[249]
1081	$\nu_1CO_3^{2-}$, $\nu_3PO_4^{3-}$, ν(C-C) skeletal acyl backbone in lipid	[208, 249]
1082	Carbohydrate residues of collagen	[249]
	Nucleic acids	[249]
1083	C-N stretching mode of proteins (and lipid mode of lesser degree)	[203, 207, 249]
1084	Phosphodiester groups of nucleic acids	[249]
1086	ν(C-C) *gauche*	[249]
1087	$\nu_1CO_3^{2-}$, $\nu_3PO_4^{3-}$,ν(C-C) skeletal of acyl backbone in lipid	[208, 249]
1087-1090	C-C stretch, PO_2^- stretch	[203, 249]
1090	Symmetric phosphate stretching	[249]
1092-1093	Phosphodioxy	[249]
1093	Symmetric PO_2^- stretching (DNA backbone), C-N of proteins	[249]
1094	DNA	[249]
	C-N stretching	[249]
1095	Lipid	[249]
	ν(C-N)	[208, 249]
	Phosphodioxy group (PO_2^- in nucleic acids)	[204, 249]
1096	Phosphodioxy (PO_2^-) groups	[249]
1099	ν(C-N)	[208, 249]
1100	C-C vibration mode of the *gauche*-bonded chain	[249]
1101	O-P-O backbone stretch of DNA	[249]
1104	Phenylalanine (proteins)	[249]
1111	Benzoid ring deformation	[249]

1112	Saccharide band (overlaps with acyl band)	[211, 249]
1115, 1116	$CH_{2,6}$ in-plane band and C_{1}-C_{α}-H_{α} bend	[249]
1117	Glucose	[211, 249]
1117-1119	C-C stretch (breast lipid)	[203, 249]
1120	Strong C-O band of ribose (RNA marker, solutions)	[249]
1123	(C-N), proteins	[203, 207, 249]
1124	ν(C-C) skeletal of acyl backbone in lipid (*trans* conformation)	[208, 249]
1126	ν(C-C) skeletal of acyl backbone in lipid (*trans* conformation)	[208, 249]
	C-N stretching, proteins	[249]
	ν(C-O)+ ν(C-C), disaccharides, sucrose	[249]
1127	ν(C-N)	[249]
1128	C-N stretching, proteins	[204, 249]
	C-O stretching, carbohydrates	[204, 249]
1128-1129	ν(C-C) skeletal of acyl backbone in lipid (*trans* conformation)	[208, 249]
1130	ν(C-C) skeletal of acyl backbone in lipid (*trans* conformation)	[249]
	Acyl chains	[211, 249]
1131	Palmitic acid	[211, 249]
	Fatty acid	[211, 249]
	C-C skeletal stretching	[249]
1149	Carbohydrates (solids)	[249]
1150	Glycogen	[249]
	Carotenoid	[249]
1152	ν(C-N), proteins and ν(C-C), carotenoids	[249]
1153	Carbohydrates (solutions)	[249]
1154	β-Carotenes	[207, 249]
1155-1157	Carotenoids	[249]
1155	C-C (and C-N) stretching of proteins and carotenoids	[203, 207, 249]
	Glycogen	[249]
1156	C-C, C-N stretching (protein)	[249]
1156-1157	Carotenoids (absent in normal tissue)	[249]
1158	C-C/C-N stretching (protein)	[204, 249]

1160	C-C/C-N stretching (protein)	[249]
1161	Deformative vibrations of quinoid ring	[249]
1163	Tyrosine	[208, 249]
1167	N=Quinoid ring=N stretching and C-H in plane bending	[249]
1168	Lipids	[249]
	ν(C=C) δ(COH), lipid	[249]
	ν(C-C), carotenoids	[249]
1169	Tyrosine	[208, 249]
1170	C-H in-plane bending mode of tyrosine	[203, 207, 249]
1171	Tyrosine	[208, 249]
	(CH) phenylalanine	[249]
1172	δ(C-H), tyrosine (protein)	[249]
1173	Cytosine, guanine	[205, 249]
	Tyrosine (protein)	[208, 249]
1174	Tyrosine, phenylalanine, C-H bend (protein)	[249]
1175-1176	Cytosine, guanine	[205, 249]
1176	C-H bending tyrosine (protein)	[204, 249]
1177	Cytosine, guanine	[205, 249]
1180	Cytosine, guanine	[205, 249]
1180-1184	Cytosine, guanine, adenine	[203, 249]
1199	Tryptophan ring breathing	[249]
1200	Nucleic acids and phosphates	[249]
	Aromatic C-O and C-N	[249]
1200-1300	Amide III (protein)	[204, 249]
1200-1350	Amide III; due to C-N stretching and N-H bending	[249]
1200-1360	Nucleotides	[249]
1204	Amide III and CH_2 wagging vibrations (glycine backbone and proline side chains)	[249]
	Collagen	[249]
	Tyrosine, phenylalanine (IgG)	[249]
1206	Hydroxyproline, tyrosine	[203, 249]
1208	ν(C-C_6H_5), tryptophan, phenylalanine (protein)	[208, 249]
	A,T (ring breathing modes of DNA/RNA bases) and amide III (protein)	[249]

1209	ν(C-C_6H_5), tryptophan, phenylalanine (protein)	[203, 204, 207, 249]
1210	ν(C-C_6H_5), tyrosine, phenylalanine (protein)	[249]
1216	C-N stretching	[249]
1220	C=N=C stretching	[249]
1220, 1221	Amide III (β-sheet)	[249]
1220-1284	T,A (DNA/RNA)	[204, 249]
	Amide III (protein)	[204, 249]
1223	$\nu(PO_2^-$, nucleic acids	[249]
	Protein	[249]
1224	Amide III (β-sheet)	[249]
1230	Antisymmetric phosphate stretching vibration	[249]
1230-1300	Amide III (protein)	[249]
1235	Amide III (protein)	[249]
1237	Amide III and CH_2 wagging vibrations from glycine backbone and proline side chains	[249]
1239	Amide III	[249]
1240	One of the two most distinct peaks for RNA (with 813cm^{-1})	[249]
	Asymmetric phosphate (PO_2^-) stretching modes	[207, 249]
	Collagen	[249]
1241	Asymmetric phosphate (PO_2^-) stretching modes	[208, 249]
1242	Amide III (β sheet and random coils)	[249]
1243	Amide III	[203, 249]
	Asymmetric phosphate (PO_2^-) stretching modes	[249]
1245	Amide III	[209, 249]
1246	Amide III (collagen)	[208, 249]
1247	Amide III (collagen)	[249]
1247-1248	Guanine, cytosine (NH_2)	[205, 249]
1248	Amide III	[249]
1250	Amide III	[249]
1250-1252	Guanine, cytosine (NH_2)	[205, 249]
1254	C-N in plane stretching	[249]
1255	Lipids	[249]

1257	A,T (ring breathing modes of the DNA/RNA bases) and Amide III (protein)	[249]
1258	Amide III (protein), adenine and cytosine (nucleic acids)	[203, 249]
1259	Guanine, cytosine (NH_2)	[205, 249]
	Amide III (protein)	[249]
1260	Amide III (protein)	[203, 249]
	CH_2 in plane deformation (lipid)	[249]
1263	A,T (ring breathing modes of the DNA/RNA bases) and =C-H bend (protein)	[249]
1263, 1265	Lipids	[249]
1264	Triglycerides (fatty acids)	[249]
1265	Amide III (collagen)	[249]
	ν(CN), δ(NH) amide III, α-helix, collagen	[249]
1266	Amide III (protein, α-helix)	[206, 208, 249]
	ν(CN), δ(NH) amide III, α-helix, collagen, tryptophan	[249]
1267	C-H (lipid)	[249]
	Amide III (collagen)	[249]
1268	δ(=C-H), phospholipids	[249]
1268-1269	Amide III (collagen)	[249]
1270	Phospholipids	[249]
	Amide III (protein)	[249]
	C=C groups in unsaturated fatty acids	[249]
1272-1273	$CH_{\alpha'}$ rocking	[249]
1273	δ(C=CH)	[249]
1275	Amide III	[204, 249]
1278	Proteins	[249]
1279	Amide III (α-helix)	[249]
1280	Amide III and CH_2 wagging vibrations from glycine backbone and proline side chains	[249]
1287-1288	Cytosine	[205, 249]
1288	Phosphodiester groups of nucleic acids	[249]
1290	Cytosine	[205, 249]
1290-1400	CH bending	[205, 249]
1291-1292	Cytosine	[249]
1294	Methylene twisting	[249]

1296	CH_2 deformation	[249]
1297	Palmitic acid	[249]
1298	Palmitic acid	[211, 249]
	Acyl chains	[211, 249]
	Fatty acids	[211, 249]
1299-1300	CH_2 deformation (lipid)	[203, 249]
1300	Lipid	[249]
	Fatty acids	[249]
	$\delta(CH_2)$; lipids, fatty acids	[209, 249]
1301	Triglycerides (fatty acids)	[249]
	$\tau(CH_2)$, lipids	[204, 249]
1302	$\delta(CH_2)$ (protein and lipids)	[206, 249]
	Amide III (protein)	[249]
1303-1304	CH_3, CH_2 twisting (collagen)	[249]
1304	CH_2 deformation (lipid), adenine, cytosine	[203, 249]
1307	CH_3CH_2 twisting, wagging and/or bending mode (collagen/lipid)	[208, 249]
1308	C-N asymmetric stretching in asymmetric aromatic amines	[249]
1309	CH_3CH_2 twisting, wagging and/or bending mode (collagen/lipid)	[208, 249]
1313	CH_3CH_2 twisting mode (collagen/lipid)	[203, 207, 249]
1314	CH_3CH_2 twisting mode (collagen)	[249]
1315	Guanine (B, Z-marker)	[205, 249]
1317-1319	Guanine (B, Z-marker)	[205, 249]
1318	G (ring breathing modes of the DNA/RNA bases) and C-H deformation (protein)	[249]
1319	Guanine (B, Z-marker)	[205, 249]
1320	Guanine (DNA/RNA)	[204, 249]
	CH deformation (proteins)	[204, 249]
1321	Amide III (α-helix)	[249]
	CH_2 deformation of lipids	[212, 249]
1322	CH_3CH_2 twisting (collagen and nucleic acids)	[249]
1323	Guanine (B,Z marker)	[205, 249]
	Ch deformation	[249]
1324	CH_3CH_2 wagging mode (collagen and purine bases)	[249]

1325-1330	CH_3CH_2 wagging mode in purine bases	[249]
1330	Phospholipids	[249]
	DNA and phospholipids	[249]
	Nucleic acids, phosphates, and collagen	[249]
1332	C-C stretch of phenyl	[249]
1333	Guanine	[205, 249]
1335	CH_3CH_2 wagging (collagen, and purine bases)	[206, 207, 249]
1335-1336	Guanine	[205, 249]
1335-1345	CH_3CH_2 wagging (collagen)	[203, 249]
1336	Polynucleotide chain (DNA purine bases)	[203, 249]
	$\delta(CH_3)\delta(CH_2)$ twisting (collagen)	[249]
1337	A,G (ring breathing modes), C-H deformation (protein)	[249]
	Amide III and Ch_2 wagging (glycine backbone, proline sidechain)	[249]
1337,1339	Tryptophan	[208, 249]
	CH_3CH_2 wagging (collagen, lipids, nucleic acid, tryptophan)	[249]
1339	C-C stretch of phenyl	[249]
1340	Nucleic acid mode	[249]
	Collagen	[249]
1341	Adenine, Guanine	[249]
1342	Guanine	[204, 249]
	CH deformation (proteins and carbohydrates)	[204, 249]
1343	CH_3CH_2 wagging (collagen)	[249]
	Glucose	[249]
1343-1344	δ(CH)	[249]
1355,1357	Guanine (B,Z-marker)	[205, 249]
1359	Tryptophan	[249]
1360,1364	Tryptophan	[249]
1361-1363	Guanine (B,Z-marker)	[205, 249]
1365	Tryptophan	[208, 249]
1367	Phospholipids	[249]
1369	Guanine, protein, porphyrins, lipids	[249]
1370	Saccharide	[211, 249]
1371	CH_3	[249]

1373	Thymine, Adenine, Guanine (ring breathing modes)	[249]
1379	δCH_3 symmetric (lipid)	[249]
1383	CH_3	[249]
1386	CH_3	[203, 249]
1391	CH rocking	[249]
1393	CH rocking	[249]
1396	β-carotene	[249]
1398	C=O symmetric stretch	[249]
	CH_2	[208, 249]
1400	NH in=plane deformation	[249]
1400-1430	$\nu(C{=}O)O^-$ (aspartic and glutamic acid)	[209, 249]
1401	CH_3	[249]
1404	CH deformation	[249]
1406,1409	ν_s COO^- (IgG?)	[249]
1417	C=C stretching in quinoid ring	[249]
1420-1421	Deoxyribose (B,Z-marker)	[205, 249]
1420-1450	CH_2 scissoring vibration (lipid)	[249]
1420-1480	Guanine, Adenine	[204, 249]
1421	Guanine, Adenine (ring breathing modes)	[249]
1422	Deoxyribose (B,Z-marker)	[205, 249]
1423	NH in-plane deformation	[249]
1424	Deoxyribose (B,Z-marker)	[205, 249]
1436	CH_2 scissoring	[205, 249]
1437	CH_2 (lipid)	[203, 249]
1437-1453	CH_2 deformation	[249]
1438-1440	Lipid	[249]
1439	CH_2	[249]
1440-1443	CH_2 and CH_3	[203, 211, 249]
1444	Cholesterol band	[249]
1445-1451	CH_2	[203, 207, 208, 249]
1453	Protein bands	[249]
1454	CH_2 and CH_3	[249]
1455	Deoxyribose	[205, 249]
	$\delta(CH_2)$	[249]
1457	Deoxyribose	[205, 249]

1458	Nucleic acid modes	[249]
1459	Deoxyribose	[205, 249]
	$\delta(CH_2)$	[249]
1460	Deoxyribose	[205, 249]
	CH_2 and CH_3	[208, 249]
1462	δCH_2, disaccharides, sucrose	[209, 249]
1465	Lipids	[249]
1470	C=N stretching	[249]
1480-1575	Amide II	[249]
1485	Guanine, Adenine (ring breathing modes)	[203, 249]
1485-1550	NH_3^+	[249]
1487-1488	Guanine	[205, 249]
1488	Collagen	[249]
1490	DNA	[249]
1491	C-N stretching vibration coupled with the in-plane C-H bending in amino acid radical cations	[249]
1499	C-C stretching in benzenoid ring	[249]
1506	N-H bending	[249]
1510	Cytosine	[205, 249]
	Adenine	[249]
1513	Cytosine	[205, 249]
1515	Cytosine	[205, 249]
1517	β-Carotene	[249]
1518	ν(C=C), porphyrin	[206, 249]
1520-1538	-C=C- carotenoids	[249]
1540-1680	Amide carbonyl group	[249]
1544	Amide II	[249]
1545	C_6-H deformation mode	[249]
1546	Bound and free NADH	[249]
	Tryptophan	[249]
1547	Proline	[249]
1548	Tryptophan	[203, 207, 249]
1552	Tryptophan	[206, 249]
1554	Amide II	[249]
1558	Tryptophan	[208, 249]
	Tyrosine	[249]

1560	Tryptophan	[249]
1560-1600	COO^-	[249]
1573	Guanine, Adenine, TRP (protein)	[249]
1575	Guanine, Adenine (ring breathing modes)	[249]
1576	Nucleic acid	[249]
1576,1577	Guanine	[205, 249]
1577	Bound and free NADH	[205, 249]
1578	Guanine, Adenine	[204, 205, 249]
1579	Pyrimidine ring (nucleic acid) and heme protein	[203, 207, 249]
1580	C-C stretching	[249]
	δ(C=C) of phenylalanine	[249]
1582-83	δ(C=C) of phenylalanine	[206, 249]
1585	A and G	[97, 257, 258]
	Cytochrome C	
	C=C olefinic stretch	[249]
1586,1588	Phenylalanine, hydroxyproline	[208, 249]
1593	C=N and C=C stretching in quinoid ring	[249]
1600-1800	Amide I (C=O stretching)	[249]
1602,1603	δ(C=C) of phenylalanine and tyrosine	[203, 206–208, 249]
1605	Cytosine (NH_2)	[249]
1606	δ(C=C)	[249]
1608,1609,1610	Cytosine (NH_2)	[205, 249]
1614	Tyrosine	[208, 249]
1615	Adenine	[207, 249]
	δ(C=C) of tryptophan and tyrosine	[249]
1616	δ(C=C) of tryptophan and tyrosine	[203, 207, 249]
1622,1623	Tryptophan	[208, 249]
1645	Amide I (α-helix)	[249]
1647	Random coils	[249]
1652,1653	Lipid (C=C stretching)	[249]
1653-1655	Lipid	[249]
1655-1680	Thymine, Guanine, Cytosine (ring breathing modes), amide I	[249]
1656	C=C (lipids)	[249]
	Amide I	[249]

1657	Fatty acids	[249]
1658	Amide I (α-helix)	[249]
1662	Nucleic acid	[249]
1663	DNA	[249]
1676	Amide I (β-sheet)	[249]
1678	Bound and free NADH	[249]
1685	Amide I (disordered structure; non-hydrogen bonded)	[249]
1700-1750	ν(C=O)OH (aspartic and glutamic acid)	[249]
1738	Lipids	[249]
1745	Phospholipids	[249]
2095	C-N stretch	[249]
2300-3800	Region of OH-NH-CH stretching vibrations	[249]
2700-3300	C-H stretches	[249]
2700-3500	Stretching vibrations of CH, NH, and OH groups	[211, 249]
2800-3100	CH, CH_2, and CH_3 symmetric and antisymmetric stretching	[249]
3329	N-H vibration of proteins	[249]
3350-3550	O-H stretching	[249]

Table C.1.: *Raman spectral interpretations. Adapted from [249].*

Bibliography

[1] R. Brandstrup Morrish, M. Hermes, J. Metz, N. Stone, S. Pagliara, R. Chahwan, F. Palombo, "Single Cell Imaging of Nuclear Architecture Changes", in *Frontiers in Cell and Developmental Biology* **2019**, *7*, 141, DOI 10.3389/fcell.2019.00141, (cit. on pp. 1, 19, 35, 42, 44, 46, 47, 49, 50, 52, 55, 56, 58, 59, 92).

[2] R. Brandstrup Morrish, K. H. W. Yim, S. Pagliara, F. Palombo, R. Chahwan, N. Stone, "Single cell label-free probing of chromatin dynamics during B lymphocyte activation", in *Frontiers in Cell and Developmental Biology* **2020: in submission**, (cit. on pp. 1, 19, 31, 70, 92).

[3] S. Venkatesh, J. L. Workman, "Histone exchange, chromatin structure and the regulation of transcription", in *Nature Reviews Molecular Cell Biology* **2015**, *16*, 178–189, DOI 10.1038/nrm3941, (cit. on p. 1).

[4] N. Nair, M. Shoaib, C. S. Sørensen, "Chromatin Dynamics in Genome Stability: Roles in Suppressing Endogenous DNA Damage and Facilitating DNA Repair", in *International Journal of Molecular Sciences* **2017**, *18*, 1486–, DOI 10.3390/ijms18071486, (cit. on p. 1).

[5] S.-H. Yang, A. D. Sharrocks, A. J. Whitmarsh, "MAP kinase signalling cascades and transcriptional regulation", in *Gene* **2013**, *513*, 1–13, DOI 10.1016/J.GENE.2012.10.033, (cit. on p. 1).

[6] B. T. MacDonald, K. Tamai, X. He, "Wnt/β-Catenin Signaling: Components, Mechanisms, and Diseases", in *Developmental Cell* **2009**, *17*, 9–26, DOI 10.1016/j.devcel.2009.06.016, (cit. on p. 1).

[7] J. Briscoe, P. P. Thérond, "The mechanisms of Hedgehog signalling and its roles in development and disease", in *Nature Reviews Molecular Cell Biology* **2013**, *14*, 418–431, DOI 10.1038/nrm3598, (cit. on p. 1).

[8] A. Vihervaara, F. M. Duarte, J. T. Lis, "Molecular mechanisms driving transcriptional stress responses", in *Nature Reviews Genetics* **2018**, *19*, 385–397, DOI 10.1038/s41576-018-0001-6, (cit. on p. 1).

[9] E. Sheppard, R. Brandstrup Morrish, M. J. Dillon, R. Leyland, R. Chahwan, "Epigenomic Modifications Meidating Antibody Maturation", in *Frontiers in Immunology* **2018**, *9*, 355, DOI 10.3389/fimmu.2018.00355, (cit. on pp. 2, 3, 6, 7, 72).

[10] P. H. L. Krijger, P. C. M. van den Berk, N. Wit, P. Langerak, J. G. Jansen, C.-A. Reynaud, N. de Wind, H. Jacobs, "PCNA ubiquitination-independent activation of polymerase η during somatic hypermutation and DNA damage tolerance", in *DNA Repair* **2011**, *10*, 1051–1059, DOI 10.1016/j.dnarep.2011.08.005, (cit. on p. 2).

[11] S. Winter, W. Fischle, C. Seiser, "Modulation of 14-3-3 interaction with phosphorylated histone H3 by combinatorial modification patterns", in *Cell Cycle* **2008**, *7*, 1336–1342, DOI 10.4161/cc.7.10.5946, (cit. on p. 2).

[12] P. P. Rocha, R. Raviram, Y. Fu, J. Kim, V. M. Luo, A. Aljoufi, E. Swanzey, A. Pasquarella, A. Balestrini, E. R. Miraldi, R. Bonneau, J. Petrini, G. Schotta, J. A. Skok, "A Damage-Independent Role for 53BP1 that Impacts Break Order and *Igh* Architecture during Class Switch Recombination", in *Cell Reports* **2016**, *16*, 1–8, DOI 10.1016/j.celrep.2016.05.073, (cit. on p. 2).

[13] G. Li, C. A. White, T. Lam, E. J. Pone, D. C. Tran, K. L. Hayama, H. Zan, Z. Xu, P. Casali, "Combinatorial H3K9acS10ph Histone Modification in IgH Locus S Regions Targets 14-3-3 Adaptors and AID to Specify Antibody Class-Switch DNA Recombination", in *Cell Reports* **2013**, *5*, 702–714, DOI 10.1016/j.celrep.2013.09.031, (cit. on pp. 2, 6).

[14] Z. D. Smith, A. Meissner, "DNA methylation: roles in mammalian development", in *Nature Reviews Genetics* **2013**, *14*, 204–220, DOI 10.1038/nrg3354, (cit. on p. 2).

[15] A. Tajik, Y. Zhang, F. Wei, J. Sun, Q. Jia, W. Zhou, R. Singh, N. Khanna, A. D. Belmont, N. Wang, "Transcription upregulation via force-induced direct stretching of chromatin", in *Nature Materials* **2016**, *15*, 1287–1296, DOI 10.1038/nmat4729, (cit. on pp. 2, 9, 13, 52, 93).

[16] A. Méjat, T. Misteli, "LINC complexes in health and disease", in *Nucleus* **2010**, *1*, 40–52, DOI 10.4161/nucl.1.1.10530, (cit. on p. 2).

[17] G. R. Fedorchak, A. Kaminski, J. Lammerding, "Cellular mechanosensing: Getting to the nucleus of it all", in *Progress in Biophysics and Molecular Biology* **2014**, *115*, 76–92, DOI 10.1016/j.pbiomolbio.2014.06.009, (cit. on p. 2).

[18] N. Wang, J. D. Tytell, D. E. Ingber, "Mechanotransduction at a distance: mechanically coupling the extracellular matrix with the nucleus", in *Nature Reviews Molecular Cell Biology* **2009**, *10*, 75–82, DOI 10.1038/nrm2594, (cit. on p. 2).

[19] S. Cho, J. Irianto, D. E. Discher, "Mechanosensing by the nucleus: From pathways to scaling relationships", in *Journal of Cell Biology* **2017**, *216*, 305–315, DOI 10.1083/jcb.201610042, (cit. on p. 2).

[20] Y. A. Miroshnikova, M. M. Nava, S. A. Wickström, "Emerging roles of mechanical forces in chromatin regulation", in *Journal of Cell Science* **2017**, *130*, 2243–2250, DOI 10.1242/jcs.202192, (cit. on pp. 2, 93).

[21] N. Belaadi, J. Aureille, C. Guilluy, "Under Pressure: Mechanical Stress Management in the Nucleus", in *Cells* **2016**, *5*, 27, DOI 10.3390/cells5020027, (cit. on p. 2).

[22] P. Isermann, J. Lammerding, "Nuclear Mechanics and Mechanotranduction in Health and Disease", in *Current Biology* **2013**, *23*, 1113–1121, DOI 10.1016/j.cub.2013.11.009, (cit. on p. 2).

[23] F. Haque, D. J. Lloyd, D. T. Smallwood, C. L. Dent, C. M. Shanahan, A. M. Fry, R. C. Trembath, S. Shackleton, "SUN1 interacts with NUclear Lamin A and Cytoplasmic Nesprins To Provide a Physical Connection between the Nuclear Lamina and the Cytoskeleton", in *Molecular and Cellular Biology* **2006**, *26*, 3738–3751, DOI 10.1128/mcb.26.10.3738-3751.2006, (cit. on p. 2).

[24] J. Schmitt, R. Benavente, D. Hodzic, C. Hø¨, C. L. Stewart, M. Alsheimer, "Transmembrane protein Sun2 is involved in tethering mammalian meiotic telomeres to the nuclear envelope", in *Proceedings of the National Academy of Sciences of the United States of America* **2007**, *104*, 7426–7431, DOI 10.1073/pnas.0609198104, (cit. on p. 2).

[25] Y. Turgay, L. Champion, C. Balazs, M. Held, A. Toso, D. W. Gerlich, P. Meraldi, U. Kutay, "SUN proteins facilitate the removal of membranes from chromatin during nuclear envelope breakdown", in *Journal of Cell Biology* **2014**, *204*, 1099–1109, DOI 10.1083/jcb.201310116, (cit. on p. 2).

[26] J. D. Pajerowski, K. N. Dahl, F. L. Zhong, P. J. Sammak, D. E. Discher, "Physical plasticity of the nucleus in stem cell differentiation", in *Proceedings of the National Academy of Sciences of the United States of America* **2007**, *104*, 15619–15624, DOI 10.1073/pnas.0702576104, (cit. on pp. 2, 13, 14, 93).

[27] J. Lammerding, P. C. Schulze, T. Takahashi, S. Kozlov, T. Sullivan, R. D. Kamm, C. L. Stewart, R. T. Lee, "Lamin A/C deficiency causes defective nuclear mechanics and mechanotransduction", in *Journal of Clinical Investigation* **2004**, *113*, 370–378, DOI 10.1172/JCI200419670, (cit. on pp. 2, 52, 93).

[28] A. T. Bertrand, S. Ziaei, C. Ehret, H. Duchemin, K. Mamchaoui, A. Bigot, M. Mayer, S. Quijano-Roy, I. Desguerre, J. Laine, R. B. Yaou, G. Bonne, C. Coirault, "Cellular microenvironments reveal defective mechanosensing responses and elevated YAP signaling in *LMNA*-mutated muscle precursors", in *Journal of Cell Science* **2014**, *127*, 2873–2884, DOI 10.1242/jcs.144907, (cit. on pp. 2, 93).

[29] M. Cupesi, J. Yoshioka, J. Gannon, A. Kudinova, C. L. Stewart, J. Lammerding, "Attenuated hypertrophic response to pressure overload in a lamin A/C haploinsufficiency mouse", in *Journal of Molecular and Cellular Cardiology* **2010**, *48*, 1290–1297, DOI 10.1016/j.yjmcc.2009.10.024, (cit. on pp. 2, 93).

[30] D. Parra, F. Takizawa, J. O. Sunyer, "Evolution of B Cell Immunity", in *Annual Review of Animal Biosciences* **2013**, *1*, 65–97, DOI 10.1016/j.micinf.2011.07.011.Innate, (cit. on p. 3).

[31] B. Q. Vuong, J. Chaudhuri, "Combinatorial mechanisms regulating AID-dependent DNA deamination: Interacting proteins and post-translational modifications", in *Seminars in Immunology* **2012**, *24*, 264–272, DOI 10.1016/j.smim.2012.05.006, (cit. on p. 3).

[32] K. Johnson, J. Chaumeil, J. A. Skok, "Epigenetic regulation of V(D)J recombination", in *Essays in Biochemistry* **2010**, *48*, 221–243, DOI 10.1042/bse0480221, (cit. on p. 3).

[33] I. Martincorena, P. J. Campbell, "Somatic mutation in cancer and normal cells", in *Science* **2015**, *349*, 1483–1489, DOI 10.1126/science.aab4082, (cit. on p. 3).

[34] S. Kracker, A. Durandy, "Insights into the B cell specific process of immunoglobulin class switch recombination", in *Immunology Letters* **2011**, *138*, 97–103, DOI 10.1016/j.imlet.2011.02.004, (cit. on p. 3).

[35] A. Martin, M. D. Scharff, "AID and mismatch repair in antibody diversification", in *Nature Reviews Immunology* **2002**, *2*, 605–614, DOI 10.1038/nri858, (cit. on p. 5).

[36] K. Basso, R. Dalla-Favera, "Germinal centres and B cell lymphomagenesis", in *Nature Reviews Immunology* **2015**, *15*, 172–184, DOI 10.1038/nri3814, (cit. on pp. 5, 8, 9).

[37] K.-M. Schmitz, S. K. Petersen-Mahrt, "AIDing the immune system - DIAbolic in cancer", in *Seminars in Immunology* **2012**, *24*, 241–245, DOI 10.1016/j.smim.2012.07.001, (cit. on p. 5).

[38] V. H. Odegard, D. G. Schatz, "Targeting of somatic hypermutation", in *Nature Reviews Immunology* **2006**, *6*, 573–583, DOI 10.1038/nri1896, (cit. on p. 5).

[39] J. U. Peled, F. L. Kuang, M. D. Iglesias-Ussel, S. Roa, S. L. Kalis, M. F. Goodman, M. D. Scharff, "The Biochemistry of Somatic Hypermutation", in *Annual review of Immunology* **2008**, *26*, 481–511, DOI 10.1146/annurev.immunol.26.021607.090236, (cit. on p. 5).

[40] J. M. Di Noia, M. S. Neuberger, "Molecular Mechanisms of Antibody Somatic Hypermutation", in *Annual review of biochemistry* **2007**, *76*, 1–22, DOI 10.1146/annurev.biochem.76.061705.090740, (cit. on p. 5).

[41] S. K. Dickerson, E. Market, E. Besmer, F. N. Papavasiliou, "AID Mediates Hypermutation by Deaminating Single Stranded DNA", in *The journal of experimental medicine* **2003**, *197*, 1291–1296, DOI 10.1084/jem.20030481, (cit. on p. 5).

[42] M. Wiesendanger, B. Kneitz, W. Edelmann, M. D. Scharff, "Somatic Hypermutation in MutS Homologue (MSH)3-, MSH6-, and MSH6-deficient Mice Reveals a Role for the MSH2-MSH6 Heterodimer in Modulating the Base Substitution Pattern", in *The journal of experimental medicine* **2000**, *191*, 579–584, DOI 10.1084/jem.191.3.579, (cit. on p. 5).

[43] C. Rada, M. R. Ehrenstein, M. S. Neuberger, C. Milstein, "Hot Spot Focusing of Somatic Hypermutation in MSH2-Deficient Mice Suggests Two Stages of Mutational Targeting", in *Immunity* **1998**, *9*, 135–141, DOI 10.1016/S1074-7613(00)80595-6, (cit. on p. 5).

[44] D. Frieder, M. Larijani, C. Collins, M. Shulman, A. Martin, "The Concerted Action of Msh2 and UNG Stimulates Somatic Hypermutation at A T Base Pairs", in *Molecular and cellular biology* **2009**, *29*, 5148–5157, DOI 10.1128/MCB.00647-09, (cit. on p. 5).

[45] H. Saribasak, D. Rajagopal, R. W. Maul, P. J. Gearhart, "Hijacked DNA repair proteins and unchained DNA polymerases", in *Philosophical transactions of the Royal Society of London. Series B Biological Sciences* **2009**, *364*, 605–611, DOI 10.1098/rstb.2008.0188, (cit. on p. 5).

[46] K. Kinoshita, J. Tashiro, S. Tomita, C.-G. Lee, T. Honjo, "Target Specificity of Immunoglobulin Class Switch Recombination Is Not Determined by Nucleotide Sequences of S Regions", in *Immunity* **1998**, *9*, 849–858, DOI 10.1016/S1074-7613(00)80650-0, (cit. on p. 5).

[47] D. Carter, L. Chakalova, C. S. Osborne, Y.-f. Dai, P. Fraser, "Long-range chromatin regulatory interactions in vivo", in *Nature genetics* **2002**, *32*, 623–626, DOI 10.1038/ng1051, (cit. on p. 5).

[48] R. Wuerffel, L. Wang, F. Grigera, J. Manis, E. Selsing, T. Perlot, F. W. Alt, M. Cogne, E. Pinaud, A. L. Kenter, "S-S synapsis during class switch recombination is promoted by distantly located transcriptional elements and activation-induced deaminase", in *Immunity* **2007**, *27*, 711–722, DOI 10.1016/j.immuni.2007.09.007, (cit. on p. 5).

[49] A. L. Kenter, "AID targeting is dependent on RNA polymerase II pausing", in *Seminars in Immunology* **2012**, *24*, 281–286, DOI 10.1016/j.smim.2012.06.001, (cit. on p. 5).

[50] J. Chaudhuri, F. W. Alt, "Class-switch recombination: interplay of transcription, DNA deamination and DNA repair", in *Nature Reviews Immunology* **2004**, *4*, 541–552, DOI 10.1038/nri1395, (cit. on p. 6).

[51] R. Chahwan, W. Edelmann, M. D. Scharff, S. Roa, "Mismatch-mediated error prone repair at the immunoglobulin genes", in *Biomedicine and Pharmacotherapy* **2011**, *65*, 529–536, DOI 10.1016/j.biopha.2011.09.001, (cit. on p. 6).

[52] S. Zheng, B. Q. Vuong, B. Vaidyanathan, J.-Y. Lin, F.-T. Huang, J. Chaudhuri, "Non-coding RNA Generated following Lariat Debranching Mediates Targeting of AID to DNA", in *Cell* **2015**, *161*, 762–773, DOI 10.1016/j.cell.2015.03.020, (cit. on pp. 6, 72).

[53] N. A. Begum, A. Stanlie, M. Nakata, H. Akiyama, T. Honjo, "The Histone Chaperone Spt6 Is Required for Activation-induced Cytidine Deaminase Target Determination through H3K4me3 Regulation", in *Journal of Biological Chemistry* **2012**, *287*, 32415–32429, DOI 10.1074/jbc.M112.351569, (cit. on p. 6).

[54] A. Stanlie, N. A. Begum, H. Akiyama, T. Honjo, "The DSIF Subunits Spt4 and Spt5 Have Distinct Roles at Various Phases of Immunoglobulin Class Switch Recombination", in *PLoS Genetics* **2012**, *8*, e1002675, DOI 10.1371/journal.pgen.1002675, (cit. on p. 6).

[55] A. Stanlie, M. Aida, M. Muramatsu, T. Honjo, N. Begum, "Histone3 Lysine4 trimethylation regulated by the facilitates chromatin transcription complex is critical for DNA cleavage in class switch recombination", in *Proceedings of the National Academy of Sciences of the United States of America* **2010**, *107*, 22190–22195, DOI 10.1073/pnas.1016923108, (cit. on pp. 6, 72).

[56] F. L. Kuang, Z. Luo, M. D. Scharff, "H3 trimethyl K9 and H3 acetyl K9 chromatin modifications are associated with class switch recombination", in *Proceedings of the National Academy of Sciences of the United States of America* **2009**, *106*, 5288–5293, DOI 10.1073/pnas.0901368106, (cit. on p. 6).

[57] A. Franklin, P. J. Milburn, R. V. Blanden, E. J. Steele, "Human DNA polymerase-η, an A-T mutator in somatic hypermutations of rearranged immunoglobulin genes, is a reverse transcriptase", in *Immunology and Cell Biology* **2004**, *82*, 219–225, DOI 10.1046/j.0818-9641.2004.01221.x, (cit. on p. 6).

[58] G. M. Borchert, N. W. Holton, K. A. Edwards, L. A. Vogel, E. D. Larson, "Histone H2A and H2B Are Monoubiquitinated at AID-Targeted Loci", in *PloS One* **2010**, *5*, e11641, DOI 10.1371/journal.pone.0011641, (cit. on p. 6).

[59] P. L. Kannouche, J. Wing, A. R. Lehmann, "Interaction of Human DNA Polymerase η with Monoubiquitinated PCNA: A Possible Mechanism for the Polymerase Switch in Response to DNA Damage", in *Molecular Cell* **2004**, *14*, 491–500, DOI 10.1016/S1097-2765(04)00259-X, (cit. on p. 6).

[60] B. S. Plosky, A. E. Vidal, A. R. Fernández de Henestrosa, M. P. McLenigan, J. P. McDonald, S. Mead, R. Woodgate, "Controlling the subcellular localization of DNA polymerases ι and η via interactions with ubiquitin", in *The EMBO Journal* **2006**, *25*, 2847–2855, DOI 10.1038/sj.emboj.7601178, (cit. on p. 6).

[61] A. T. Noon, A. A. Goodarzi, "53BP1-mediated DNA double strand break repair: Insert bad pun here", in *DNA Repair* **2011**, *10*, 1071–1076, DOI 10.1016/j.dnarep.2011.07.012, (cit. on p. 6).

[62] J. P. Manis, J. C. Morales, Z. Xia, J. L. Kutok, F. W. Alt, P. B. Carpenter, "53BP1 links DNA damage-response pathways to immunoglobulin heavy chain class-switch recombination", in *Nature Immunology* **2004**, *5*, 481–487, DOI 10.1038/ni1067, (cit. on p. 6).

[63] A. Stanlie, A. S. Yousif, H. Akiyama, T. Honjo, N. A. Begum, "Chromatin Reader Brd4 Functions in Ig Class Switching as a Repair Complex Adaptor of Nonhomologous End-Joining", in *Molecular Cell* **2014**, *55*, 97–110, DOI 10.1016/j.molcel.2014.05.018, (cit. on p. 8).

[64] S. Ramachandran, R. Chahwan, R. M. Nepal, D. Frieder, S. Panier, S. Roa, A. Zaheen, D. Durocher, M. D. Scharff, A. Martin, "The RNF8/RNF168 ubiquitin ligase cascade facilitates class switch recombination", in *Proceedings of the National Academy of Sciences of the United States of America* **2010**, *107*, 809–814, DOI 10.1073/pnas.0913790107, (cit. on p. 8).

[65] M. Lunning, G. MR, "Mutation of chromatin modifiers; an emerging hallmark of germinal center B-cell lymphomas", in *Blood cancer journal* **2015**, *5*, e361, DOI 10.1038/bcj.2015.89, (cit. on p. 8).

[66] B. G. T. Pogo, V. G. Allfrey, A. E. Mirsky, "RNA synthesis and histone acetylation during the course of gene activation in lymphocytes", in *Proceedings of the National Academy of Sciences of the United States of America* **1966**, *55*, 805, DOI 10.1073/pnas.55.4.805, (cit. on pp. 8, 43).

[67] A. Zaheen, A. Martin, "Induction and Assessment of Class Switch Recombination in Purified Murine B Cells", in *Journal of Visualized Experiments* **2010**, 6–8, DOI 10.3791/2130, (cit. on p. 8).

[68] J. Liu, E. Xiong, Z. Zhu, Hanying, H. Mori, S. Yasuda, K. Kinoshita, T. Tsubata, J.-Y. Wang, "Efficient Induction of Ig Gene Hypermutation in Ex Vivo-Activated Primary B cells", in *The Journal of Immunology* **2017**, *199*, 3023–3030, DOI 10.4049/jimmunol.1700868, (cit. on p. 8).

[69] A. Cerutti, H. Zan, A. Schaffer, L. Bergsagel, N. Harindranath, E. E. Max, P. Casali, "CD40 Ligand and Appropriate Cytokines Induce Switching to IgG, IgA, and IgE and Coordinated Germinal Center and Plasmacytoid Phenotypic Differentiation in a Human Monoclonal IgM+IgD+ B Cell Line", in *Journal of Immunology* **1998**, *160*, 2145–2157, (cit. on p. 8).

[70] M. L. Squadrito, C. Baer, F. Burdet, C. Maderna, G. D. Gilfillan, R. Lyle, M. Ibberson, M. De Palma, "Endogenous RNAs Modulate MicroRNA Sorting to Exosomes and Transfer to Acceptor Cells", in *Cell Reports* **2014**, *8*, 1432–1446, DOI 10.1016/j.celrep.2014.07.035, (cit. on p. 9).

[71] M. Turner, A. Galloway, E. Vigorito, "Noncoding RNA and its associated proteins as regulatory elements of the immune system", in *Nature Immunology* **2014**, *15*, 484–491, DOI 10.1038/ni.2887, (cit. on p. 9).

[72] A. Montecalvo et al., "Mechanism of transfer of functional microRNAs between mouse dendritic cells via exosomes", in *Blood* **2012**, *119*, 756–766, DOI 10.1182/blood-2011-02-338004, (cit. on p. 9).

[73] D. L. Hardie, G. D. Johnson, M. Khan, I. C. M. MacLennan, "Quantitative analysis of molecules which distinguish compartments within germinal centers", in *European Journal of Immunology* **1993**, *23*, 997–1004, DOI 10.1002/eji.1830230502, (cit. on p. 9).

[74] Z. Wan, X. Chen, H. Chen, Q. Ji, Y. Chen, J. Wang, Y. Cao, F. Wang, J. Lou, Z. Tang, W. Liu, "The activation of IgM- or isotype-switched IgG- and IgE-BCR exhibits distinct mechanical force sensitivity and threshold", in *eLife* **2015**, *4*, 1–24, DOI 10.7554/eLife.06925, (cit. on pp. 9, 94, 95).

[75] R. Basu, B. M. Whitlock, J. Husson, A. Le Floc'h, W. Jin, A. Oyler-Yaniv, F. Dotiwala, G. Giannone, C. Hivroz, N. Biais, J. Lieberman, L. C. Kam, M. Huse, "Cytotoxic T Cells Use Mechanical Force to Potentiate Target Cell Killing", in *Cell* **2016**, *165*, 100–110, DOI 10.1002/eji.1830230502, (cit. on p. 9).

[76] M. Versaevel, T. Grevesse, S. Gabriele, "Spatial coordination between cell and nuclear shape within micropatterned endothelial cells", in *Nature Communications* **2012**, *3*, 671, DOI 10.1038/ncomms1668, (cit. on p. 9).

[77] S. Boydston-White, T. Gopen, S. Houser, J. Bargonetti, M. Diem, "Infrared spectroscopy of human tissue. V. Infrared spectroscopic studies of myeloid leukemia (ML-1) cells at different phases of the cell cycle", in *Biospectroscopy* **1999**, *5*, 219–227, DOI 10.1002/(SICI)1520-6343(1999)5, (cit. on p. 10).

[78] H.-Y. N. Holman, M. C. Martin, W. R. McKinney, "Tracking chemical changes in a live cell: Biomedical applications of SR-FTIR spectromicroscopy", in *Spectroscopy* **2003**, *17*, 139–159, DOI 10.1155/2003/486940, (cit. on p. 10).

[79] K. W. Short, S. Carpenter, J. P. Freyer, J. R. Mourant, "Raman Spectroscopy Detects Biochemical Changes Due to Proliferation in Mammalian Cell Cultures", in *Biophysical Journal* **2005**, *88*, 4274–4288, DOI 10.1529/biophysj.103.038604, (cit. on p. 10).

[80] R. J. Swain, G. Jell, M. M. Stevens, "Non-Invasive Analysis of Cell Cycle Dynamics in Single Living Cells With Raman Micro-Spectroscopy", in *Journal of Cellular Biochemistry* **2008**, *104*, 1427–1438, DOI 10.1002/jcb.21720, (cit. on p. 10).

[81] A. D. Meade, C. Clarke, F. Draux, G. D. Sockalingum, M. Manfait, F. M. Lyng, H. J. Byrne, "Studies of chemical fixation effects in human cell lines using Raman microspectroscopy", in *Analytical and Bioanalytical Chemistry* **2010**, *396*, 1781–1791, DOI 10.1007/s00216-009-3411-7, (cit. on pp. 10, 12).

[82] E. Lipiec, G. Birarda, J. Kowalska, J. Lekki, L. Vaccari, A. Wiechec, B. R. Wood, W. M. Kwiatak, "A new approach to studying the effects of ionising radiation on single cells using FTIR synchrotron microspectroscopy", in *Radiation Physics and Chemistry* **2013**, *93*, 135–141, DOI 10.1016/j.radphyschem.2013.03.037, (cit. on p. 10).

[83] E. Lipiec, K. R. Bambery, P. Heraud, C. Hirschmugl, J. Lekki, W. M. Kwiatek, M. J. Tobin, C. Vogel, D. Whelan, B. R. Wood, "Synchrotron FTIR shows evidence of DNA damage and lipid accumulation in prostate adenocarcinoma PC-3 cells following proton irradiation", in *Journal of Molecular Structure* **2014**, *1073*, 134–141, DOI 10.1016/j.molstruc.2014.04.056, (cit. on p. 10).

[84] E. Lipiec, K. R. Bambery, P. Heraud, W. M. Kwiatek, D. McNaughton, M. J. Tobin, C. Vogel, B. R. Wood, "Monitoring UVR induced damage in single cells and isolated nuclei using SR-FTIR microspectroscopy and 3D confocal Raman imaging", in *The Analyst* **2014**, *139*, 4200–4209, DOI 10.1039/c4an00838c, (cit. on p. 10).

[85] G. I. Dovbeshko, N. Y. Gridina, E. B. Kruglova, O. P. Pashchuk, "FTIR spectroscopy studies of nucleic acid damage", in *Talanta* **2000**, *53*, 233–246, DOI 10.1016/s0039-9140(00)00462-8, (cit. on p. 10).

[86] T. Chen, M. J. Lee, S. K. Yeong, S. Lee, S. Kummar, M. Gutierrez, S. M. Hewitt, J. B. Trepel, I. W. Levin, "Pharmacodynamic assessment of histone deacetylase inhibitors: Infrared vibrational spectroscopic imaging of protein acetylation", in *Analytical Chemistry* **2008**, *80*, 6390–6396, DOI 10.1021/ac800840y, (cit. on p. 10).

[87] F. Zhang, Q. Huang, J. Yan, X. Zhang, J. Li, "Assessment of the effect of trichostatin a on hela cells through FT-IR spectroscopy", in *Analytical Chemistry* **2015**, *87*, 2511–2517, DOI 10.1021/ac504691q, (cit. on p. 10).

[88] B. R. Wood, B. Tait, D. McNaughton, "Fourier-transform infrared spectroscopy as a tool for detecting early lymphocyte activation: A new approach to histocompatibility matching", in *Human Immunology* **2000**, *61*, 1307–1315, DOI 10.1016/S0198-8859(00)00164-6, (cit. on pp. 10, 11).

[89] B. Wood, B. Tait, D. M. C. Naughton, "Fourier Transform Infrared Spectroscopy as a Method for Monitoring the Molecular Dynamics of Lymphocyte Activation", in *Applied Spectroscopy Vol. 54 Issue 3 pp. 353-359* **2000**, *54*, 353–359, (cit. on pp. 10, 11).

[90] K. L. Brown, O. Y. Palyvoda, J. S. Thakur, S. L. Nehlsen-Cannarella, O. R. Fagoaga, S. A. Gruber, G. W. Auner, "Differentiation of alloreactive versus CD3/CD28 stimulated T-lymphocytes using Raman spectroscopy: A greater specificity for noninvasive acute renal allograft rejection detection", in *Cytometry Part A* **2009**, *75*, 917–923, DOI 10.1002/cyto.a.20797, (cit. on p. 10).

[91] A. B. Zoladek, R. K. Johal, S. Garcia-Nieto, F. Pascut, K. M. Shakesheff, A. M. Ghaemmaghami, I. Notingher, "Label-free molecular imaging of immunological synapses between dendritic and T cells by Raman micro-spectroscopy", in *Analyst* **2010**, *135*, 3205–3212, DOI 10.1039/c0an00508h, (cit. on p. 10).

[92] Z. J. Smith, J.-C. E. Wang, S. A. Quataert, A. J. Berger, "Integrated Raman and angular scattering microscopy reveals chemical and morphological differences between activated and nonactivated CD8+ T lymphocytes", in *Journal of Biomedical Optics* **2010**, *15*, 036021, DOI 10.1117/1.3443794, (cit. on p. 10).

[93] V. V. Pully, A. T. M. Lenferink, C. Otto, "Time-lapse Raman imaging of single live lymphocytes", in *Journal of Raman Spectroscopy* **2011**, *42*, 167–173, DOI 10.1002/jrs.2683, (cit. on p. 10).

[94] A. I. Mazur, J. L. Monahan, M. Miljkovi, N. Laver, M. Diem, B. Bird, "Vibrational spectroscopic changes of B-lymphocytes upon activation", in *Journal of Biophotonics* **2013**, *6*, 101–109, DOI 10.1002/jbio.201200136, (cit. on pp. 10, 11).

[95] A. J. Hobro, N. Pavillon, K. Fujita, M. Ozkan, C. Coban, N. I. Smith, "Label-free Raman imaging of the macrophage response to the malaria pigment hemozoin", in *Analyst* **2015**, *140*, 2350–2359, DOI 10.1039/c4an01850h, (cit. on p. 10).

[96] T. Ichimura, L.-d. Chiu, K. Fujita, H. Machiyama, T. Yamaguchi, T. M. Wantanabe, H. Fujita, "Non-label immune cell state prediction using Raman spectroscopy", in *Scientific Reports* **2016**, *6*, 37562, DOI 10.1038/srep37562, (cit. on pp. 10, 11).

[97] A. J. Hobro, Y. Kumagai, S. Akira, N. I. Smith, "Raman spectroscopy as a tool for label-free lymphocyte cell line discrimination", in *Analyst* **2016**, *141*, 3756–3764, DOI 10.1039/c6an00181e, (cit. on pp. 10, 125).

[98] N. Pavillon, A. J. Hobro, S. Akira, N. I. Smith, "Noninvasive detection of macrophage activation with single-cell resolution through machine learning", in *Proceedings of the National Academy of Sciences of the United States of America* **2018**, *115*, E2676–E2685, DOI 10.1073/pnas.1711872115, (cit. on pp. 10, 11).

[99] A. Ramoji, U. Neugebauer, T. Bocklitz, M. Foerster, M. Kiehntopf, M. Bauer, J. Popp, "Toward a spectroscopic hemogram: Raman spectroscopic differentiation of the two most abundant leukocytes from peripheral blood", in *Analytical Chemistry* **2012**, *84*, 5335–5342, DOI 10.1021/ac3007363, (cit. on p. 10).

[100] A. Maguire, I. Vega-Carrascal, J. Bryant, L. White, O. Howe, F. M. Lyng, A. D. Meade, "Competitive evaluation of data mining algorithms for use in classification of leukocyte subtypes with Raman microspectroscopy", in *Analyst* **2015**, *140*, 2473–2481, DOI 10.1039/c4an01887g, (cit. on p. 10).

[101] A. Germond, T. Ichimura, T. Horinouchi, H. Fujita, C. Furusawa, T. M. Watanabe, "Raman spectral signature reflects transcriptomic features of antibiotic resistance in Escherichia coli", in *Communications Biology* **2018**, *1*, 3205–3212, DOI 10.1039/c0an00508h, (cit. on p. 11).

[102] K. J. Kobayashi-Kirschvink, H. Nakaoka, A. Oda, K.-i. F. Kamei, K. Nosho, H. Fukushima, Y. Kanesaki, S. Yajima, H. Masaki, K. Ohta, Y. Wakamoto, "Linear regression links transcriptomic data and cellular Raman spectra", in *Cell Systems* **2018**, *7*, 104–117, DOI 10.1016/j.cels.2018.05.015, (cit. on pp. 11, 12, 70, 80, 86, 100).

[103] P. Heraud, K. M. Marzec, Q.-H. Zhang, W. S. Yuen, J. Carroll, B. R. Wood, "Label-free *in vivo* Raman microspectroscopic imaging of the macromolecular architecture of oocytes", in *Scientific Reports* **2017**, *7*, 31–34, DOI 10.1038/s41598-017-08973-0, (cit. on p. 12).

[104] A. N. Kuzmin, A. Pliss, P. N. Prasad, "Changes in Biomolecular Profile in a Single Nucleolus during Cell Fixation", in *Analytical Chemistry* **2014**, *86*, 10909–10916, DOI 10.1021/ac503172b, (cit. on p. 12).

[105] F. Draux, C. Gobinet, J. Sul´-Suso, A. Trussardi, M. Manfait, P. Jeannesson, G. D. Sockalingum, "Raman spectral imaging of single cancer cells: probing the impact of sample fixation methods", in *Analytical and Bioanalytical Chemistry* **2010**, *397*, 2727–2737, DOI 10.1007/s00216-010-3759-8, (cit. on p. 12).

[106] J. W. Chan, D. S. Taylor, D. L. Thompson, "The Effect of Cell Fixation on the Discrimination of Normal and Leukemia Cells with Laser Tweezers Raman Spectroscopy", in *Biopolymers* **2009**, *91*, 132–139, DOI 10.1002/bip.21094, (cit. on p. 12).

[107] K. L. A. Chan, S. G. Kazarian, "Attenuated total reflection Fourier-transform infrared (ATR-FTIR) imaging of tissues and live cells", in *Chemical Society Reviews* **2015**, *45*, 1850–1864, DOI 10.1039/C5CS00515A, (cit. on p. 12).

[108] P. L. Fale, A. Altharawi, K. L. A. Chan, "*In situ* Fourier transform infrared analysis of live cells'n response to doxorubicin", in *Biochimica et Biophysica Acta - Molecular Cell Research* **2015**, *1853*, 2640–2648, DOI 10.1016/j.bbamcr.2015.07.018, (cit. on p. 12).

[109] A. Altharawi, K. M. Rahman, K. L. A. Chan, "Towards identifying the mode of action of drugs using live-cell FTIR spectrocopy", in *Analyst* **2019**, *144*, 2725–2735, DOI 10.1039/c8an02218f, (cit. on p. 12).

[110] J. Phelan, A. Altharawi, K. L. A. Chan, "Tracking glycosylation in live cells using FTIR spectroscopy", in *Talanta* **2020**, *211*, 120737, DOI 10.1016/j.talanta.2020.120737, (cit. on p. 12).

[111] D. R. Whelan, K. R. Bambery, L. Puskar, D. McNaughton, B. R. Wood, "Synchrotron Fourier transform infrared (FTIR) analysis of single living cells progressing through the cell cycle", in *The Analyst* **2013**, *138*, 3891, DOI 10.1039/c3an00316g, (cit. on pp. 13, 61, 68).

[112] K. L. A. Chan, P. L. V. Fale, A. Atharawi, K. Wehbe, G. Cinque, "Subcellular mapping of living cells via synchrotron microFTIR and ZnS hemispheres", in *Analytical and Bioanalytical Chemistry* **2018**, *410*, 6477–6487, DOI 10.1007/s00216-018-1245-x, (cit. on pp. 13, 61, 68).

[113] K. L. A. Chan, A. Altharawi, P. Fale, C. L. Song, S. G. Kazarian, G. Cinque, V. Untereiner, G. D. Sockalingum, "Transmission Fourier Transform Infrared (FT-IR) Imaging, Mapping, and Synchrotron Scanning Microscopy with ZnS Hemispheres on Living Mammalian Cells at Sub-Cellular Resolution", in *Applied Spectroscopy* **2020**, *74*, 544–552, DOI 10.1177/0003702819898275, (cit. on pp. 13, 61, 68).

[114] E. J. (Swain) Marcsisin, C. M. Uttero, M. Miljković, M. Diem, "Infrared microspectroscopy of live cells in aqueous media", in *The Analyst* **2010**, *135*, 3227, DOI 10.1039/c0an00548g, (cit. on pp. 13, 61, 68).

[115] M. J. Tobin, L. Puskar, R. L. Barber, E. C. Harvey, P. Heraud, B. R. Wood, K. R. Bambery, C. T. Dillon, K. L. Munro, "FTIR spectroscopy of single live cells in aqueous media by synchrotron IR microscopy using microfabricated sample holders", in *Vibrational Spectroscopy* **2010**, *53*, 34–38, DOI 10.1016/j.vibspec.2010.02.005, (cit. on pp. 13, 61, 68).

[116] K. L. A. Chan, S. G. Kazarian, "Aberration-free FTIR spectroscopic imaging of live cells in microfluidic devices", in *The Analyst* **2013**, *138*, 4040, DOI 10.1039/c3an00327b, (cit. on pp. 13, 61, 68).

[117] E. Mitri, G. Birarda, L. Vaccari, S. Kenig, M. Tormen, G. Grenci, "SU-8 bonding protocol for the fabrication of microfluidic devices dedicated to FTIR microspectroscopy of live cells.", in *Lab on a chip* **2014**, *14*, 210–8, DOI 10.1039/c3lc50878a, (cit. on pp. 13, 61, 68).

[118] E. Mitri, A. Pozzato, G. Coceano, D. Cojoc, L. Vaccari, M. Tormen, G. Grenci, "Highly IR-transparent microfluidic chip with surface-modified BaF 2 optical windows for Infrared Microspectroscopy of living cells", in *Microelectronic Engineering* **2013**, *107*, 6–9, DOI 10.1016/j.mee.2013.02.068, (cit. on pp. 13, 61, 68).

[119] R. Smith, K. L. Wright, L. Ashton, "Raman spectroscopy: an evolving technique for live cell studies", in *Analyst* **2016**, *141*, 3590–3600, DOI 10.1039/c6an00152a, (cit. on pp. 13, 37, 61, 68).

[120] G. J. Puppels, J. H. F. Olminkhop, G. M. J. Segers-Nolten, C. Otto, F. F. M. De Mul, J. Greve, "Laser Irradiation and Raman Spectroscopy of Single Living Cells and Chromosomes: Sample Degradation Occurs with 514.5 nm but not with 660 nm Laser Light", in *Experimental Cell Research* **1991**, *195*, 361–367, DOI 10.1016/0014-4827(91)90385-8, (cit. on p. 13).

[121] B. R. Wood, L. Hammer, L. Davis, D. McNaughton, "Raman microspectroscopy and imaging provides insights into heme aggregation and denaturation within human erythrocytes", in *Journal of Biomedical Optics* **2005**, *10*, 014005, DOI 10.1117/1.1854678, (cit. on p. 13).

[122] E. M. Darling, D. Di Carlo, "High-Throughput Assessment of Cellular Mechanical Properties", in *Annual Review of Biomedical Engineering* **2015**, *17*, 35–62, DOI 10.1146/annurev-bioeng-071114-040545, (cit. on pp. 13, 14).

[123] H. Liu, J. Wen, Y. Xiao, S. Hopyan, M. Radisic, C. A. Simmons, Y. Sun, "emphIn Situ Mechanical Characterization of the Cell Nucleus by Atomic Force Microscopy", in *ACS Nano* **2014**, *8*, 3821–3828, DOI 10.1021/nn500553z, (cit. on p. 13).

[124] S. Pagliara, K. Franze, C. R. McClain, G. W. Wylde, C. L. Fisher, R. J. Franklin, A. J. Kabla, U. F. Keyser, K. J. Chalut, "Auxtic nuclei in embryonic stem cells exiting pluripotency", in *Nature Materials* **2014**, *13*, 638–644, DOI 10.1038/nmat3943, (cit. on pp. 13, 15, 20, 52, 57, 60, 92, 94).

[125] O. Otto et al., "Real-time deformability cytometry: on-the-fly cell mechanical phenotyping", in *Nature methods* **2015**, *12*, 199–202, DOI 10.1038/nmeth.3281, (cit. on pp. 13, 14, 61).

[126] J. Zhang, X. A. Nou, H. Kim, G. Scarcelli, "Brillouin flow cytometry for label-free mechanical phenotyping of the nucleus", in *Lab on a Chip* **2017**, *17*, 663–670, DOI 10.1039/C6LC01443G, (cit. on pp. 13, 14, 101).

[127] J. Guck, "Some thoughts on the future of cell mechanics", in *Biophysical Reviews* **2019**, *11*, 667–670, DOI 10.1007/s12551-019-00597-0, (cit. on p. 13).

[128] C. Guilluy, L. D. Osborne, L. Van Landeghem, L. Sharek, R. Superfine, R. Garcia-Mata, K. Burridge, "Isolated nuclei adapt to force and reveal a mechanotransduction pathway in the nucleus", in *Nature Cell Biology* **2014**, *16*, 376–381, DOI 10.1038/ncb2927, (cit. on p. 13).

[129] M. Lherbette, A. dos Santos, Y. Hari-Gupta, N. Fili, C. P. Toseland, I. A. T. Schaap, "Atomic Force Microscopy micro-rheology reveals large structural inhomogeneities in single cell-nuclei", in *Scientific Reports* **2017**, *7*, 1–13, DOI 10.1038/s41598-017-08517-6, (cit. on p. 13).

[130] K. J. Chalut, M. Höpfler, F. Lautenschläger, L. Boyde, C. Jou Chan, A. Ekpenyong, A. Martinez-Arias, J. Guck, "Chromatin Decondensation and Nuclear Softening Accompagny Nanog Downregulaton in Embryonic Stem Cells", in *Biophysical Journal* **2012**, *103*, 2060–2070, DOI 10.1016/j.bpj.2012.10.015, (cit. on pp. 13, 14).

[131] M. Krause, J. te Riet, K. Wolf, "Probing the compressibility of tumor cell nuclei by combined atomic force-confocal microscopy", in *Physical Biology* **2013**, *10*, 065002, DOI 10.1088/1478-3975/10/6/065002, (cit. on pp. 13, 14).

[132] E. K. Sackmann, A. L. Fulton, D. J. Beebe, "The present and future role of microfluidics in biomedical research", in *Nature* **2014**, *507*, 181–189, DOI 10.1038/nature13118, (cit. on p. 14).

[133] G. M. Whitesides, "The origins and the future of microfluidics", in *Nature* **2006**, *442*, 368–373, DOI 10.1038/nature05058, (cit. on p. 14).

[134] G. M. Whitesides, "Cool, or simple and cheap? Why not both?", in *Lab on a Chip* **2013**, *13*, 11–13, DOI 10.1039/C2LC90109A, (cit. on p. 14).

[135] M. Junkin, S. Tay, "Microfluidic single-cell analysis for systems immunology", in *Lab on a Chip* **2014**, *7*, 1246–1260, DOI 10.1039/C3LC51182K, (cit. on p. 14).

[136] T. Bergmiller, A. M. C. Andersson, K. Tomasek, E. Balleza, D. J. Kiviet, R. Hauschild, G. Tkacik, C. C. Guet, "Biased partitioning of the multidrug efflux pump AcrAB-TolC underlies long-lived phenotypic heterogeneity", in *Science* **2017**, *356*, 311–315, DOI 10.1126/science.aaf4762, (cit. on p. 14).

[137] R. Chait, J. Ruess, T. Bergmiller, G. Tkacik, C. C. Guet, "Shaping bacterial population behavior through computer-interfaced control of individual cells", in *Nature Communications* **2017**, *8*, 1–11, DOI 10.1038/s41467-017-01683-1, (cit. on p. 14).

[138] U. Łapińska, G. Glover, P. Capilla-Lasheras, A. J. Young, S. Pagliara, "Bacterial ageing in the absence of external stressors", in *Philosophical Transactions of the Royal Society B: Biological Sciences* **2019**, *374*, 1–13, DOI 10.1098/rstb.2018.0442, (cit. on p. 14).

[139] J. Cama, M. Voliotis, J. Metz, A. Smith, J. Iannucci, U. F. Keyser, K. Tsaneva-Atanasova, S. Pagliara, "Single-cell microfluidics facilitates the rapid quantification of antibiotic accumulation in Gram-negative bacteria", in *Lab on a Chip* **2020**, *20*, 2765–2775, DOI 10.1039/d0lc00242a, (cit. on p. 14).

[140] A. E. Ekpenyong, G. Whyte, K. Chalut, S. Pagliara, F. Lautenschläger, C. Fiddler, S. Paschke, U. F. Keyser, E. R. Chilvers, J. Guck, "Viscoelastic Properties of Differentiating Blood Cells Are Fate- and Function-Denpendent", in *PLoS ONE* **2012**, *7*, e45237, DOI 10.1371/journal.pone.0045237, (cit. on pp. 14, 61).

[141] M. Herbig, M. Kräter, K. Plak, P. Müller, J. Guck, O. Otto, *Flow Cytometry Protocols*, *Vol. 263*, Humana Press, **2004**, Chapter 15: Real-Time Deformability Cytometry: Label-Free Functional Characterization of Cells, pp. 347–369 (cit. on p. 14).

[142] A. Mietke, O. Otto, S. Girardo, P. Rosendahl, A. Taubenberger, S. Golfier, E. Ulbricht, S. Aland, J. Guck, E. Fischer-Friedrich, "Extracting Cell Stiffness from Real-Time Deformability Cytometry: Theory and Experiment", in *Biophysical Journal* **2015**, *109*, 2023–2036, DOI 10.1016/j.bpj.2015.09.006, (cit. on p. 14).

[143] A. Jacobi, M. Rosendahl, Philipp abd Kräter, M. Urbanska, M. Herbig, J. Guck, *Stem Cell Mobilization: Methods and Protocols*, Humana Press, **2017**, Chapter 11: Analysis of Biomechanical Properties of Hematopoietic Stem and Progenitor Cells Using Real-Time Fluorescence and Deformability Cytometry, pp. 135–148 (cit. on pp. 14, 61).

[144] N. Toepfner et al., "Detection of human disease conditions by single-cell morpho-rheological phenotyping of blood", in *bioRxiv* **2017**, 145078, DOI 10.1101/145078, (cit. on pp. 14, 61).

[145] A. C. Hodgson, C. M. Verstreken, C. L. Fisher, U. F. Keyser, S. Pagliara, K. J. Chalut, "A microfluidic device for characterizing nuclear deformations", in *Lab on a Chip* **2017**, *17*, 805–813, DOI 10.1039/c6lc01308b, (cit. on pp. 14, 61).

[146] Y. Ge, P. Rosendahl, C. Durán, N. Töpfner, S. Ciucci, J. Guck, C. V. Cannistraci, "Cell Mechanics Based Computational Classification of Red Blood Cells Via Machine Intelligence Applied to Morpho-Rheological Markers", in *IEEE/ACM Transactions on Computational Biology and Bioinformatics* **2019**, *5963*, 1–13, DOI 10.1109/tcbb.2019.2945762, (cit. on p. 14).

[147] F. Reichel, J. Mauer, A. A. Nawaz, G. Gompper, J. Guck, D. A. Fedosov, "High-Throughput Microfluidic Characterization of Erythrocyte Shapes and Mechanical Variablity", in *Biophysical Journal* **2019**, *117*, 14–24, DOI 10.1016/j.bpj.2019.05.022, (cit. on pp. 14, 61).

[148] K. R. Bashant, A. Vassallo, C. Herold, R. Berner, L. Menschner, J. Subburayalu, M. J. Kaplan, C. Summers, J. Guck, E. R. Chilvers, N. Toepfner, "Real-time deformability cytometry reveals sequential contraction and expansion during neutrophil priming", in *Journal of Leukocyte Biology* **2019**, *105*, 1143–1153, DOI 10.1002/JLB.MA0718-295RR, (cit. on pp. 14, 61).

[149] S. Pagliara, L. Persano, A. Camposeo, R. Cingolani, D. Pisignono, "Registration accuracy in multilevel soft lithography", in *Nanytechnology* **2007**, *18*, 1–6, DOI 10.1088/0957-4484/18/17/175302, (cit. on p. 20).

[150] S. Pagliara, C. Chimerel, R. Langford, D. G. A. L. Aarts, U. F. Keyser, "Parallel sub-micrometre channels with different dimensions for laser scattering detection", in *Lab on a Chip* **2011**, *11*, 3365–3368, DOI 10.1039/c1lc20399a, (cit. on p. 20).

[151] H. M. Shapiro, *Practical Flow Cytometry*, Wiley-Liss, **2003** (cit. on p. 21).

[152] FlowJo^{TM} Software for Windows, [software application], version 10, Ashland, OR: Becton, Dickinson and Company, **2019** (cit. on p. 23).

[153] P. R. Griffiths, J. A. De Haseth, *Fourier transform infrared spectrometry*, Wiley-Interscience, **2007**, p. 529 (cit. on p. 24).

[154] H. H. Mantsch, D. Chapman, *Infrared spectroscopy of biomolecules*, Wiley-Liss, **1996** (cit. on p. 24).

[155] F. Parker, *Applications of Infrared Spectroscopy in Biochemistry, Biology, and Medicine*, Springer Science & Business Media, **1971** (cit. on p. 24).

[156] M. J. Baker et al., "Using Fourier transform IR spectroscopy to analyze biological materials", in *Nature Protocols* **2014**, *9*, 1771–1791, DOI 10.1038/nprot.2014.110, (cit. on pp. 24, 26, 35).

[157] D. L. Wetzel, S. M. LeVine, "Imaging molecular chemistry wutg infrared microscopy", in *Science* **1999**, *285*, 1224–1224, DOI 10.1126/science.285.5431.1224, (cit. on p. 26).

[158] R. Bhargava, "Infrared Spectroscopic Imaging: The Next Generation", in *Applied Spectroscopy* **10/2012**, *66*, 1091–1120, DOI 10.1366/12-06801, (cit. on p. 26).

[159] C. Beleites, V. Sergo, hyperSpec: a package to handle hyperspectral data sets in R, R package version 0.99-20171005, **2017** (cit. on p. 27).

[160] B. Auguie, A. Antonov, gridExtra: Miscellaneous Functions for "Grid" Graphics (cit. on p. 27).

[161] H. Bengtsson, H. C. Bravo, R. Gentleman, O. Hossjer, H. Jaffee, D. Jiang, P. Langfelder, P. Hickey, B. Montgomery, matrixStats: Functions that Apply to Rows and Columns of Matrices (and to Vectors) (cit. on p. 27).

[162] N. Colthup, *Introduction to Infrared and Raman Spectroscopy*, Elsevier Science, **2012** (cit. on p. 28).

[163] C. Trapnell, A. Roberts, L. Goff, G. Pertea, D. Kim, D. R. Kelley, H. Pimente, S. L. Salzberg, J. L. Rinn, L. Pachter, "Differential gene and transcript expression analysis of RNA-seq experiments with TopHat and Cufflinks", in *Nature Protocols* **2013**, *7*, 562–578, DOI 10.1038/nprot.2012.016, (cit. on p. 32).

[164] T. Metsalu, J. Vilo, "ClustVis: a web tool for visualizing clustering of multivariate data using Principal Component Analysis and heatmap", in *Nucleic Acids Research* **2015**, *43*, W566–W570, DOI 10.1093/nar/gkv468, (cit. on pp. 32, 80).

[165] Z. Zhang, Y. Zhang, P. Evans, Chinwalla, D. Taylor, "RNA-seq 2G: online analysis of differential gene expression with comprehensive options of stistical methods", in *bioRxiv* **2017**, *6*, W566–W570, DOI 10.1101/122747, (cit. on p. 32).

[166] T. S. P. Heng, M. W. Painter, T. I. G. P. Consortium, "The Immunological Genome Project: networks of gene expression in immune cells", in *Nature Immunology* **2008**, *9*, 1091–1094, DOI 10.1038/ni1008-1091, (cit. on p. 32).

[167] S. van der Walt, J. L. Schönberger, J. Nunez-Iglesias, F. Boulogne, J. D. Warner, N. Yager, E. Gouillart, T. Yu, "scikit-image: image processing in Python", in *PeerJ* **2014**, *2*, e453, DOI 10.7717/peerj.453, (cit. on p. 34).

[168] T. E. Oliphant, *A guide to NumPy*, Trelgol Publishing, **2006** (cit. on p. 34).

[169] E. Jones, T. Oliphant, P. Peterson, SciPy: Open Source Scientific Tools for Python, **2001** (cit. on p. 34).

[170] G. J. Filion, J. G. van Bemmel, U. Braunschweig, W. Talhout, J. Kind, L. D. Ward, W. Brugman, I. J. de Castro, R. M. Kerkhoven, H. J. Bussemaker, B. van Steensel, "Systematic Protein Location Mapping Reveals Five Principal Chromatin Types in *Drosophila* Cells", in *Cell* **2010**, *143*, 212–224, DOI 10.1016/j.cell.2010.09.009, (cit. on p. 35).

[171] W. Deng, X. Shi, R. Tjian, T. Lionnet, R. H. Singer, "CASFISH: CRISPR/Cas9-mediated in situ labeling of genomic loci in fixed cells", in *Proceedings of the National Academy of Sciences of the United States of America* **2015**, *112*, 11870–11875, DOI 10.1073/pnas.1515692112, (cit. on p. 35).

[172] S. Wang, J.-H. Su, B. J. Beliveau, B. Bintu, J. R. Moffitt, C.-t. Wu, X. Zhuang, "Spatial organixation of chromatin domains and compartments in single chromosomes", in *Science* **2016**, *353*, 598–602, DOI 10.1126/science.aaf8084, (cit. on p. 35).

[173] S. Wang, J.-H. Su, F. Zhang, X. Zhuang, "An RNA-aptamer-based two-color CRISPR labeling system", in *Scientific Reports* **2016**, *6*, 26857, DOI 10.1038/srep26857, (cit. on p. 35).

[174] T. Nagano, Y. Lubling, T. J. Stevens, S. Schoenfelder, E. Yaffe, W. Dean, E. D. Laue, A. Tanay, P. Fraser, "Single-cell Hi-C reveals cell-to-cell variability in chromosome structure", in *Nature* **2013**, *502*, 59–64, DOI 10.1038/nature12593, (cit. on p. 35).

[175] D. R. Whelan, K. R. Bambery, P. Heraud, M. J. Tobin, M. Diem, D. McNaughton, B. R. Wood, "Monitoring the reversible B to A-like transition of DNA in eukaryotic cells using Fourier transform infrared spectroscopy", in *Nucleic Acids Research* **2011**, *39*, 5439–5448, DOI 10.1093/nar/gkr175, (cit. on p. 35).

[176] B. R. Wood, "The importance of hydration and DNA conformation in interpreting infrared spectra of cells and tissues", in *Chem. Soc. Rev.* **2016**, *45*, 1980–1998, DOI 10.1039/C5CS00511F, (cit. on pp. 35, 45, 47, 105, 106).

[177] J. Nallala, G. R. Lloyd, M. Hermes, N. Shepherd, N. Stone, "Enhanced spectral histology in the colon using high-magnification benchtop FTIR imaging", in *Vibrational Spectroscopy* **2016**, *91*, 83–91, DOI 10.1016/j.vibspec.2016.08.013, (cit. on p. 37).

[178] D. Perez-Guaita, D. Andrew, P. Heraud, J. Beeson, D. Anderson, J. Richards, B. R. Wood, "High resolution FTIR imaging provides automated discrimination and detection of single malaria parasite infected erythrocytes on glass", in *Faraday Discussions* **2016**, *187*, 341–352, DOI 10.1039/c5fd00181a, (cit. on p. 37).

[179] H. Shinzawa, B. Turner, J. Mizukado, S. Kazarian, "Protein hydration in living cells probed by Fourier transform infrared (FT-IR) spectroscopic imaging", in *Analyst* **06/2017**, *142*, 2475–2483, DOI 10.1039/c7an00337d, (cit. on p. 37).

[180] H. A. Crissman, J. A. Steinkamp, "Rapid, simultaneous measurement of DNA, protein, and cell volume in single cells from large mammalian cell populations", in *Journal of Cell Biology* **1973**, *59*, 766–771, DOI 10.1083/jcb.59.3.766, (cit. on p. 41).

[181] T. Fowler, A. S. Garruss, A. Ghosh, S. De, K. G. Becker, W. H. Wood, M. T. Weirauch, S. T. Smale, B. Aronow, R. Sen, A. L. Roy, "Divergence of transcriptional landscape occurs early in B cell activation", in *Epigenetics and Chromatin* **2015**, *8*, e1–14, DOI 10.1186/s13072-015-0012-x, (cit. on p. 43).

[182] Y. Zhang, D. J. Fear, S. A. G. Willis-Owen, W. O. Cookson, M. F. Moffatt, "Global gene regulation during activation of immunoglobulin class switching in human B cells", in *Scientific Reports* **2016**, *6*, 37988, DOI 10.1038/srep37988, (cit. on p. 43).

[183] F. Kouzine et al., "Global regulation of promoter melting in naive lymphocytes", in *Cell* **2013**, *153*, 988, DOI 10.1016/j.cell.2013.04.033, (cit. on p. 43).

[184] J. S. Rawlings, M. Gatzka, P. G. Thomas, J. N. Ihle, "Chromatin condensation via the condensin II complex is required for peripheral T-cell quiescence", in *EMBO journal* **2011**, *30*, 263–276, DOI 10.1038/emboj.2010.314, (cit. on p. 43).

[185] J. Kong, S. Yu, "Fourier transform infrared spectroscopic analysis of protein secondary structures", in *Acta Biochimica et Biophysica Sinica* **2007**, *39*, 549–559, DOI 10.1111/j.1745-7270.2007.00320.x, (cit. on pp. 45, 47, 105, 106).

[186] R. Sandberg, I. Ernberg, "The molecular portrait of in vitro growth by meta-analysis of gene-expression profiles", in *Genome biology* **2005**, *6*, R65, DOI 10.1186/gb-2005-6-8-r65, (cit. on p. 47).

[187] K. M. Olsavsky, J. L. Page, M. C. Johnson, H. Zarbl, S. C. Strom, C. J. Omiecinski, "Gene expression profiling and differentiation assessment in primary human hepatocyte cultures, established hepatoma cell lines, and human liver tissues", in *Toxicology and Applied Pharmacology* **2007**, *222*, 42–56, DOI 10.1016/j.taap.2007.03.032, (cit. on p. 47).

[188] C. Pan, C. Kumar, S. Bohl, U. Klingmueller, M. Mann, "Comparative proteomic phenotyping of cell lines and primary cells to assess preservation of cell type-specific functions", in *Molecular and Cellular Proteomics* **2009**, *8*, 443–450, DOI 10.1074/mcp.M800258-MCP200, (cit. on p. 47).

[189] C. S. Alge, S. M. Hauck, S. G. Priglinger, A. Kampik, M. Ueffinf, "Differential protein profiling of primary versus immortalized human RPE cells identifies expression patterns associated with cytoskeletal remodeling and cell survival", in *Journal of Proteome Research* **2006**, *5*, 862–878, DOI 10.1021/pr050420t, (cit. on p. 47).

[190] T. J. Kirby, J. Lammerding, "Emerging views of the nucleus as a cellular mechanosensor", in *Nature Cell Biology* **2018**, *20*, 373–381, DOI 10.1038/s41556-018-0038-y, (cit. on pp. 52, 93).

[191] T. Iskratsch, H. Wolfenson, M. P. Sheetz, "Appreciating force and shape - the rise of mechanotransduction in cell biology", in *Nature Reviews Molecular Cell Biology* **2014**, *15*, 825–833, DOI 10.1038/nrm3903, (cit. on p. 52).

[192] N. Otsu, "A Threshold Selection Method from Gray-Level Histograms", in *IEEE Transactions on Systems Man and Cybernetics* **1979**, *9*, 62–66, DOI 10.1109/TSMC.1979.4310076, (cit. on p. 54).

[193] C. H. Li, C. K. Lee, "Minimum Cross Entropy Thresholding", in *Patterns Recognition* **1993**, *26*, 617–625, DOI 10.1016/0031-3203(93)90115-D, (cit. on p. 54).

[194] J.-C. Yen, F.-J. Chang, S. Chang, "A New Criterion for Automatic Multilevel Thresholding", in *IEEE Transactions on Image Processing* **1995**, *4*, 370–378, DOI 10.1109/83.366472, (cit. on p. 54).

[195] J. Schindelin et al., "Fiji: an open-source platform for biological-image analysis", in *Nature Methods* **2012**, *9*, 676–682, DOI 10.1038/nmeth.2019, (cit. on p. 54).

[196] M. V. Barich, A. T. Krummel, "Polymeric Infrared Compatible Microfluidic Devices for Spectrochemical Analysis", in *Analytical Chemistry* **2013**, *85*, 10000–10003, DOI 10.1021/ac4026016, (cit. on p. 62).

[197] E. Vigorito et al., "microRNA-155 Regulates the Generation of Immunoglobulin Class-Switched Plasma Cells", in *Immunity* **2007**, *27*, 847–859, DOI 10.1016/j.immuni.2007.10.009, (cit. on p. 72).

[198] L. Wang, N. Whang, R. Wuerffel, A. L. Kenter, "AID-dependent histone acetylation is detected in immunoglobulin S regions", in *The Journal of experimental medicine* **2006**, *203*, 215–226, DOI 10.1084/jem.20051774, (cit. on p. 72).

[199] S. Ramachandran, D. Haddad, C. Li, M. X. Le, A. K. Ling, C. C. So, R. M. Nepal, J. L. Gommerman, K. Yu, T. Ketela, J. Moffat, A. Martin, "The SAGA Deubiquitination Module Promotes DNA Repair and Class Switch Recombination through ATM and DNAPK-Mediated γH2AX Formation", in *Cell Reports* **2016**, *15*, 1554–1565, DOI 10.1016/j.celrep.2016.04.041, (cit. on p. 72).

[200] Z. Xu et al., "14-3-3 adator proteins recruit AID to 5'-AGCT-3'-rich switch regions for class switch recombination", in *Nature structural molecular biology* **2010**, *17*, 1124–1135, DOI 10.1038/nsmb.1884, (cit. on p. 72).

[201] J. P. Ridoux, J. Liquier, E. Taillandier, "Raman spectroscopy of Z-Form Poly[d(A-T)]•Poly[d(A-T)]", in *Biochemistry* **1988**, *27*, 3874–3878, DOI 10.1021/bi00410a052, (cit. on pp. 76, 90, 97, 109).

[202] C. Kendall, J. Day, J. Hutchings, B. Smith, N. Shepherd, H. Barr, N. Stone, "Evaluation of Raman probe for oesophageal cancer diagnostics", in *Analyst* **2010**, *135*, 3038–3041, DOI 10.1039/c0an00536c, (cit. on pp. 76, 109).

[203] N. Stone, C. Kendall, J. Smith, P. Crow, H. Barr, "Raman spectroscopy for identification of epithelial cancers", in *Faraday Discussions* **2004**, *126*, 141–157, DOI 10.1039/c0an00536c, (cit. on pp. 76, 108–125).

[204] Z. Liu, C. Davis, W. Cai, L. He, X. Chen, H. Dai, "Circulation and long-term fate of functionalized, biocompatible single-walled carbon nanotubes in mice probed by Raman spectroscopy", in *Proceedings of the National Academy of Sciences of the United States of America* **2008**, *105*, 1410–1415, DOI 10.1073/pnas.0707654105, (cit. on pp. 76, 109–111, 113–123, 125).

[205] A. J. Ruiz-Chica, M. A. Medina, F. Sánchez-Jiménez, F. J. Ramirez, "Characterization by Raman spectroscopy of conformational changes on guanine-cytosine and adenine-thymine oligonucleotides induced by aminooxy analogues of spermidine", in *Journal of Raman Spectroscopy* **2004**, *35*, 93–100, DOI 10.1002/jrs.1107, (cit. on pp. 76, 109, 110, 112, 118–125).

[206] Z. W. Huang, A. McWilliams, H. Lui, D. I. McLean, S. Lam, H. S. Zeng, "Near-infrared Raman spectroscopy for optical diagnosis of lung cancer", in *Int. J. Canc.* **2003**, *107*, 1047–1052, DOI 10.1002/ijc.11500, (cit. on pp. 76, 108, 110, 111, 114, 120–122, 124, 125).

[207] N. Stone, C. Kendall, N. Shepherd, P. Crow, H. Barr, "Near-infrared Raman spectroscopy for the classification of epithelial pre-cancers and cancers", in *Journal of Raman Spectroscopy* **2002**, *33*, 564–573, DOI 10.1002/jrs.882, (cit. on pp. 76, 108, 112, 114, 116–119, 121–125).

[208] W.-T. Cheng, M.-T. Liu, H.-H. Liu, S.-Y. Lin, "Micro-Raman Spectroscopy Used to Identify and Grade Human Skin Pilomatrixoma", in *Microscopy Research and Technique* **2005**, *68*, 75–79, DOI 10.1002/jemt.20229, (cit. on pp. 76, 108, 111, 113–125).

[209] G. Shetty, C. Kendall, N. Shepherd, N. Stone, H. Barr, "Raman spectroscopy: elucidation of biochemical changes in carcinogenesis of oesophagus", in *British Journal of Cancer* **2006**, *94*, 1460–1464, DOI 10.1038/sj.bjc.6603102, (cit. on pp. 76, 109, 111–114, 119, 121, 123, 124).

[210] M. Gniadecka, H. C. Wulf, N. Nymark Mortensen, O. Faurskov Nielsen, D. H. Christensen, "Diagnosis of Basal Cell Carcinoma by Raman Spectroscopy", in *Journal of Raman Spectroscopy* **1997**, *28*, 125–129, DOI 10.1002/(sici)1097-4555(199702)28:2/3<125::aid-jrs65>3.0.co;2-#, (cit. on pp. 76, 110).

[211] C. Krafft, L. Neudert, T. Simat, R. Salzer, "Near infrared Raman spectra of human brain lipids", in *Spectrochimica Acta - Part A: Molecular and Biomolecular Spectroscopy* **2005**, *61*, 1529–1535, DOI 10.1016/j.saa.2004.11.017, (cit. on pp. 76, 108–112, 115, 117, 121–123, 126).

[212] L. E. Kamemoto, A. K. Misra, S. K. Sharma, M. T. Goodman, H. Luk, A. C. Dykes, T. Acosta, "Near-Infrared Micro-Raman Spectroscopy for *in Vitro* Detection of Cervical Cancer", in *Applied Spectroscopy* **2010**, *64*, 255–261, DOI 10.1366/000370210790918364, (cit. on pp. 76, 121).

[213] C. Ribeiro de Almeida, S. Dhir, A. Dhir, A. E. Moghaddam, Q. Sattentau, A. Meinhart, N. J. Proudfoot, "RNA Helicase DDX1 Converts RNA G-Quadruplex Structures into R-Loops to Promote *IgH* Class Switch Recombination", in *Molecular Cell* **2018**, *70*, 650–662.e8, DOI 10.1016/j.molcel.2018.04.001, (cit. on p. 79).

[214] D. Warde-Farley et al., "The GeneMANIA prediction server: biological network integration for gene prioritization and predicting gene function", in *Nucleic Acids Research* **2010**, *38*, 214–220, DOI 10.1093/nar/gkq537, (cit. on p. 80).

[215] A. Orthwein, A.-M. Patenaude, E. B. Affar, A. Lamarre, J. C. Young, J. M. Di Noia, "Regulation of activation-induced deaminase stability and antibody gene diversification", in *Journal of Experimental Medicine* **2010**, *207*, 2751–2765, DOI 10.1084/jem.20101321, (cit. on p. 86).

[216] J. Li, W. Yin, Y. Jing, D. Kang, L. Yang, J. Cheng, Z. Yu, Z. Peng, X. Li, Y. Wen, X. Sun, B. Ren, C. Liu, "The Coordination Between B Cell Receptor Signaling and the Actin Cytoskeleton During B Cell Activation", in *Frontiers in Immunology* **2019**, *10*, 1–13, DOI 10.3389/fimmu.2018.03096, (cit. on p. 87).

[217] W. Song, C. Liu, A. Upadhyaya, "The pivotal position of the actin cytoskeleton in the initiation and regulation of B cell receptor activation", in *Biochimica et Biophysica Acta - Biomembranes* **2014**, *1838*, 569–578, DOI 10.1016/j.bbamem.2013.07.016, (cit. on p. 87).

[218] C. Baarlink, M. Plessner, A. Sherrard, K. Morita, S. Misu, D. Virant, E.-M. Kleinschnitz, R. Harniman, D. Alibhai, S. Baumeister, K. Miyamoto, U. Endesfelder, A. Kaidi, R. Grosse, "A transient pool of nuclear F-actin at mitotic exit controls chromatin organization", in *Nature Cell Biology* **2017**, *19*, 1389–1399, DOI 10.1038/ncb3641, (cit. on p. 87).

[219] V. Hurst, K. Shimada, S. M. Gasser, "Nuclear Actin and Actin-Binding Proteins in DNA Repair", in *Trends in Cell Biology* **2019**, *29*, 462–476, DOI 10.1016/j.tcb.2019.02.010, (cit. on p. 87).

[220] C. P. Caridi, M. Plessner, R. Grosse, I. Chiolo, "Nuclear actin filaments in DNA repair dynamics", in *Nature Cell Biology* **2019**, *21*, 1068–1077, DOI 10.1038/s41556-019-0379-1, (cit. on p. 87).

[221] J. M. Benevides, G. J. Thomas JR, "Characterization of DNA structures by Raman spectroscopy: high-salt and low-salt forms of double helical poly(dG-dC) in H_2O and D_2O solutions and application to B, Z and A-DNA", in *Nucleic Acids Research* **1983**, *11*, 5747–5761, DOI 10.1093/nar/11.16.5747, (cit. on pp. 90, 109).

[222] B. Wittig, T. Dorbic, A. Rich, "Transcription is associated with Z-DNA formation in metabolically active permeabilized mammalian cell nuclei", in *Proceedings of the National Academy of Sciences of the United States of America* **1991**, *88*, 2259–2263, DOI 10.1073/pnas.88.6.2259, (cit. on pp. 90, 97).

[223] S.-I. Shin, S. Ham, J. Park, H. Seo, Seong, C. H. Lim, H. Jeon, J. Huh, T.-Y. Roh, "Z-DNA-forming sites identified by ChIP-Seq are associated with actively transcribed regions in the human genome", in *DNA Research* **2016**, *23*, 477–486, DOI 10.1093/dnares/dsw031, (cit. on pp. 90, 97).

[224] M. Crisp, B. Burke, "The nuclear envelope as an integrator of nuclear and cytoplasmic architecture", in *FEBS Letters* **2008**, *582*, 2023–2032, DOI 10.1016/j.febslet.2008.05.001, (cit. on p. 93).

[225] S. G. Alam, D. Lovett, D. I. Kim, K. J. Roux, R. B. Dickinson, T. P. Lele, "The nucleus is an intracellular propagator of tensile forces in NIH 3T3 fibroblasts", in *Journal of Cell Science* **2015**, *128*, 1901–1911, DOI 10.1242/jcs.161703, (cit. on p. 93).

[226] S. G. Alam, Q. Zhang, N. Prasad, Y. Li, S. Chamala, R. Kuchibhotla, B. KC, V. Aggarwal, S. Shrestha, A. L. Jones, S. E. Levy, K. J. Roux, J. A. Nickerson, T. P. Lele, "The mammalian LINC complex regulates genome transcriptional responses to substrate rigidity", in *Scientific Reports* **2016**, *6*, 38063, DOI 10.1038/srep38063, (cit. on p. 93).

[227] G. Uzer, G. Bas, B. Sen, Z. Xie, S. Birks, M. Olcum, C. McGrath, M. Styner, J. Rubin, "Sun-mediated mechanical LINC between nucleus and cytoskeleton regulates βcatenin nucleus access", in *Journal of Biomechanics* **2018**, *74*, 32–40, DOI 10.1016/j.jbiomech.2018.04.013, (cit. on p. 93).

[228] S. R. Solmaz, G. Blobel, I. Melcák, "Ring cycle for dilating and constricting the nuclear pore", in *Proceedings of the National Academy of Sciences of the United States of America* **2013**, *110*, 5858–5863, DOI 10.1073/pnas.1302655110, (cit. on p. 93).

[229] H. Chug, S. Trakhanov, B. B. Hülsmann, T. Pleiner, D. Görlich, "Crystal strcuture of the metazoan Nup62•Nup58•Nup54 nucleoporin complex", in *Science* **2015**, *350*, 106–110, DOI 10.1126/science.aac7420, (cit. on p. 93).

[230] T. Stuwe et al., "Architecture of the fungal nuclear pore inner ring complex", in *Science* **2015**, *350*, 56–64, DOI 10.1126/science.aac9176, (cit. on p. 93).

[231] C. Stewart, B. Burke, "Teratocarcinoma Stem Cells and Early Mouse Embryos Contain Only a Single Major Lamin Polypeptide Closely Resembling Lamin B", in *Cell* **1987**, *51*, 383–392, DOI 10.1016/0092-8674(87)90634-9, (cit. on p. 94).

[232] R.-A. Röber, K. Weber, M. Osborn, "Differential timing of nuclear lamin A/C expression in the various organs of the mouse embryo and the young animal: a developmental study", in *Development* **1989**, *105*, 365–378, (cit. on p. 94).

[233] S. A. Adam, R. D. Goldman, "Insights into the Differences between the A- and B-Type Nuclear Lamins", in *Advances in Biological Regulation* **2012**, *52*, 108–113, DOI 10.1016/j.advenzreg.2011.11.001, (cit. on p. 94).

[234] M. Huse, "Mechanical forces in the immune system", in *Nature Reviews Immunology* **2017**, *17*, 679–690, DOI 10.1038/nri.2017.74, (cit. on p. 94).

[235] M. Tomura, A. Sakaue-Sawano, Y. Mori, M. Takase-Utsugi, A. Hata, K. Ohtawa, O. Kanagawa, A. Miyawaki, "Contrasting Quiescent G_0 Phase with Mitotic Cell Cycling in the Mouse Immune System", in *PLoS ONE* **2013**, *8*, e73801, DOI 10.1371/journal.pone.0073801, (cit. on p. 94).

[236] A. N. Blackford, S. P. Jackson, "ATM, ATR, and DNA-PK: The Trinity at the Heart of the DNA Damage Response", in *Molecular Cell* **2017**, *66*, 801–817, DOI 10.1016/j.molcel.2017.05.015, (cit. on p. 94).

[237] J. S. Brown, B. O'Carrigan, S. P. Jackson, T. A. Yap, "Targeting DNA Repair in Cancer: Beyond PARP Inhibitors", in *Cancer Discovery* **2017**, *7*, 20–37, DOI 10.1158/2159-8290.CD-16-0860, (cit. on p. 94).

[238] J. M. González-Granado, C. Silvestre-Roig, V. Rocha-Perugini, L. Trigueros-Motos, D. Cibrián, G. Morlino, M. Blanco-Berrocal, F. G. Osorio, J. M. P. Freije, C. López-Otin, F. Sánchez-Madrid, V. Andrés, "Nuclear Envelope Lamin-A Couples Actin Dynamics with Immunological Synapse Architecture and T Cell Activation", in *Science Signaling* **2014**, *7*, ra37, DOI 10.1126/scisignal.2004872, (cit. on p. 95).

[239] A. Purwada, M. K. Jaiswal, H. Ahn, T. Nojima, D. Kitamura, A. K. Gaharwar, L. Cerchietti, A. Singh, "*Ex vivo* engineered immune organoids for controlled germinal center reactions", in *Biomaterials* **2015**, *63*, 24–34, DOI 10.1016/j.biomaterials.2015.06.002, (cit. on p. 95).

[240] P. B. Gupta, C. M. Fillmore, G. Jiang, S. D. Shapira, K. Tao, C. Kuperwasser, E. S. Lander, "Stochastic State Transitions Give Rise to Phenotypic Equilibrium in Population of Cancer Cells", in *Cell* **2011**, *146*, 633–644, DOI 10.1016/j.cell.2011.07.026, (cit. on p. 96).

[241] A. Kreso, J. E. Dick, "Evolution of the Cancer Stem Cell Model", in *Cell Stem Cell* **2014**, *14*, 275–291, DOI 10.1016/j.stem.2014.02.006, (cit. on p. 96).

[242] H. Oldenhof, S. Schütze, W. F. Wolkers, H. Sieme, "Fourier transform infrared spectroscopic analysis of sperm chromatin structure and DNA stability", in *Andrology* **2016**, *4*, 430–441, DOI 10.1111/andr.12166, (cit. on p. 96).

[243] D. Evenson, Z. Darzynkiewicz, M. Melamed, "Relation of Mammalian Sperm Chromatin Heterogeneity to Fertility", in *Science* **1980**, *210*, 1–3, DOI 10.1126/science.7444440, (cit. on p. 96).

[244] J. Erenpreiss, M. Spano, J. Erenpreisa, M. Bungum, A. Giwercman, "Sperm chromatin structure and male fetility: biological and clinical aspects", in *Asian Journal of Andrology* **2006**, *8*, 11–29, DOI 10.1111/j.1745-7262.2006.00112.x, (cit. on p. 96).

[245] R. Prevedel, A. Diz-Muñoz, G. Ruocco, G. Antonacci, "Brillouin microscopy: an emerging tool for mechanobiology", in *Nature Methods* **2019**, *16*, 969–977, DOI 10.1038/s41592-019-0543-3, (cit. on p. 101).

[246] F. Palombo, D. Fioretto, "Brillouin Light Scattering: Applications in Biomedical Sciences", in *Chemical Reviews* **2019**, *119*, 7833–7847, DOI 10.1021/acs.chemrev.9b00019, (cit. on p. 101).

[247] A. J. Traverso, J. V. Thompson, Z. A. Steelman, Z. Meng, M. O. Scully, V. V. Yakovlev, "Dual Raman-Brillouin Microscope for Chemical and Mechanical Characterization and Imaging", in *Analytical Chemistry* **2015**, *87*, 7519–7523, DOI 10.1021/acs.analchem.5b02104, (cit. on p. 101).

[248] F. Scarponi et al., "High-Performance Versatile Setup for Simultaneous Brillouin-Raman Microspectroscopy", in *Physical Review X* **2017**, *7*, 1–11, DOI 10.1103/PhysRevX.7.031015, (cit. on p. 101).

[249] A. C. S. Talari, Z. Movasaghi, S. Rehman, I. U. Rehman, "Raman Spectroscopy of Biological Tissues", in *Applied Spectroscopy Reviews* **2015**, *50*, 46–111, DOI 10.1080/05704920701551530, (cit. on pp. 107–126).

[250] J. L. Deng, Q. Wei, M. H. Zhang, Y. Z. Wang, Y. Q. Li, "Study of the effect of alcohol on single human red blood cells using near-infrared laser tweezers Raman spectroscopy", in *Journal of Raman Spectroscopy* **2005**, *36*, 257–261, DOI 10.1002/jrs.1301, (cit. on p. 108).

[251] C. M. Muntean, G. J. Puppels, J. Greve, G. M. J. Segers-Nolten, S. Cinta-Pinzaru, "Raman microspectroscopic study on low-pH-induced DNA structural transitions in the presence of magnesium ions", in *Journal of Raman Spectroscopy* **2002**, *33*, 784–788, DOI 10.1002/jrs.918, (cit. on p. 108).

[252] J. Ruiz-Chica, M. A. Medina, F. Sanchez-Jimenez, F. J. Ramirez, "Fourier Transform Raman study of the structural specificities on the interaction between DNA and biogenic polyamines", in *Biophysical Journal* **2001**, *80*, 443–454, DOI 10.1016/S0006-3495(01)76027-4, (cit. on p. 108).

[253] J. W. Chan, D. S. Taylor, T. Zwerdling, S. M. Lane, K. Ihara, T. Huser, "Micro-Raman spectroscopy detects individual neoplastic and normal hematopoietic cells", in *Biophysical Journal* **2006**, *90*, 648–656, DOI 10.1529/biophysj.105.066761, (cit. on p. 109).

[254] T. Bhattacharjee, P. Kumar, G. Maru, A. Ingle, C. M. Krishna, "Swiss bare mice: A telomeric model for transcutaneous in vivo Raman spectroscopic studies of breast cancer", in *Laser. Med. Sci.* **2014**, *29*, 325–333, DOI 10.1007/s10103-013-1347-9, (cit. on p. 114).

[255] F. Bonnier, H. J. Byrne, "Understanding the molecular information contained in principal component analysis of vibrational spectra of biological systems", in *Analyst* **2012**, *137*, 2, DOI 10.1039/c1an15821j, (cit. on p. 114).

[256] R. J. Lakshmi, V. B. Kartha, C. M. Krishna, J. G. R. Solomon, G. Ullas, P. U. Devi, "Tissue Raman spectroscopy for the study of radiation damage: Brain irradiation of mice", in *Radiation Research* **2002**, *157*, 175–182, DOI 10.1667/0033-7587(2002)157[0175:TRSFTS]2.0.CO;2, (cit. on p. 114).

[257] A. J. Hobro, D. M. Standley, S. Ahmad, N. I. Smith, "Deconstructing RNA: optical measurement of composition and structure", in *Physical Chemistry Chemical Physics* **2013**, *15*, 13199–13208, DOI 10.1039/c3cp52406j, (cit. on p. 125).

[258] Y.-L. Tang, Z.-Y. Guo, "Raman spectroscopic analysis of the effect of ultraviolet irradiation on calf thymus DNA", in *Acta Biochimia et Biophysica Sinica* **2005**, *37*, 39–46, DOI 10.1093/abbs/37.1.39, (cit. on p. 125).